Sellmeijer in the northern Maasvallei

Assessing the applicability of the Sellmeijer design rule for hydrogeological systems in Limburg

MSc Thesis
Sanne van Dijk

TUDelft

ARCADIS

Sellmeijer in the northern Maasvallei

Assessing the applicability of the Sellmeijer design rule for hydrogeological systems in Limburg

by

Sanne van Dijk

to obtain the degree of Master of Science
at the Delft University of Technology,
to be defended publicly on Thursday February 9 2023, at 15:00.

Cover Image: drone photo of the flood event in the Ooijen-Wanssum Maaspark in Limburg (Projectbureau Ooijen-Wanssum, 2021)

ŤUDelft   **ARCADIS**

Preface

This report is a compilation of the research that I have performed during my master's thesis for completion of the Master (track) Hydraulic Engineering at the Faculty of Civil Engineering and Geosciences of Delft University of Technology. The objective of my thesis was to assess the applicability of the Sellmeijer design rule for hydrogeological conditions in Limburg.

I had the opportunity to perform my research during a graduation internship at Arcadis. Obviously, I learned a lot about piping and numerical modelling during my thesis and internship, but I also learned things that I did not expect to learn. For example, I discovered that keeping track of the big picture in such a long project is difficult for me. I tend to get caught up in one small topic and lose myself in its details. Also, I have found that taking the train from Delft to Arnhem is not that bad when you get a nice day at the office in return.

To conclude, I want to express my gratitude to a few people who have helped me throughout my study and thesis. To begin, I would like to thank my Arcadis supervisor, Rimmer Koopmans, for introducing me to the world of piping, for your critical remarks based on your expertise, and for your unwavering support. Furthermore, I would like to thank my supervisor at TU Delft, Juan Pablo Aguilar-López, for the motivational meetings every Friday and your patience with my slow Excel and numerical modelling skills. At first, I was hesitant about numerical modelling, but I enjoyed becoming a COMSOL ninja. I also would like to thank Harm Aantjes for sparking my interest in civil engineering, particularly flood defences, and for always being interested in my progress and work. Finally, thank you to Koen, family, and friends for all your help, for keeping me from spiraling (on occasion), and for your encouragement throughout my entire time as a student.

Sanne van Dijk
Delft, February 2023

Abstract

The applicability of the Sellmeijer design rule to Limburg dike sections near Well, Hout-Blerick, Buggenum, and Thorn was investigated in this thesis. This was accomplished by building a finite element numerical model, in COMSOL Multiphysics, to assess the piping in the hydrogeological systems of the research locations. The proposed model is composed by combining several groundwater and piping model principles, schematizing dike cross-sections, and calibrating the model. The schematization choices that define the model geometry of the average pipe cross-section are critical. It was decided to apply a fracture flow pipe cross-section and the piping assessment was performed iteratively for multiple pipe height values, because the true pipe height is unknown. The pipe height is expressed as a function of the number of grains and the representative grain size.

According to a deterministic assessment, which was performed analytically using multiple versions of the Sellmeijer design rule and numerically using the proposed FEM model, piping does not occur at the research locations Well, Hout-Blerick and Thorn. Piping is theoretically possible at Buggenum, but only with a very small pipe height, making it appear very unlikely. The assessment also revealed that the critical head determined by using revised Sellmeijer design rule (2021) is conservative for the examined dike sections in Limburg. Furthermore, it is discovered that the original Sellmeijer design rule with the new geometry factor (1988/2011) produces critical heads that are similar to the results of the revised Sellmeijer design rule (2021) multiplied by 1.8, which is the current design rule used to assess piping in Limburg.

The Sellmeijer design rule (1988/2011) was stochastically evaluated to determine how the design rule changed when calibrated to Limburg parameter values. 1000 unique randomly generated dike cross-sections were evaluated on piping using the proposed FEM numerical models. The unique dike cross-sections are made up of a random combination of model parameters that were sampled from a uniform distribution using Latin Hypercube Sampling. (Olsson et al., 2003). The randomly generated dike cross-sections that demonstrate piping for a realistic pipe height, were used to re-calibrate the Sellmeijer scale factor. Using a linear regression, it was demonstrated that the scale factor corresponding to the broadened application range (including Limburg parameter values), of the Sellmeijer design rule, is 1.56 times greater than the original scale factor. This means that the original Sellmeijer design rule with the new geometry factor (1988/2011) and the additional factor of 1.56, can be applied to (Limburg) dike sections, for which the model parameters fall within the newly set parameter application ranges (e.g. $100\ \mu\text{m} \leq d_{70} \leq 900\ \mu\text{m}$).

$$\frac{H_{\text{c,o}}}{L} = 1.56 F_{\text{S,o}} F_{\text{G}} F_{\text{R}}$$

Contents

Nomenclature

Roman

a	Pipe height	[m]
a_{mesh}	Estimated maximum pipe height	[m]
B	Exponent of the Sellmeijer geometric factor	[-]
b	Width of the vertical pipe	[m]
C_{creep}	Bligh creep factor	[-]
c_0	Den Rooij packing coefficient	[-]
D_i	Thickness of layer made of soil material i	[m]
dh/dx	Hydraulic head gradient	[m/m]
d_{10}	10$^{\text{th}}$ Percentile representative size of grain	[m]
d_{50}	50$^{\text{th}}$ Percentile representative size of grain	[m]
d_{65}	65$^{\text{th}}$ Percentile representative size of grain	[m]
d_{70}	70$^{\text{th}}$ Percentile representative size of grain	[m]
d_{70m}	70$^{\text{th}}$ Percentile calibration reference value	[m]
d_{70max}	Estimated maximum d_{70}	[m]
d_{75}	75$^{\text{th}}$ Percentile representative size of grain	[m]
d_{80}	80$^{\text{th}}$ Percentile representative size of grain	[m]
D_h	Hydraulic diameter	[m]
F_{G}	Sellmeijer geometric factor	[-]
F_{R}	Sellmeijer resistance factor	[-]
$F_{\text{S,o}}$	Scale factor of the original Sellmeijer design rule (1988)	[-]
$F_{\text{S,rev}}$	Scale factor of the revised Sellmeijer design rule (2021)	[-]
$F_{S,eq}$	Sellmeijer scale factor corresponding to equilibrium condition	[-]
$F_{S,stoc}$	Stochastically determined Sellmeijer scale factor	[-]
g	Gravitational acceleration (9.81)	[m/s^2]
H	Hydraulic head	[m]
H_f	Foreland hydraulic head	[m]
H_h	Hinterland hydraulic head	[m]
$H_{c,o}$	Critical hydraulic head of original Sellmeijer design rule	[m]
$H_{c,rev}$	Critical hydraulic head of revised Sellmeijer design rule (2021)	[m]
h_p	Phreatic level at the hinterland (uplift)	[m]
i	Heave gradient	[-]
KAS	Angularity of sand particles	[-]
KAS_m	Angularity of sand particles calibrated reference value	[-]
K_a	Weighted average aquifer hydraulic conductivity	[m/s]
L	Seepage length (dike width)	[m]
l	Pipe length	[m]
n_g	Number of grains	[-]
p	Pressure	[kg/ms^2]
RD	Relative density	[-]
RD_m	Relative density calibrated reference value	[-]
R_e	Reynolds number	[-]
U	Average flow velocity across a cross-section	[m/s]
U	Uniformity of sand particles	[-]
U_c	Bottom of the cover layer	[m+NAP]
U_m	Uniformity of sand particles calibrated reference value	[-]
u	Horizontal flow velocity	[m/s]
V_{tot}	Total soil volume	[m^3]

V_v	Volume of voids/pores	[m³]
Z_h	Reliability term of heave equation	[-]
Z_u	Reliability term of uplift equation	[m]

Greek

β_{fi}	Friction coefficient of the pipe cross-section	[-]
γ_s	Soil volumetric weight (quartz)	[kN/m³]
γ_{sat}	Saturated volumetric weight cover layer	[kN/m³]
γ_{sp}	Volumetric weight of submerged sand particles	[kN/m³]
γ_w	Water volumetric weight	[kN/m³]
ϵ_i	Porosity of soil material i	[-]
η	White's sand embedment factor (0.25)	[-]
θ	Bedding angle of sand grains of Sellmeijer design rule (37)	[deg]
κ^*	Fictitious permeability	[m²]
κ_a	Weighted average aquifer intrinsic permeability	[m²]
κ_f	Fracture flow fictitious permeability	[m²]
κ_h	Horizontal intrinsic permeability	[m²]
κ_i	Intrinsic permeability of subsoil material i	[m²]
κ_v	Vertical intrinsic permeability	[m²]
λ	Leakage length	[m]
μ	Dynamic viscosity of water	[kg/ms]
ν	Kinematic viscosity of water at 10 deg	[m²/s]
ρ	Density of water	[kg/m³]
ϕ_i	Potential at location i (uplift)	[m]
$\phi_{c,u}$	Critical potential (uplift)	[m]

List of Figures

List of Tables

<div align="right">

1

</div>

Introduction

1.1. Definition

Internal erosion, backward erosion piping, and piping are terms that are frequently used interchangeably, which can cause confusion. Internal erosion is the broadest term for a variety of failure mechanisms that result in the formation of voids within the soil as a result of material removal by seepage (e.g. backward erosion and suffusion). In this report, piping refers to the failure mechanism in which groundwater erodes granular material underneath the dike and forms shallow pipes underneath the dike. Backward erosion indicates that the pipes are growing in the opposite direction of the seepage flow.

1.2. Motivation and relevancy

The Netherlands experienced an extreme flood event in July 2021, when the Maas overflowed its river banks and flooded adjacent Limburg areas. Due to unusually heavy precipitation in the Maas catchment area, river discharge increased to the point where it exceeded the river's maximum discharge capacity (ENW, 2021). The water level was nearly equal to the crest level of the dikes in several places. Considering the extreme conditions, the primary flood defences in Limburg performed quite well, as only a relatively small number of calamities and incidents have been reported. However, some dikes needed to be reinforced with sandbags (see Figure 1.1), and a small number of local dikes failed, causing damage and the need to evacuate (ENW, 2021).

Only 13 piping incidents have been reported along the Maas and its tributaries in Limburg and Noord-Brabant as a result of the flood event (ENW, 2021). With such extreme water levels, it was expected that piping would cause more problems for the dikes in Limburg. In her thesis, Verhulst (2017) proposed that piping is a real risk when the dikes' critical water levels are exceeded. Furthermore, during the most recent national dike assessment, a large number of dikes have been judged to be insufficiently safe for piping. As part of the Hoogwaterbeschermingsprogramma (HWBP), these dikes are reinforced against piping (HWBP, 2022). The discrepancy between the low number of piping observations as a result of the flood event and the fact that piping is regarded as a potential threat in Limburg raises concerns about Limburg's current piping assessment method for dikes.

The Sellmeijer conceptual model (Sellmeijer, 1988) serves as the foundation for the standard piping assessment rule in the Netherlands. This design rule is known as revised Sellmeijer rule (Rijkswaterstaat, 2021) because the original design rule (Sellmeijer, 1988) was revised several times before it reached its final form. Due to the calibration of the revised Sellmeijer rule, the application of the design rule is limited to the parameter bounds used in the calibration experiments. The parameter values associated with Limburg dikes may fall outside the parameter bounds of the Sellmeijer design rule (Sellmeijer et al., 2011). As a result, Waterschap Limburg assesses piping in Limburg using an adapted version of the revised Sellmeijer rule (Waterschap Limburg, 2020).

Figure 1.1: Reinforcement of the dike with sandbags near Buggenum (De Limburger, 2021)

1.3. Thesis objective

The objective of this thesis is:

To assess the applicability of the Sellmeijer design rule in the northern Maasvallei in Limburg and make an improved estimation of piping when necessary.

To achieve the objective, several research questions are proposed to break down the main objective into more graspable pieces. The first question is about gaining an understanding of the current piping assessment and the hydrogeological conditions in Limburg. The other research questions are about developing a finite element groundwater model for dike cross-sections in Limburg, performing a piping assessment with the proposed models, and assessing the applicability of the Sellmeijer design rule for Limburg dikes. The following research questions are formulated to achieve the objective of the thesis:

1. What are the primary reasons why the Sellmeijer design rule may not apply to Limburg dikes?
2. How can piping in Limburg hydrogeological systems be modeled?
3. What are the primary differences in the results of the safety assessment between the Sellmeijer conceptual model and the finite element model?
4. When Limburg parameter values are included in the design rule calibration using the finite element model, how does the Sellmeijer design rule change?

The finite element model is developed in the software COMSOL Multiphysics (COMSOL), which provides a flexible modelling environment for porous-media calculations. This software has not been used before to assess piping in Limburg.

1.4. Scope

To improve research quality, the following limitations have been imposed, which form the scope of this thesis:

• The research is performed for river dikes in Limburg that serve as primary flood defences.
• The dike sections containing water-retaining structures (e.g., locks, pumping stations, and divers)

are not included in this work. The transition between the construction and the dike may jeopardise the "water-proofness" of the dike and result in piping. This thesis focuses on standard dike sections where the seepage length includes the dike's total width and results in horizontal piping.

- This research only looks at backward erosion piping that occurs after uplift and heave. Uplift and heave assessments are not conducted because these processes are not assessed using the Sellmeijer design rule.

- Research is limited to trying to get a better estimate for the Sellmeijer limit state equation. Other piping design models/rules are disregarded.

- The research is based on the results from numerical models. It is not intended to perform physical experiments.

- The dike sections at four research locations, appointed by Waterschap Limburg, in the northern Maasvallei are being studied: Thorn (79.037), Hout-Blerick (70.075), Buggenum (75.030), and Well (60.070) (see Figure 1.2).
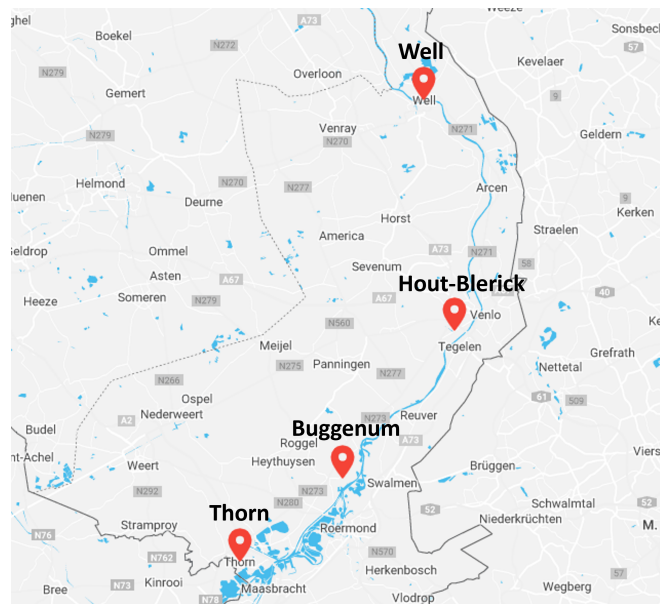
Figure 1.2: Research locations in Northern Limburg (Google, 2022)

1.5. Report structure

The report is structured according to the research questions of Section 1.3 and concludes by answering the thesis objective. Each chapter is briefly described below.

Chapter 2 focuses on the theory and background needed to understand the rest of the work. The chapter begins with an elaboration on groundwater flow corresponding hydraulic head development for a standard dike geometry, which includes an explanation of one of the main concepts: the hydraulic head gradient. Furthermore, the piping failure mechanisms and assessment methods are evaluated. The Sellmeijer design rule is explained in greater detail than any other assessment method because understanding the evolution of the design rule is critical. Finally, the general characteristics of Limburg's geohydrological system are examined in order to understand why the piping assessment in Limburg differs from that of the rest of the Netherlands.

The following chapter (Chapter 3) describes the development of the numerical models used to evaluate piping. This chapter explains the main principles and schematization choices used in the numerical model to simulate piping. The schematization of Limburg research locations into cross-sectional models is then explained. Finally, the numerical model calibration is discussed.

The deterministic piping assessment results are discussed in Chapter 4. For each research location, piping was evaluated analytically using the Sellmeijer design rule and numerically using the proposed

cross-sectional model.

Chapter 5 describes how the proposed cross-sectional models are used to assess piping stochastically. A total of 1000 randomly generated dike cross-sections are assessed on piping. Afterwards, the piping failure scenarios are used to evaluate the Sellmeijer design rule and calculate a fit factor for applying the Sellmeijer design rule in Limburg.

The final chapters are this thesis' discussion (Chapter 6), and conclusion and recommendations (Chapter 7). In Chapter 6 the results of the previous chapters are interpreted and the imperfections of the proposed numerical model are discussed. Afterwards, the thesis objective and research questions are answered in Chapter 7 and recommendations for further research are addressed.

<div style="text-align: right; font-size: 3em;">2</div>

Theory and background

The objective of this chapter is to get a better understanding of the failure mechanism piping. To begin, the basic principles of internal erosion and backward erosion are analyzed to get a sense of the processes that drive the failure mechanism. Afterwards, several piping assessment methods are introduced and the Sellmeijer design rule is elaborated. Finally, piping in Limburg is analyzed.

2.1. The piping failure mechanism

Piping is a type of internal erosion in which soil particles are washed beneath the dike until underground pipes form beneath it and the dike collapses. The piping failure mechanism is divided into three sub-mechanisms: uplift, heave, and (backward erosion) piping. Because the total failure mechanism and the final sub-mechanism have similar titles, the total failure mechanism is referred to as the piping failure mechanism throughout the rest of this thesis.

2.1.1. Flow beneath the dike

Piping is a phenomenon caused by a high outside water level that stands against the dike as a result of a flood or storm event (see Figure 2.1). The water levels are expressed in terms of the hydraulic head (H [m]). As the outer hydraulic head rises, the pore pressure in the aquifer and dike rises as well. When the pore pressure on the dike and the aquifer's outer side exceeds the pore pressure in the hinterland, the seepage flows in the direction of the hinterland (Q).
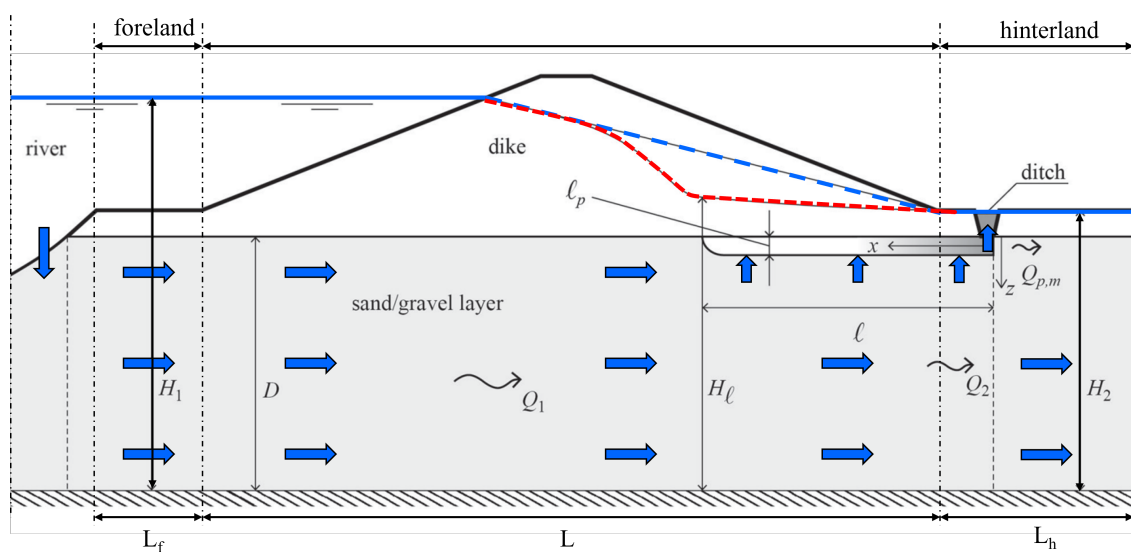
Figure 2.1: Definition sketch of piping (Hoffmans & Van Rijn Emeritus Professor, 2017)

Figure 2.1 shows the definition sketch of piping (Hoffmans & Van Rijn Emeritus Professor, 2017). During a high water level event when the pipe has not yet developed, the blue dashed line represents the hydraulic head development across the dike. The hydraulic head across the dike is influenced by the presence of a pipe in the aquifer (red dashed line), because due to the high permeability of the pipe, groundwater can easily travel to the hinterland.

For piping, seepage water must flow beneath the dike to the surface or a ditch in the hinterland, which occurs if the outer head is higher than the inner hydraulic head ($H_1 > H_2$ in Figure 2.1). The amount of seepage flow beneath the dike is determined by the aquifer's resistance and the increase in pore pressure caused by the outer hydraulic head. The vertical permeability of the cover layer determines groundwater drainage. Because groundwater follows the path of least resistance, it will exit the aquifer through cover layer cracks if they exist (Deltares, 2018).

The potential seepage length is the distance in the subsoil between the potential water entry and exit points. Groundwater follows the path of least resistance and thus travel the shortest distance between the entry and exit points. Because groundwater enters and exits through the foreland and hinterland, the dike width (L [m]) is the minimum potential seepage length. If the entry or exit point is far from the dike, the seepage length is the sum of the dike width, distance to the entry point in the foreland, and distance to the exit point in the hinterland from the dike.

Hydraulic head gradient is the change in hydraulic head along a groundwater path that is often expressed horizontally ($\frac{dh}{dx}$) or vertically ($\frac{dh}{dz}$). The hydraulic head difference across the dike and the hydraulic head gradient form the driving loads for the piping sub-mechanisms (Deltares, 2018):

- The cover layer is lifted and cracks are formed due to a critical hydraulic head difference across the cover layer.
- In a sand boil, the hydraulic gradient can cause heave.
- The pipe lengthens as a result of the hydraulic gradient at the tip of the pipe.

Time dependent load
Piping is also a time-dependent process. The water level development of the water body outside the dike depends the load duration working on the dike. River dikes are subjected to high water levels as a result of flood events that can last several weeks. The river water level associated with a flood event slowly rises to a maximum before gradually decreasing (see Appendix C). This results in a relatively long load duration compared to sea dikes, which depend, among other things, on short storm conditions. If the duration of the load exceeds the time required for the entire piping process, piping can lead to dike failure (Deltares, 2018).

2.1.2. Process description and (sub-)mechanisms
Figure 2.2 shows the primary processes of which the piping failure mechanism consists. Several processes must be preceded before piping can occur and cause dike failure. Below, the processes that lead to dike failure due to piping are described in chronological order (Deltares, 2012):

0. The possibility of seepage beneath the dike and cover layer in the direction of the hinterland is the first condition for piping to occur. Because of its impermeable properties, the cover layer is also known as an aquitard. The discharge beneath the dike is determined by the thickness and permeability of the aquifer.

1. When the water level on the dike's outer side rises, so does the seepage discharge under the dike. As a result, the pore pressure beneath the cover layer behind the dike rises until it exceeds the cover layer's weight. This is when the cover layer experiences uplift.

2. Excess pore pressure eventually causes cracks to form in the cover layer. Groundwater flows towards the leak in the cover layer and up through the cracks to the surface. A vertical canal develops through the cover layer due to erosion and forms an open connection between the surface and aquifer. A decrease in pore pressure is observed near the vertical canal.

3. The sand particles are carried to the surface through the exit canal as soon as the hydraulic head gradient across the vertical canal exceeds the critical gradient corresponding to the stability of the sand particles at the bottom of the pipe. Heave refers to the fluidization of sand particles that forms
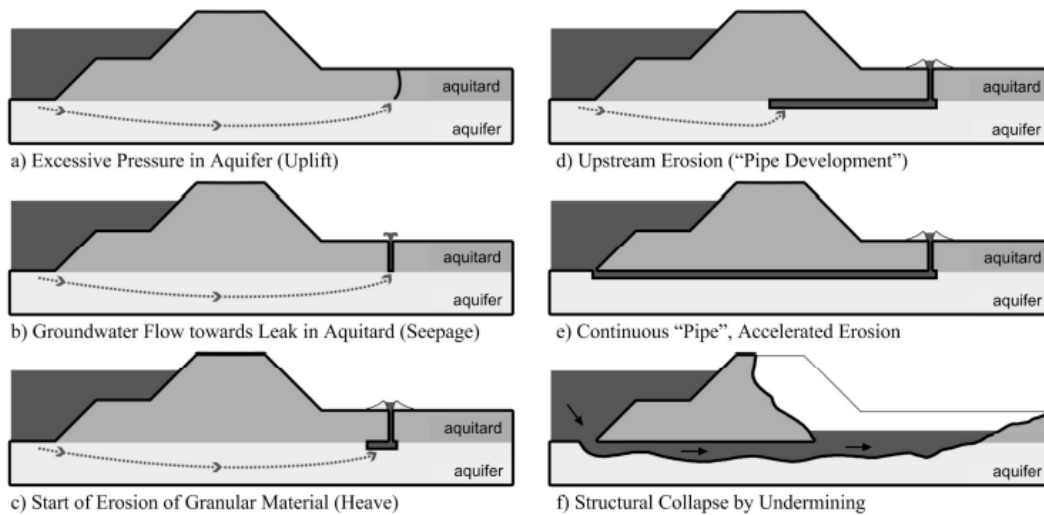
Figure 2.2: Phases of piping (Jonkman et al., 2021)

the beginning of the pipe. When the particles are flushed to the surface, they accumulate around the opening in the cover layer, forming a sand boil. The hydraulic head gradient is explained in Section 2.1.1.

4. (Backward erosion) piping continues until a continuous small pipe has formed beneath the dike along the potential seepage path as long as the hydraulic gradient exceeds the rolling resistance of the grains.

5. When a continuous pipe has formed the erosion process continues in the form of widening and deepening of the pipe. This process is driven by the difference in water pressure between the entrance and exit points of the pipe.

6. Eventually, a hollow clearing forms beneath the dike, causing the flood defence to fail. However, for safety assessments, the development of a continuous pipe along the potential seepage path is already regarded as failure of the flood defence.

2.1.3. Assessment of the submechanisms

In the Netherlands, the primary flood defences are assessed every 12 years. In each assessment round the safety corresponding to piping is assessed using prediction models. For many river dikes, piping forms a realistic risk, but remains difficult to predict. That is the reason why much attention has been paid to piping in the past and it still remains an important research topic. However, piping failure can only occur if the uplift, heave, and backward erosion limits are exceeded. That is why all sub-mechanisms of piping have to be assessed.

Uplift

As told before, uplift occurs when the pore pressure in the aquifer in the hinterland exceeds the weight of the cover layer. This process is expressed in the following limit state function (Jonkman et al., 2021):

$$Z_u = m_u \Delta\phi_{c,u} - \Delta\phi$$
$$\Delta\phi_{c,u} = D\frac{\gamma_{sat} - \gamma_w}{\gamma_w} \tag{2.1}$$
$$\Delta\phi = \phi_{\text{exit}} - h_p$$

From Equation 2.1 can be seen that uplift depends on the balance between the critical head difference ($\Delta\phi_{c,u}$ [m]) which is expressed in the weight of the cover layer, as γ_{sat} [kN/m^3] is the saturated volumetric weight of the cover layer, γ_w (= 10 kN/m^3) is the volumetric weight of water, and D ([m]) is the depth of the cover layer at the exit point. The load is described by the difference in potential at the exit

point ($\Delta\phi_{\text{exit}}$) and the phreatic level at the hinterland (h_p [m]). If the load is greater than the resistance ($Z_u < 0$) uplift occurs.

Heave

When uplift has occurred heave is the next sub-mechanism that must occur to eventually lead up to dike failure due to piping. Heave is concerned with the start of the erosion of sand particles from the aquifer. That means that the critical heave gradient ($i_{c,h}$ [-]) must be exceeded by the exit gradient (i [-]) (Jonkman et al., 2021):

$$Z_h = i_{c,h} - i$$
$$i_{c,h} = \frac{(1-\epsilon)\,(\gamma_s - \gamma_w)}{\gamma_w}$$
$$i = \frac{(\phi_{\text{exit}} - h_p)}{D}$$

(2.2)

Whereas, the critical heave gradient is a function of porosity (ϵ [-]) and the volumetric weight of quartz ($\gamma_s = 26.5$ kN/m^3) and the volumetric weight of water. The other parameters have been introduced in Equation 2.1.

(Backward-erosion) piping

When the heave criterion is exceeded, (backward erosion) piping starts. In this thesis backward erosion and piping are both considered with the sub-mechanism that concerns the development of pipes beneath the dike. This process was first scientifically described by Bligh in 1910. Bligh developed an empirical design rule based on the analysis of several collapsed dams on various earth foundations (Deltares, 2012):

$$\Delta H \leq \Delta H_c = \frac{L}{C_{creep}}$$

(2.3)

Where:

ΔH [m]: the present head difference across the flood defence (= H-h$_p$)

ΔH_c [m]: the critical head difference across the flood defence

L [m]: the minimum seepage length

C_{creep} [-]: creep factor

Bligh has provided a number of values for the creep factor, depending on the estimated grain size of the sand in the aquifer. In this design rule, the influence of vertical structures beneath the dike is accounted for by summing the vertical and horizontal seepage length for the minimum seepage length in the design rule (Deltares, 2012). However, Lane (1935) harshly criticized how Bligh took into account the influence of vertical seepage paths. Lane analysed a large number of dams and focused on the differences in horizontal and vertical seepage length. He found that the resistance along the vertical seepage paths is three times higher than along the horizontal seepage paths. The rules of Bligh and Lane are derived in a similar manner in which both the critical head gradient of existing weirs and dams have been plotted against the corresponding seepage length. Subsequently, a lower limit was chosen that was considered sufficiently safe (Deltares, 2012).

The revised Sellmeijer rule, as proposed by Sellmeijer et al. (2011) and Rijkswaterstaat (2021), is currently the standard piping assessment rule in the Netherlands. The revised Sellmeijer rule is proven to be less conservative and safer than Bligh's rule (Deltares, 2012). The Sellmeijer design rule is discussed in detail in Section 2.2

2.1.4. Piping sensitive subsoil characteristics

Not every subsoil structure allows the piping failure mechanism to occur. Local subsoil structures can already indicate whether piping is an important failure mechanism to consider. This subsection summarizes the characteristics of the subsoil that lead to a sensitive and insensitive subsoil structure of the pipe (Deltares, 2012).

Characteristics of a piping sensitive subsoil structure:

- The most basic piping-sensitive subsoil structure is a clay dike with a cohesive (impermeable or low permeable) cover layer (aquitard) on top of a permeable sand layer (aquifer) (see Figure 2.2).

- A subsoil structure composed of multiple sand layers underlying a cover layer made of cohesive material. The piping criteria should be checked for all sand layers present.

- The entry point for seepage shifts in the direction of the open water if the flood defence has a cohesive cover layer on the foreland. The seepage length increases in proportion to the width of the foreland. However, if the cover layer contains weaknesses on the foreland, the normative seepage length is determined by the shortest distance to the possible entry point.

Characteristics of a piping insensitive subsoil structure:

- Piping requires an aquitard, which serves as the pipe's roof (see Figure 2.2). However, dikes made entirely of sand or with a sand foundation connected to the aquifer cannot provide this condition.

- When dikes are mostly made of sand or are not (fully) covered by a cohesive top layer, piping does not form an important failure mechanism. Seepage can outflow the structure at any point. Seepage can flush soil particles from the dike core, resulting in slope failure. This failure mechanism is known as micro-instability.

The Potential seepage length is another condition that can quickly indicate the risk of piping, because the pipe must develop until the pipe length is equal to the width of the dike and the additional potential seepage path behind the dike to lead to failure. A long potential seepage path indicates that the seepage encounters significant soil resistance and requires a long load duration for the pipe to develop along the entire path. If the sum of the dike width and the potential seepage path is unrealistically large, the structure can be regarded as insensitive to piping.

2.2. The Sellmeijer design rule

The original Sellmeijer design rule (Sellmeijer, 1988) is based on the conceptual Sellmeijer model, which theoretically describes the physical processes of piping. With the help of experiments, the original design rule was recalibrated to become the revised Sellmeijer design rule Sellmeijer et al. (2011) that is now used for piping assessments (Van Esch, 2014). However, the original rule's base assumptions remain the foundation of today's Sellmeijer rule. As a result, understanding the evolution of the Sellmeijer rule is critical.

2.2.1. Model principles

Many experiments of varying scales have been conducted in the past to investigate backward erosion piping. The pressure gradient caused by a difference in water level across a structure induces seepage flow in the subsoil. When the flow initiated by the hydraulic gradient is sufficiently powerful, erosion occurs under the structure in the form of pipes, and the eroded sand forms a sand boil at the seepage exit point (Sellmeijer & Koenders, 1991). The formed pipe has a much higher permeability than the surrounding subsoil, which dampens the hydraulic gradients that initiate the erosion process and leads to an equilibrium state for a given hydraulic gradient value (Sellmeijer & Koenders, 1991). Visual tests show that after a change in hydraulic head, the seepage flow grows to a steady state. As a result, steady-state flow equations can be used to describe seepage flow (Sellmeijer, 1988). Because sand erosion can only begin when sand particles are set in motion, the limit equilibrium of sand must be determined in the sand boil and in the pipe. The critical hydraulic gradient is also linked to the sand limit equilibrium (Sellmeijer, 1988).

Another main principle of the Sellmeijer model is that a two-dimensional approach is used to describe piping. According to Sellmeijer (1988), using a two-dimensional approach rather than three-dimensional, should not have a negative impact on the quality of the results because the main mechanical features are properly described. However, it is not possible to implement meandering of the pipes in the analysis, since this is a three-dimensional feature associated with the heterogeneity of the sand properties.

(a) Standard dike geometry

(b) Model simplification with geometry parameters
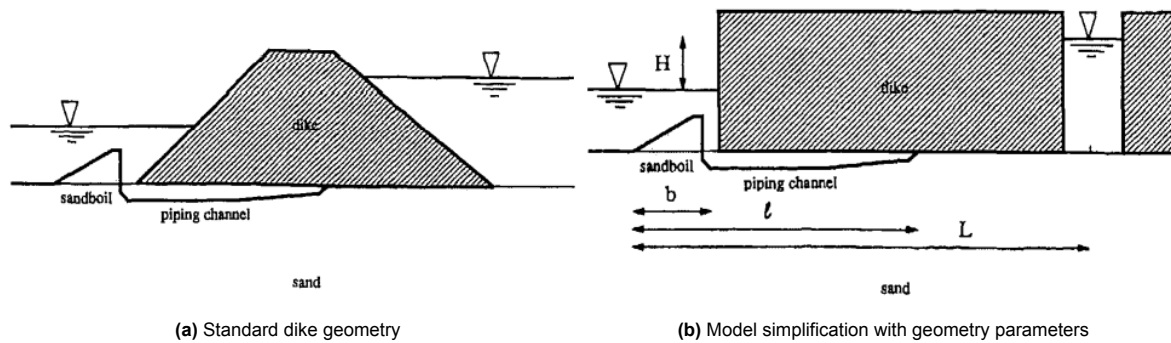
Figure 2.3: Dike geometry in the Sellmeijer model (Sellmeijer & Koenders, 1991)

The assumption of laminar flow through the pipe and the assumption that erosion occurs solely under the structure, are two more important principles of the Sellmeijer model. The resistance caused by the geometry of the sand boil and the pipe is considered. In the Sellmeijer conceptual model the length of the pipe is equal to 44% of the dike width. This is considered the critical pipe length, and if it is exceeded, piping will proceed independently of the load conditions, resulting in dike failure (Sellmeijer, 1988).

Sellmeijer mathematically described three processes that contribute to piping in his model using the schematization choices and assumptions mentioned above (Sellmeijer & Koenders, 1991):

- Under the dike or structure, groundwater flows from the foreland to the pipe and the hinterland.
- Flow through the pipe.
- The stability of the grains at the bottom of the pipe.

Geometry and boundary conditions
The Sellmeijer model's hydrological system is derived from a straightforward dike geometry (see Figure 2.3a). The dike has horizontal bottom with length (L [m]) and is considered to be made of a fully impermeable material, that also acts as a roof of the developing pipe. The system's subsoil consists of a permeable homogeneous aquifer made of sand. The hydrological system is set in motion by the difference in hydraulic head (H [m]) across the dike, which gives rise to seepage through the aquifer to the side with the lowest water head. In the geometry shown in Figure 2.3b, the sand boil and pipe have been drawn including the corresponding parameters.
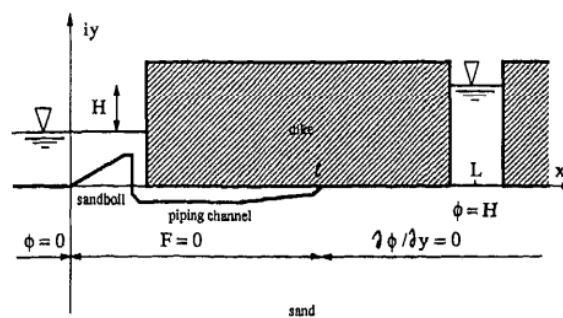
Figure 2.4: Overview boundary conditions (Sellmeijer & Koenders, 1991)

A Cartesian coordinate system is used to define the model's system and to specify the boundary conditions (see Figure 2.4). The piezometric head and its derivative are used to express the model's boundary conditions. The gradient increases as the head difference between the foreland and hinterland increases. For x < 0, the head and the horizontal head gradient are constant ($\phi = 0$, $d\phi/dx = 0$) due to the presence of the free water surface. At x = L, the head is fixed for $\phi = H$ in which H indicates the hydraulic head on the outside the dike. Because a steady state function is used, H, which typically

changes with the water level of the water body, is set to be fixed. For $l < x < L$, the vertical discharge vanishes (head gradient $d\phi/dy = 0$) due to the impermeable material of the dike. However, in between the sand boil and the tip of the pipe the boundary conditions are described by the erosion processes in the pipe (Sellmeijer, 1988).

The groundwater flow calculations are solved for these boundary conditions by expressing the head in the pipe as a variable. As a result is found that piping depends on seepage flow through the aquifer and the limit equilibrium of sand particles in the pipe.

2.2.2. The first Sellmeijer design rule (1988)

Each Sellmeijer design rule describes the relationship between the critical head for which piping occurs (H_c [m]), the seepage length (L [m]) and the erosion coefficient (c [-]). During his thesis Sellmeijer found that the relevant variables for his design rule can be grouped into meaning full clusters:

$$\frac{H_c}{L} = \frac{H}{L}\left(\frac{l}{L}; \frac{\kappa}{D^2}, \frac{D}{L}, \Phi, \theta, C, \eta, \frac{\gamma_{sp}}{\gamma_w}, \frac{\gamma_s}{\gamma_w}\right) \tag{2.4}$$

where:

> H_c [m]: critical head
>
> L [m]: potential seepage length
>
> H [m]: Hydraulic head of the outside water body
>
> l [m]: length of the pipe
>
> κ [m^2]: intrinsic permeability
>
> D [m]: thickness of the aquifer
>
> θ [deg]: embedment angle of sand particles
>
> η [-]: White's packing coefficient (0.25)
>
> γ_{sp} [kN/m^3]: submerged volumetric weight of soil particles
>
> γ_w [kN/m^3]: volumetric weight of water
>
> γ_s [kN/m^3]: volumetric weight of soil

From the clusters can be seen that H/L is the typical design quantity and all other variables are site specific water and soil characteristics (Sellmeijer & Koenders, 1991). The first version of the Sellmeijer design rule (Sellmeijer, 1988) is found by solving the conceptual model and using dimensional analysis and multi-variate regression methods:

$$\frac{H}{L} = c\frac{\gamma_{sp}}{\gamma_w}\tan\theta\left(1 - 0.65c^{0.42}\right)$$
$$c = \frac{1}{4}\pi\eta\sqrt[3]{\frac{D^2}{\kappa}\frac{D}{\frac{1}{2}L}} \tag{2.5}$$

When applying the design rule, a representative particle diameter between d_{65} and d_{75} should be used, because finer grains are easier set in motion than larger particles (Sellmeijer, 1988). Therefore, the resistance against erosion depends on larger grains.

However, soon after this design rule was published Sellmeijer acknowledged two major shortcomings in his mathematical model: the impermeable cover layer present in the hinterland was not considered and the aquifer was described having a infinite thickness (Barendsen, 2020). In 1989, Sellmeijer improved his mathematical model with more realistic geometry, such as an impervious cover layer in the hinterland and a finite-thickness aquifer. This changed the boundary conditions of the hinterland cover layer and the model's lowest boundary to $d\phi/dy = 0$, resulting in the disappearance of the vertical discharge. The second version of the Sellmeijer design was created by running a large number of simulations with the new geometry and boundary conditions and applying curve fitting (Barendsen, 2020).

$$\frac{H_c}{L} = \frac{1}{c} = F_R F_S F_G$$

$$F_R = \eta \frac{\gamma_{sp}}{\gamma_w} \tan \vartheta$$

$$F_S = \frac{d_{70}}{\sqrt[3]{\kappa L}}$$ (2.6)

$$F_G = \{0.68 - 0.1 \ln (\eta F_S)\} \left(\frac{D}{L}\right)^{\frac{0.28}{\left(\frac{D}{L}\right)^{2.8} - 1}}$$

For simplicity and clarity the design rule is divided in the resistance factor (F_R [-]), scale factor (F_S [-]) and the geometric factor (F_G [-]). The inclusion of the geometric factor is the newest addition to the design rule.

2.2.3. Two force equilibrium

There has been some debate about whether the piping model should be based on a four forces equilibrium working on the sand grains at the bottom of the pipe. It is argued that at limit equilibrium, the sand grain is not buried deep between other grains, but rather protrudes from the pipe bottom. This implies that the flow forces have no effect on the grain and that only the grain weight and drag force must be considered. As a result, the geometric factor is changed to a two-force equilibrium. However, it must be noted that the new geometric factor is only valid for a sand layer with a constant thickness (Sellmeijer et al., 2011).

$$F_G = \{0.68 - 0.1 \ln (\eta F_S)\} \left(\frac{D}{L}\right)^{\frac{0.28}{\left(\frac{D}{L}\right)^{2.8} - 1}} \quad \Rightarrow \quad F_G = 0.91 \left(\frac{D}{L}\right)^{\frac{0.28}{\left(\frac{D}{L}\right)^{2.8} - 1} + 0.04} \quad (2.7)$$

The original Sellmeijer design rule has been updated with the new geometric factor. This version of the design rule is referred to throughout this thesis as the 'original Sellmeijer design rule (Sellmeijer, 1988) with the new geometric factor (Sellmeijer et al., 2011)'. Equation 2.8 depicts one of the design rules whose applicability is evaluated in this thesis.

$$\frac{H_c}{L} = \frac{1}{c} = F_R F_S F_G$$

$$F_R = \eta \frac{\gamma_{sp}}{\gamma_w} \tan \vartheta$$

$$F_S = \frac{d_{70}}{\sqrt[3]{\kappa L}}$$ (2.8)

$$F_G = 0.91 \left(\frac{D}{L}\right)^{\frac{0.28}{\left(\frac{D}{L}\right)^{2.8} - 1} + 0.04}$$

2.2.4. Adapted Sellmeijer rule (2011)

Van Beek et al. (2011) conducted a series of small-, medium-, and large-scale piping experiments to get a better understanding of the physics of the piping phenomenon. Because only sufficient small-scale experiments are carried out for statistical analysis and a multivariate regression, Equation 2.8 is adapted based on the results of the small- and medium-scale experiments (Sellmeijer et al., 2011). As a result, multivariate expression factors are determined that express the influence of each factor on the critical head (see Table 2.1). Equation 2.9 displays the adapted version of the Sellmeijer design rule (Sellmeijer et al., 2011), which was validated with three large-scale field experiments. The adapted Sellmeijer design rule (Equation 2.9) now includes the influence of the relative density (RD), uniformity (U) and angularity (KAS) in the resistance factor. The scale factor is modified to reflect the measured role of particle size (Sellmeijer et al., 2011).

Table 2.1: Multivariate regression factors (Van Beek et al., 2011)

	RD	κ	d_{70}	U	KAS	fitting
	0.35	-0.35	0.40	0.13	-0.02	-0.079

When combining Equation 2.8 and the results of the multivariate analysis, the adapted Sellmeijer design rule looks like:

$$\frac{H_c}{L} = \frac{1}{c} = F_R F_S F_G$$

$$F_R = \eta \frac{\gamma_{sp}}{\gamma_w} \tan\vartheta \left(\frac{RD}{RD_m}\right)^{0.35} \left(\frac{U}{U_m}\right)^{0.13} \left(\frac{KAS}{KAS_m}\right)^{-0.02}$$

$$F_S = \frac{d_{70m}}{\sqrt[3]{\kappa L}} \left(\frac{d_{70}}{d_{70m}}\right)^{0.4}$$

$$F_G = 0.91 \left(\frac{D}{L}\right)^{\frac{0.28}{\left(\frac{D}{L}\right)^{2.8}-1}+0.04}$$

(2.9)

The extension and adaption of the original Sellmeijer rule are solely of empirical nature, consequently the application is limited to the range of parameters used during the experiments (Sellmeijer et al., 2011). These parameter limits are:

Table 2.2: Parameter limits (Sellmeijer et al., 2011)

parameter	minimum	maximum	mean
RD	50%	100%	72.5%
U	1.3	2.6	1.81
KAS	35%	70%	49.8%
d_{70}	150 μm	430 μm	208 μm

2.2.5. Current piping assessment rule

The Dutch government prescribes how piping should be assessed in statutory assessment tools (WBI-2017). It specifies that piping should be assessed using another version of the Sellmeijer design rule (see Equation 2.10), known as revised Sellmeijer design rule (Rijkswaterstaat, 2021). In this version the influence of the relative density, uniformity and angularity is not included.

$$\frac{H_c}{L} = \frac{1}{c} = F_R F_S F_G$$

$$F_R = \eta \frac{\gamma'_{sp}}{\gamma_w} \tan\theta$$

$$F_S = \frac{d_{70m}}{\sqrt[3]{\kappa L}} \left(\frac{d_{70}}{d_{70m}}\right)^{0.4}$$

$$F_G = 0.91 \left(\frac{D}{L}\right)^{\left(\frac{0.28}{\left(\frac{D}{L}\right)^{2.8}-1}+0.04\right)}$$

(2.10)

The applicability of the revised Sellmeijer design rule is also evaluated in this thesis, as this design rule is currently used to assess piping in practice.

2.3. Piping in Limburg

Whereas the Sellmeijer model's hydrogeological system is completely homogeneous and straightforward (see Section 2.2 and Figure 2.3), real hydrogeological systems are heterogeneous, uncertain,

and almost never homogeneous. It is certain that the hydrogeological system in Limburg is not straight-forward, because the subsoil composition has great variety. Figure 2.5 shows a sketch of the subsoil in Well and perfectly depicts the complication of the Limburg subsoil. The colours in the figure represent gravel (orange) and clay (grey) layers. The influence of layer heterogeneity and variation in layers across the cross-section complicates piping assessment in Limburg.

Figure 2.5: Sketch of the subsoil composition for research location in Well (Koopmans & Janssen, 2018)

2.3.1. General soil characteristics

During the project 'POV Piping - Invloed Maasklei en Grindlagen' (Koopmans & Janssen, 2018) multiple laboratory and pumping tests have been performed to get a better understanding of the cover layer, layer composition and geological characteristics in the Maasvallei. It is known that the subsoil composition in Limburg consists mainly of clay, sand and gravel. Afterwards, in 2018 and 2019, Van Beek performed two analyses in which the piping sensitivity of coarse sand and gravel samples of 'POV Piping - Invloed Maasklei en Grindlagen' (Koopmans & Janssen, 2018) were studied by comparing the samples with older experiments from literature. The findings of these studies provide a brief idea of the geological characteristics of the present subsoil layers.

Cover layer

Koopmans & Janssen (2018) used triaxial tests to investigate whether the cover layer consists of cohesive material. According to these tests, the soil material acts as a cohesive material for small deformations (elongation of 0.5-2.0%) but not for larger deformations (>25%) (Koopmans & Janssen, 2018). Uplift and bursting of the cover layer in piping can be considered small deformations, so the layer acts as a cohesive material in these mechanisms. The layer's cohesion allows for the formation of a vertical open channel through which seepage water can reach the surface.

The hydraulic conductivity of the cover layer is investigated by Koopmans & Janssen (2018) using porchet and ring tests, which were performed for several research locations. The cover layer in the Maasvallei has a hydraulic conductivity range of 0.2-0.6 m/d. Limburg clay is fairly to moderately permeable to water, as are soil materials with a hydraulic conductivity less than 1 m/d. The low hydraulic conductivity in the cover layer indicates that pressure can build up underneath the layer, leading to uplift of the cover layer (Koopmans & Janssen, 2018).

The dikes in Limburg have a relatively low retaining height, as a result the groundwater potentials under the cover layer are not as extreme (Koopmans & Janssen, 2018). The combination of perceived hydraulic conductivity and the potential beneath the cover layer, indicates that there is no concentrated seepage stream leading to the surface, but rather uniform seepage occurs through the cover layer.

Sand

Sand in the northern Maasvallei in Limburg is considered to be coarse because it frequently contains gravel fractions. Koopmans & Janssen (2018) conclude that the coarse sand layer beneath the cover layer contains 10% gravel on average, but the standard deviation is quite large (v = 1.0). This means that sand layers can have a gravel fraction of 30% or 0%. In practice, the sand layer in Thorn has a high probability of containing gravel, but the sand layers in Buggenum and Well may also contain gravel.

Van Beek (2018) compares the samples of sand layers containing gravel from the pump test in Thorn (Slot, 2016) with sieve curves from experiments by Townsend et al. (1988) and Allan (2018) (see Figure 2.6). The samples of Townsend et al. and Allan were tested in a laboratory to study geological properties and are used to compare the prediction of the revised Sellmeijer design rule (Equation 2.10) with physical experiments. As a result, differences are found between the resistance against piping of the experiments and the critical head according to Sellmeijer. Comparing the experimentally tested sieve curves with the Limburg sieve curves gives an idea of the strength of the Limburg geomechanical properties against piping, with respect to the corresponding critical head of the Sellmeijer design rule.

(a) Comparison with Townsend et al. (1988) (Van Beek, 2018)   **(b)** Comparison with Allan (2018) (Van Beek, 2019)
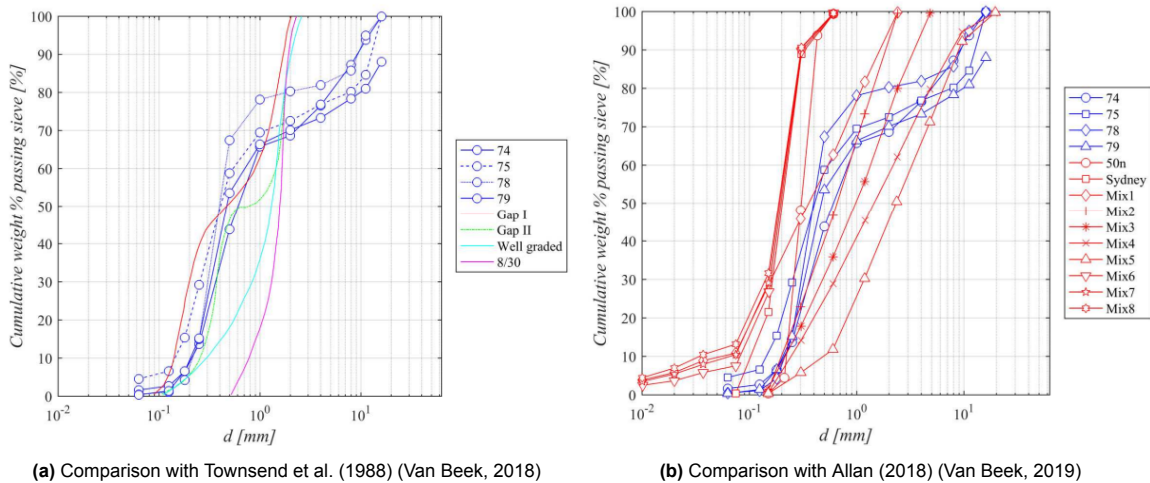
Figure 2.6: Sieve curve comparison of Limburg coarse sand samples and laboratory tested sand samples
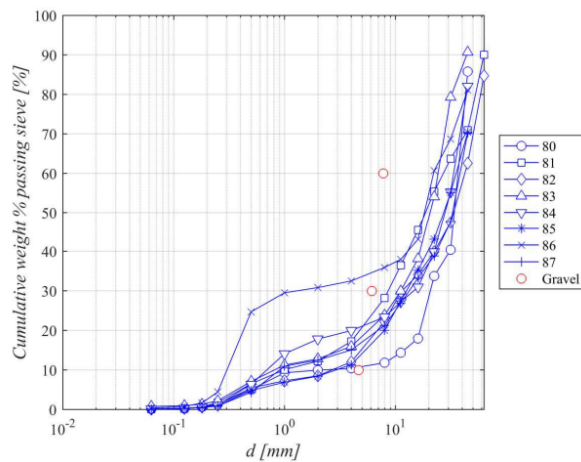
Figure 2.7: Comparison with Robbins et al. (2016) (Van Beek, 2018)

The sieve curves of Townsend et al. (1988) differ from the sieve curves of Limburg coarse sand. Despite this, the Gap-II sample has the highest likeliness, but the presence of the fine fraction indicates that this sample has a higher permeability than the Limburg samples. Van Beek (2018) argues that the Limburg coarse sand samples appear to be at least as strong against piping as the Gap-II sample because, while d_{70} is lower, d_{80} is significantly higher, and permeability is also an advantage for the Limburg samples. Van Beek (2019) contends that Mix1 to Mix5 of Allan (2018) provide a reasonable estimate of piping sensitivity, if the Limburg coarse sand samples are internally stable (as demonstrated by Koopmans & Janssen (2018)).

Van Beek (2019) concludes that the strength against piping of the coarse samples from Limburg is 1.8-5.5 times greater than predicted by the Sellmeijer model. It should be noted that this conclusion must be read with uncertainty for the influence of 3D outflow of water from the test domain compared with a 2D model in Sellmeijer.

Gravel
The same analyses are performed on gravel samples from the pump test in Thorn (Slot, 2016) as were done on Limburg coarse sand samples. The only difference is that these samples are taken from deeper gravel layers rather than directly beneath the cover layer. During the physical experiments, the gravel samples of Robbins et al. (2016) demonstrated a factor 2 increase in strength against piping when compared to the Sellmeijer model. In comparison to the Limburg gravel samples, the samples of Robbins et al. (2016) are more fine and uniform, favoring the Limburg gravel sample. That is why Van Beek (2018) contends that the strength against piping of the Limburg gravel samples is comparable to the strength of the Robbins et al. (2016) samples.

2.3.2. Current piping assessment in Limburg
Waterschap Limburg has identified three different piping assessment methods based on the subsoil structure for locations with gravel in the subsoil (Waterschap Limburg, 2020):

1. The gravel layer is the aquiferous layer.
2. The aquiferous layer consists solely of sand.
3. The aquifer consists of a sand layer on top of a gravel layer

When the aquiferous layer (the layer in which groundwater flows beneath the cover layer) consists of gravel, Waterschap Limburg uses an adapted piping assessment method. Limburg gravel layers can have a grain size greater than 10 mm, which exceeds the limits of Sellmeijer (see Table 2.2). Waterschap Limburg bases their adopted assessment method on the analyses of Van Beek (2018, 2019), which argues that the critical head gradient for sand layers containing gravel and gravel layers is a factor 1.8-5.5 greater than predicted with the revised Sellmeijer design rule (Equation 2.10). That is the reason why Waterschap Limburg includes a factor of 1.8 on the critical head gradient while using the Sellmeijer model to assess piping in gravel layers (Waterschap Limburg, 2020).

When the aquiferous layer consists solely of sand the revised Sellmeijer model (Equation 2.10) is used, without implementing an increase for the critical head gradient.

When the aquifer consists of a sand layer lying on top of a gravel layer, Waterschap Limburg argues that a two-layer system should be used. This means that the permeability of the system is described by the weighted average over the depth of the aquifer and the representative grain size (d_{70}) of the sand layer is used in the assessment. The piping assessment of the system is performed with the revised Sellmeijer model (Equation 2.10), without increasing the critical head gradient.

3

Construction of the finite element numerical model

The objective of this chapter is to describe how to build a two-dimensional calibrated finite element model (FEM) in COMSOL Multiphysics (COMSOL), to assess piping for varying dike cross-sections. The principles used to set up the model and analyse piping are based on the model and concept proposed by Aguilar-López et al. (2016a) in 'Piping erosion safety assessment of flood defences founded over sewer pipes'. Furthermore, the principles for analyzing piping are adapted to represent the principles that Sellmeijer (1988) applied in his conceptual model. The basic model and piping principles are elaborated in Section 3.1. Section 3.2 describes a set of operations to implement the principles and assumptions of the model in COMSOL.

Section 3.3 describes the schematization choices and assumptions that have been made to schematize four dike cross-sections in Limburg, into two-dimensional cross-sectional models. To begin, several general assumptions are discussed, followed by site-specific characteristics for each research location. To make the models as realistic as possible, they are calibrated to hydraulic head measurements from standpipes and pore pressure gauges of the 2021 flood event at the research locations. Section 3.4 describes the calibration process and the results.

3.1. Piping model principles

Some of the main model principles are based on the considerations implemented in the model of Sellmeijer (1988) in order to compare the results of the FEM numerical model to the Sellmeijer model (Sellmeijer, 1988). The piping erosion model is built in two dimensions (2D) for a steady-state equilibrium condition. Meaning, that piping is considered in a single pipe with given dimensions and the three-dimensional meandering of the pipe is neglected. Furthermore, water can only enter and exit the model at the specified boundary conditions at both ends of the model domain. This means that groundwater flow is also considered two-dimensional.

The piping model is chosen as a steady-state model as the limit equilibrium becomes independent of time. Another important principle is that only secondary erosion is considered in the model because Sellmeijer (1988) neglects the effect of primary erosion. These assumptions make it possible to test the occurrence of piping for fixed pipe lengths.

The equilibrium condition in the model is defined by the horizontal pressure gradient ($\frac{dp}{dx}$) working on the grains in the pipe and the rolling resistance of the grains. Throughout this thesis, the horizontal pressure gradient is expressed as the hydraulic head gradient ($\frac{dh}{dx}$) to gain a better understanding when comparing the hydraulic gradient to the hydraulic head development across the dike and pipe.

$$\frac{dp}{dx} = \frac{dh}{dx}\rho g \qquad (3.1)$$

where:

$\rho = 1000$ kg/m^3: density of water

$g = 9.81$ m/s^2: gravitational acceleration

The rolling resistance or stability of the grains is represented by the two forces equilibrium acting on a grain (Van Esch et al., 2013), as described in Section 3.1.2. It is assumed that if the hydraulic gradient exceeds the rolling resistance of the grains, erosion of the pipe progresses. According to Sellmeijer & Koenders (1991) this equilibrium becomes critical for a pipe that has developed until approximately the midpoint of the dike (0.44*L). If the equilibrium condition is exceeded at this point, erosion progresses continuously, independent of the loading conditions of the dike until the failure of the structure.

The boundary conditions of the piping erosion model can easily be divided into two types of conditions: Dirichlet and Neumann boundary conditions.
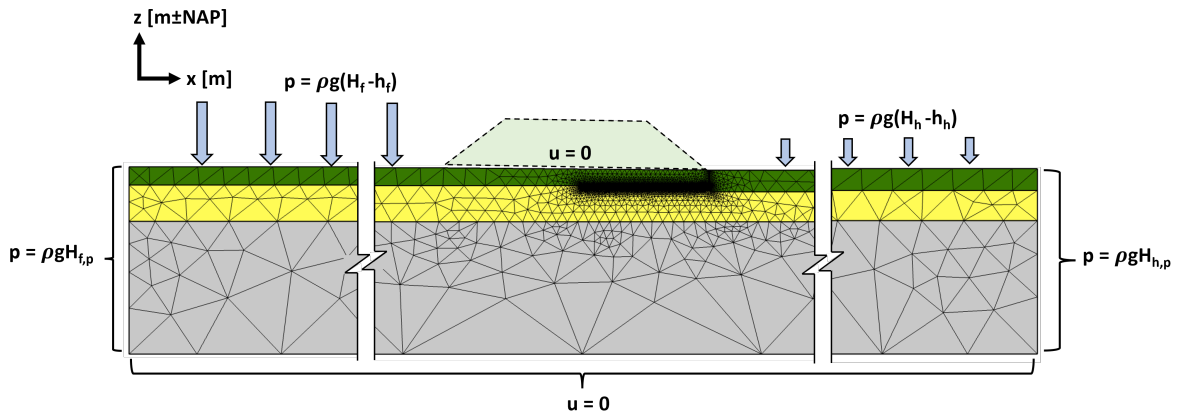
Figure 3.1: Schematization of the boundary conditions on the numerical model of Well; based on (Aguilar-López et al., 2016a)

The Dirichlet boundary conditions are defined by 'no-flow' ($u = 0$) conditions and are located on the bottom of the dike and the lowest boundary of the geometry and imply an impermeable boundary (see Figure 3.1). The dike is assumed to be fully impermeable. The implementation and details of the boundary conditions are elaborated on in Section 3.2.

The Neumann boundary conditions are defined by a hydraulic head at the two vertical and remaining horizontal boundaries of the model domain. At the foreland, the outside water level of the river or the critical water level according to Sellmeijer & Koenders (1991) (H_f) defines the boundary condition. On the hinterland side, the boundary condition of the water level is defined by the groundwater level (H_h). The groundwater level is set equal to the surface level to consider saturated soil conditions. The boundary conditions on the vertical boundaries are defined as hydrostatic pressure along the depth of the model geometry (see Figure 3.1).

3.1.1. Darcyan groundwater flow and fictitious permeability (load)

The FEM model simulates 2D subsurface flow in the soil geometry and solves Darcy's law for two-dimensional fluid flow through pores between soil particles in a predefined subsurface geometry. The groundwater flow in the aquifer is driven by the pressure gradient or the hydraulic head gradient and is slowed by the friction forces within the pores. For gradient-driven flow Darcy's Law is applied:

$$u = -\frac{\kappa}{\mu}(\nabla p + \rho g \Delta z) = -\frac{\kappa}{\mu}\rho g \nabla H \tag{3.2}$$

In which u ([m/s]) is the flow velocity through the porous media and ∇H is the hydraulic gradient (Bersan et al., 2013). In Equation 3.2, the intrinsic permeability (κ [m^2]) is introduced. The relationship between hydraulic conductivity (K [m/s]) and intrinsic permeability is expressed by Equation 3.3 and is a function of the fluid density (ρ [kg/m^3]) and dynamic viscosity (μ [kg/ms]) or kinematic viscosity (v [m^2/s]). The terms intrinsic permeability and hydraulic conductivity are often used interchangeably. However, they

have different definitions. Intrinsic permeability is the ability of a porous medium to transmit a fluid, which makes it a property of the porous medium only and independent of fluid properties. The ease with which a fluid can move through the pore space is described by hydraulic conductivity, which is determined by the viscosity of the fluid flowing through the media.

$$K = \frac{\kappa \rho g}{\mu} = \frac{\kappa g}{v} \tag{3.3}$$

The Navier-Stokes equation describes flow through an erosion channel. However, combining Navier-Stokes and Darcy's Law gives dependent boundary conditions for which the model domain is hard to solve. The fictitious permeability method is used in the piping model to simplify calculations (Bersan et al., 2013). This method simulates the pipe as a porous media domain or area with very high permeability, instead of a closed conduit (Wewer, 2019). The model can now be solved using Darcy's Law.

Hagen-Poiseuille flow is used to describe one-dimensional laminar and incompressible flow through a long pipe with a constant cross-section. The equation for general cross-sectional shapes is (Bersan et al., 2013):

$$U = \left(\frac{2D_h{}^2}{\beta_{fi}} \right) \left(\frac{g\rho}{\mu} \right) \frac{\Delta H}{L} \tag{3.4}$$

where:

    D_h [m]: hydraulic diameter of the pipe

    β_{fi} [-]: friction coefficient of the pipe cross-section

    L [m]: the length of the pipe

For which U ([m/s]) is the average flow velocity across the cross-section. Despite using a two-dimensional model, the shape of the pipe cross-section is a required input parameter in the model. By comparing equations 3.2 and 3.4 it becomes clear that Hagen-Poiseuille flow can be described by Darcy's law if the permeability in the pipe is described as the fictitious permeability (κ^* [m^2]) as proposed by Bersan et al. (2013):

$$\kappa^* = -\frac{2D_h{}^2}{\beta_{fi}} \tag{3.5}$$

The assumption of Hagen-Poiseuille flow regards no-slip conditions along the pipe and mass conservation between the tip of the pipe and the sand boil (Bersan et al., 2013). However, in the FEM model, water also enters the pipe from the bottom, indicating that using Hagen-Poisseuille flow is a very conservative assumption. The fictitious permeability in the pipe can be used to solve Darcy's law if Hagen-Poiseuille flow is assumed (Bersan et al., 2013).

3.1.2. Two force equilibrium (resistance)

Piping occurs when the water pressure gradient in the pipe is sufficient to bring the grains at the bottom of the pipe in motion. The critical pressure gradient or hydraulic head gradient corresponding to the stability of the grains forms the resistance term in the model. The limit state equilibrium of the grain stability is described by a two force equilibrium model (Sellmeijer, 2006), consisting of the seepage force (F_h) and the weight (F_v) of a spherical particle with diameter d ([m]).
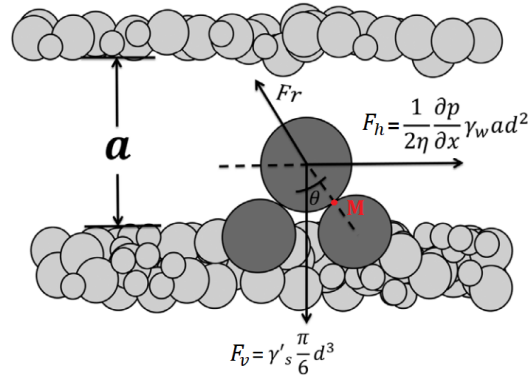
Figure 3.2: Two force equilibrium model in a erosion channel (Aguilar-López et al., 2016a)

The horizontal seepage force acts parallel to the slope of the erosion channel and is made up of the shear stress along the bottom of the channel multiplied by the equivalent area (d^2/η) (Sellmeijer, 2006). White's packing coefficient η of 0.25 describes the number of grains per unit area (White, 1940), so it takes care of the empty space between the top particles. The friction force due to the embedding of the grain between other grains (F_r) is eliminated by setting the equilibrium of moments at the contact point with the adjacent grain (point M in Figure 3.2), which reads (Wewer, 2019):

$$F_h \cos(\theta)r = F_v \sin(\theta)r \tag{3.6}$$

$$\frac{dh}{dx} = \frac{\pi}{3}\frac{\gamma_{sp}}{\gamma_w}\frac{d_{70}\eta\tan(\theta)}{a} \tag{3.7}$$

where:

$\gamma_{sp} = 16.5$ kN/m^3: volumetric weight of submerged quartz particles

$\gamma_w = 10$ kN/m^3: volumetric weight of water

d_{70} [m]: 70$^{\text{th}}$ quantile of the grain size distribution by weight

$\eta = 0.25$: White's packing coefficient (White, 1940)

$\theta = 37$ deg: grain embedment angle (Sellmeijer et al., 2011)

a [m]: the pipe height

Rewriting Equation 3.6 leads to the expression for the critical hydraulic head gradient (see Equation 3.7 (Van Esch et al., 2013)). Sellmeijer (1988) argues that larger grains are more difficult to set in motion than smaller particles. Therefore, the resistance against erosion depends on larger grain particles. For this reason, a d_{70} representative grain size diameter is substituted in the expression of the critical hydraulic head gradient. Piping progresses when the critical hydraulic gradient of Equation 3.7 is exceeded by the average hydraulic gradient inside the pipe of the FEM model.

3.1.3. Pipe geometry
The hydraulic head development across the width of the dike and the critical gradient of the two forces method are affected by the pipe geometry. The hydraulic head gradient reduces for larger pipes because less wall friction acts on the flow inside the pipe (Wewer, 2019). Consequently, the size of the pipe is limited because sufficient pressure is required inside the pipe to set the sand particles in motion (Aguilar-López et al., 2016a). The influence of cross-section shape, pipe height, and pipe length has been investigated, the and model geometry choices have been modified. So far, no general strategy for schematizing pipe geometry in a two-dimensional numerical model has been prescribed in literature.

Cross section shape
The amount of wall friction acting on the flow is determined by the shape of the pipe cross-section. Researchers, however, disagree on the width and cross-section shape of the pipe. Zhou et al. (2012) and Van Beek et al. (2015) schematize the geometry of the pipe rectangular with a constant depth and width. While Aguilar-López et al. (2016a) indicate that a circular cross-section leads to the largest pipe geometry where piping is feasible. Furthermore, the Sellmeijer model (Sellmeijer, 1988) is based on fracture flow, also called the parallel plates method.

In the fracture flow method, the pipe cross-section is infinitely wide with a very small pipe height in comparison to the width. Because this cross-section shape induces less wall friction than a rectangular or circular cross-section, the average hydraulic gradient in the pipe is lower. However, the infinite width assumption is more realistic because it includes the hydraulic head loss caused by three-dimensional meandering of the pipe in reality.

In order to compare the proposed FEM numerical model to the Sellmeijer model, the fracture flow method is used to schematize the pipe cross-section. Bersan et al. (2013) conclude that it is possible to use Darcy's law and fracture flow in COMSOL to model laminar flow through pipes. The fictitious permeability is a function of the friction loss coefficient and the hydraulic diameter (Equation 3.5), which depend on the shape of the cross-section. For fracture flow, the corresponding friction loss coefficient (β_{fi}) and hydraulic diameter (D_h) are respectively equal to $\beta_{fi} = 96.00$ and twice the pipe height (a [m]) (Aguilar-López et al., 2016a). The fictitious permeability for fracture flow (κ_f [m^2]) is now expressed as:

$$\kappa_f = \frac{2D_h{}^2}{\beta_{fi}} = \frac{2(2a)^2}{96} = \frac{a^2}{12} \tag{3.8}$$

Pipe length
Sellmeijer (1988) proposes that the pipe length is critical once the pipe has developed until almost half of the dike width (0.44L). Once the pipe grows beyond the midpoint of the dike, erosion progresses until dike failure, independent of the loading conditions. Before this can happen, the pipe must be able to develop all the way to the dike's midpoint. As a result, it is also interesting to investigate the occurrence of piping for shorter pipe lengths. The size and shape of the cross-section are assumed to be constant along the length of the pipe until it has developed along the entire width of the dike.

The pipe length affects the average hydraulic gradient in the pipe. The decrease in the hydraulic head for a short pipe is steeper than for a long pipe. A stronger decrease in the hydraulic head leads to a higher hydraulic gradient.

Pipe height
The height of the pipe remains an important research topic. Studies on pipe progression show that the pipe lengthens at the tip (primary erosion) and widens due to wall erosion in the direction of the exit point at the sand boil (secondary erosion) (see Figure 3.3) (Van Beek et al., 2015).

1. Groundwater flow
2. Pipe flow
3. Erosion at the pipe tip
4. Erosion of the pipe walls and bottom
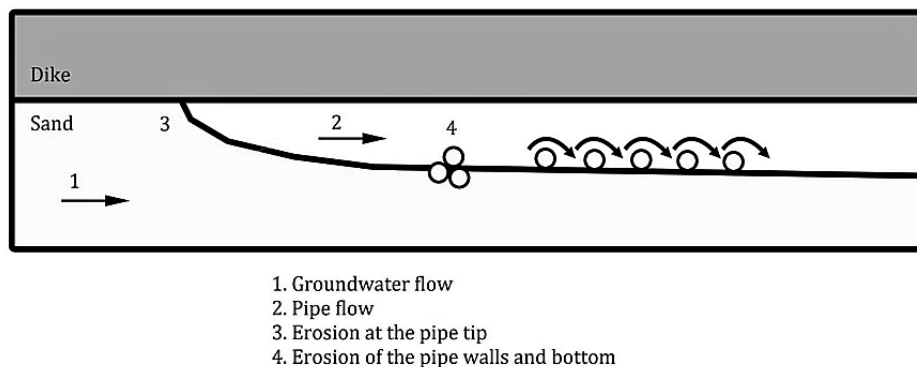
Figure 3.3: Pipe progression processes (Van Beek et al., 2015)

The equation for Hagen-Poiseuille flow (Equation 3.4) and the two force equilibrium (Equation 3.7) indicate that the hydraulic gradient depends on the height of the erosion channel. However, the actual pipe height is currently unknown, and there is no established assumption or function for including the pipe height in numerical models.

Experimental research has provided an indication of the pipe height. Van Esch et al. (2013) proposes that the pipe height for small-scale experiments varies between 0 and 3 grains, between 0 and 10 in field tests, and between 0 and 30 grains for real dikes. During the piping field experiments at the Hedwigepolder (Waterschap Hollandse Delta, 2022), a fully developed pipe has been dug out and gives an idea of the pipe height (see Figure 3.4). However, once a continuous pipe has formed, the erosion process continues in the form of the pipe widening and deepening. Therefore, the pipe height of a non-continuous pipe is likely to be smaller than depicted in Figure 3.4.

Figure 3.4: Dug out pipe at the Hedwigepolder (Förster, 2022)

The pipe height proposition of Van Esch et al. (2013) initiates the idea of assessing the occurrence of piping for multiple pipe heights. The pipe height is implemented as an iterative parameter in the model. However, an iterative process wherein the model geometry changes per (couple) iteration is computationally demanding. Especially, changes in pipe geometry lead to a large number of calculations, because the small pipe geometry must be divided into even smaller mesh faces and indices for which the FEM numerical model must solve the groundwater calculations (see Figure 3.8b).

A method has been developed to take into account the effect of varying pipe height in the model while only meshing the model once for one constant pipe height (see Section 3.2.1, for detailed explanation of mesh construction). This method is called the permeability zone method.

Erosion channel exit point
The implementation of a vertical erosion channel through a low permeable cover layer at the exit point is new in this piping erosion model compared to the Sellmeijer conceptual model (Sellmeijer, 1988). In this thesis, it is assumed that the cover layer was cracked or punctured prior.

In the field, it has been observed that the cover layer has been punctured by (fence) poles, leaving holes that can function as piping exit points. As a result, it is assumed that the vertical erosion channel is 5 to 10 cm wide, which is roughly equal to the diameter of a (fence) pole.

3.2. Implementation in COMSOL Multiphysics
To recreate the cross-sectional model for the research location, some operations in COMSOL are elaborated in this section. It is assumed that the basic principles of COMSOL are understood when trying to implement the following operations in COMSOL.

3.2.1. Mesh construction
The mesh determines the way the model is solved and therefore also the solving time and accuracy of the result. Consequently, building an adequate mesh is a crucial process in developing a FEM model.

The geometry of the model is divided into numerous mesh elements. During mesh construction, the shape, size, density, and number of elements in the geometry can be chosen to determine how the

geometry is divided. These factors have a direct impact on the problem computation, such as solving time, how much memory is required to compute a problem, and the accuracy of the solution. In this thesis, the mesh is constructed consistently in each numerical model. The exact mesh statistics for each cross-sectional model are demonstrated in Table 3.1.
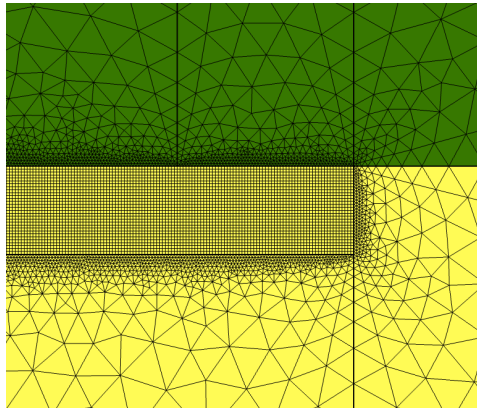
Figure 3.5: Quadrilateral mesh elements in the pipe and triangular elements cover the rest of the model geometry

The mesh in a model is made of triangular and quadrilateral (four-sided polygon) mesh elements (quads). The mesh inside the pipe is made up of quadrilateral elements, while the rest of the model is made up of triangular mesh elements (see Figure 3.5). The quadrilateral mesh elements can be as large as 1.7 mm and as small as 1.25 mm. The refinement of the quadrilateral mesh is chosen in this manner to ensure that small pipes do not go unnoticed in the model. The triangular mesh is generated automatically using a normal mesh refinement.

According to Table 3.1, the number of mesh elements in the pipe (quads) is frequently greater than the number of triangular elements dividing the rest of the model geometry. This demonstrates that the mesh in the pipe is much finer than the mesh in the rest of the model.

The solving time of the model depends on the number of mesh elements, because the physics in the model must be solved for each individual element. Therefore, it is disadvantageous to use very long model geometries, because this increases the number of mesh elements. A model geometry divided into very fine mesh elements (more elements) will, however, produce more accurate results than a coarse mesh. As a result, a balance must be found between solving time and acceptable mesh error.

Table 3.1: Mesh statistics of the numerical models of the deterministic analysis

	Well	Hout-Blerick	Buggenum	Thorn
Number of triangles	203118	220584	219670	107847
Number of quads	241638	231480	231480	112680
Number of elements	444756	452064	451150	220527
Minimum element quality	0.3896	0.4139	0.297	0.3608
Average element quality	0.9265	0.9237	0.923	0.923

The quality of the mesh is expressed in element quality, which represent how much an element has been distorted from its original shape. When a quadrilateral mesh element is a perfect square, for example, the mesh quality is 1. The shape of the mesh elements, however, is distorted to best fit the model geometry. The minimum allowed mesh quality during mesh construction is approximately 0.2, which means that if the mesh quality is less than 0.2, the mesh should be altered to better fit the model geometry.

Because the mesh is built on the shape of the geometry, it is always generated after the model geometry during a model run. Which means that model parameters that affect the model geometry also have a direct impact on the mesh. Constructing a mesh during a model run is also time consuming, so it must

be avoided that the model has to build multiple meshes in one run, a process known as remeshing. To ensure that the model only has to mesh once, variations in model parameters affecting the model must be avoided.

3.2.2. Boundary conditions

In Section 3.1 is mentioned that two types of boundary conditions are used: a 'no flow' boundary and boundary conditions that implement the foreland and hinterland water level at the boundaries of the cross-sectional models. Technically, three types of boundaries are used since the water level boundaries are split into a hydraulic head boundary and a pressure head boundary. The split is made to work more easily with the surface scale of m+NAP and still implement hydrostatic pressure boundaries. The difference between the hydraulic head and pressure head is important to understand for the application of both boundary conditions.
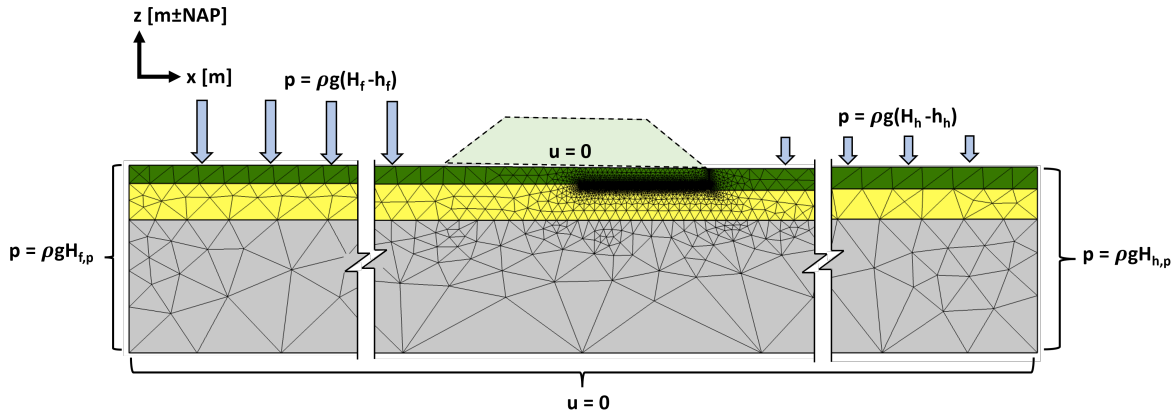
Figure 3.6: Functions of the boundary conditions

No Flow Boundary
The name implies the function of the boundary: it prevents flow across the impermeable boundary condition ($u = 0$ m/s). The no-flow boundary is applied to the boundary at the location of the dike and to the lowest boundary at the deepest point of the aquifer. The dike is assumed to be impermeable, which is acceptable for dikes made of low-permeable clay material. The no-flow boundaries are indicated as $u = 0$ m/s in Figure 3.6.

Hydraulic Head
The hydraulic head boundary condition requires a water level in the same coordinate system of the model geometry (H [m+NAP]). The boundary condition requires an input value based on a vertical coordinate. Therefore, if the model is constructed at NAP, the input value of the hydraulic head boundary condition must also be in NAP. The model determines the pressure (p) by subtracting the surface level coordinate of the foreland (h_f [m+NAP]) and hinterland (h_h [m+NAP]) of the induced foreland (H_f [m+NAP]) and hinterland (H_h [m+NAP]) hydraulic head. Figure 3.6 shows that the hydraulic head boundary is applied on the upper horizontal boundaries of the aquifer by the function:

$$p = \rho g(H_f - h_f) \qquad\qquad p = \rho g(H_h - h_h)$$

Pressure head
On the vertical boundaries of the domain, two pressure head boundary conditions were applied. The pressure head boundary requires the amount of water standing on the boundary condition expressed in height. To induce hydrostatic pressure at the vertical boundary (see Figure 3.7), the boundary condition depends on the vertical coordinate of the model domain. The pressure head boundaries for the foreland and the hinterland are defined as follows:

$$p = \rho g H_{f,p} \qquad\qquad p = \rho g H_{h,p}$$
$$H_{f,p} = H_f - z \qquad\qquad H_{h,p} = H_h - z$$

where $H_{f,p}$ and $H_{h,p}$ are the hydraulic heads in the foreland and in the hinterland dependent on the vertical coordinate (z [m+NAP]). Since the model geometry is made with respect to NAP, the vertical coordinates of the model are also in NAP.
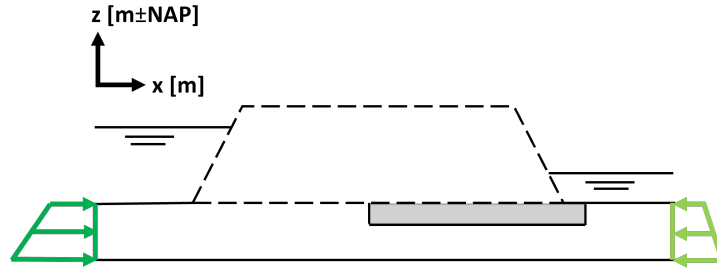
Figure 3.7: Pressure head boundary condition

3.2.3. Permeability zone method

A range of values for the pipe height (a [m]) is evaluated in this method without having to remesh the model for every value. The method is capable of including very small and very large pipe heights.

A pipe domain with the size of an exaggeratedly large pipe (a_{mesh} [m]) is included in the model geometry. Any pipe height can be assigned to the pipe domain, as long as it does not exceed the maximum pipe height to be evaluated. In the cross-sectional FEM models for the research location in Limburg, the height of the pipe domain is equal to 30 times the largest d_{70} expected to be found at the research locations, which is about 10 mm (see Section 2.3.2):

$$a_{mesh} = 30 \cdot d_{70,max} = 30 \cdot 10 \cdot 10^{-3} = 0.3m \tag{3.9}$$

Inside the pipe domain, the actual pipe with specific characteristics, such as permeability and porosity, is simulated. However, the actual pipe is simulated as an area in the pipe domain with permeability equal to the fictitious permeability of the pipe ($\kappa*$ [m^2]) rather than as a unit of geometry (see Figure 3.8a). COMSOL allows you to conditionally vary the permeability across the height of a domain. So instead of appointing the fictitious permeability (permeability of the pipe) to the entire domain, it can also be assigned to a selected height of the pipe domain. Note that the fictitious permeability must be calculated for the selected height (a [m]) within the piping domain (see Equation 3.10). The actual pipe is displayed as the grey area in Figure 3.8a and the actual pipe height is called a. The permeability of the remaining height of the pipe domain is equal to the permeability of the aquifer.

$$\kappa_f = \frac{2D_h^2}{\beta_{fi}} = \frac{2(2a)^2}{\beta_{fi}} = \frac{2(2 \cdot C \cdot a_{mesh})^2}{\beta_{fi}} \tag{3.10}$$

The conditional permeability can be implemented in the model using an if-statement saying that if the vertical model coordinate (z [m+NAP]) is bigger than or equal to the underside of the cover layer (U_C [m+NAP]) minus the pipe height (a [m]), the permeability is equal to the permeability of the pipe (κ^* [m^2], fictitious permeability). Otherwise, the permeability of the pipe domain is equal to the aquifer permeability (κ_{sand} [m^2]).

$$\text{if}(z \geq (U_C - a), \kappa^*, \kappa_{sand}) \tag{3.11}$$

By varying the permeability over a domain, the model does not have to remesh. Therefore, it is less computationally demanding to implement the applicability height of the pipe permeability (which is equal to the pipe height) within the pipe domain as the iterative parameter. Instead of changing the geometry and having to re-mesh for each pipe height value.

The height of the pipe domain is called a_{mesh}, because this is the height for which a finer mesh is built in the model. The mesh elements within the pipe domain are significantly smaller than in the remaining

(a) Schematization of permeability distribution (not to scale)

(b) Model detail with mesh
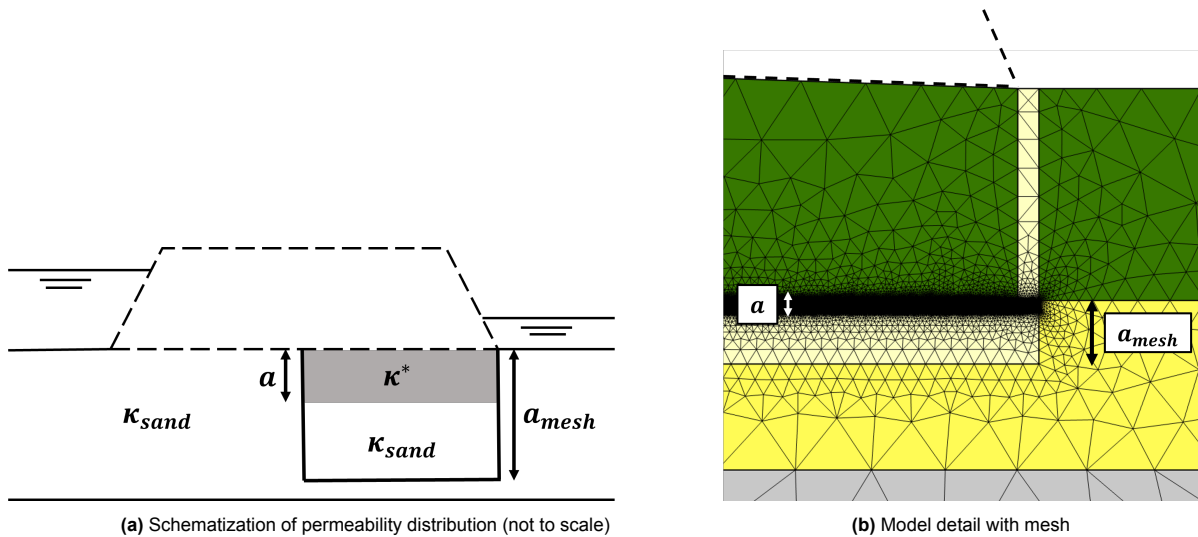
Figure 3.8: Permeability zone method

model geometry, because the mesh must be able to perceive very small pipe heights (see Figure 3.8b). Therefore, the smallest mesh elements at the top of the piping domain must be in the order of the smallest pipe heights that are desired to be evaluated.

The finest mesh elements should be in the order of magnitude of the pipe height of the smallest pipe. In the cross-sectional models of the research locations in Limburg, the smallest mesh elements are in the order of 0.001 m. The mesh elements can become coarser for bigger pipe heights. Using a very fine mesh means that more mesh elements are required to cover the domain. However, more mesh elements lead to a more computationally demanding model. Therefore, the balance must be found between having a sufficiently small mesh to include the smallest pipe and the computational demand.

3.2.4. Determination of the hydraulic head gradient
The hydraulic gradient in the pipe is the most important output value of the FEM numerical model. This is called the local hydraulic head gradient. Sellmeijer (1988) uses the global hydraulic head gradient, which is the hydraulic gradient across the width of the dike. Because the hydraulic gradient varies along the length and height of the pipe, it is decided to work with the average gradient in the pipe. This assumption is acceptable because the average hydraulic gradient is greater than the hydraulic gradient at the tip of the pipe (see Figure 3.9), implying that the hydraulic gradient that causes erosion at the tip of the pipe is slightly overestimated.

The hydraulic head is first determined along a horizontal line, that runs along the total pipe length, at half the pipe height. Subsequently, the hydraulic head gradient is calculated along the same line and the average value is determined (see Figure 3.9). To demonstrate the absolute development of the hydraulic gradient, the hydraulic gradient is shown negatively on the vertical axis in Figure 3.9. A negative development of the hydraulic gradient would have resulted from the decrease in the hydraulic head.

COMSOL offers several methods to calculate the average hydraulic gradient of models. The method described above employs the line average function across a defined horizontal line, known in COMSOL as a 2D-cutline. The average hydraulic gradient can be calculated using the line average method and the permeability zone method. When the permeability method is used, the line must be defined through the middle of the pipe and not in the aquifer domain. The vertical position of the cutline can be expressed as a function of the height of the pipe, allowing the average hydraulic gradient to be easily calculated for models with iterative pipe heights.
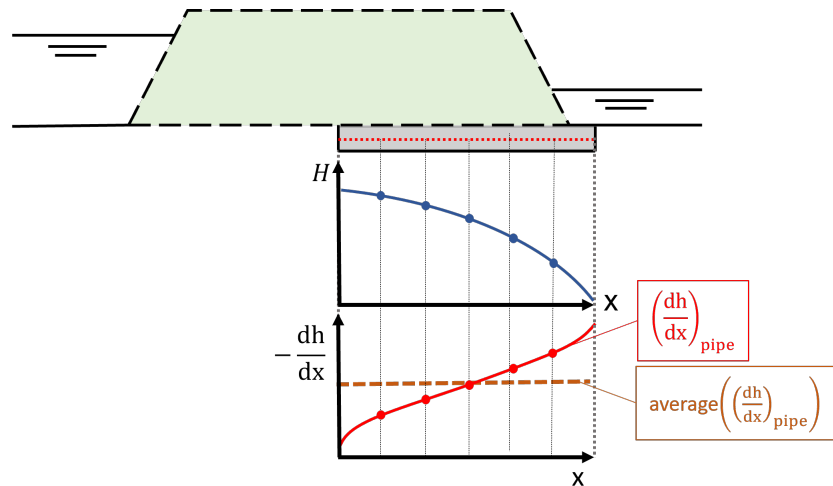
Figure 3.9: Determination of the average local hydraulic gradient in the pipe (not to scale)

3.3. Schematization of the research locations

This section describes how to schematize the dike sections near Well, Hout-Blerick, Buggenum, and Thorn into cross-sectional models. Before discussing the schematization of the cross-section per research location, the general schematization choices that are applied at each cross-section are elaborated. Finally, the calibration of cross-sectional models is discussed.

3.3.1. Schematization choices

Not all complexities can be implemented in FEM numerical models at the same time. The FEM models would become too complex and difficult to solve as a result. Therefore, making schematization choices is an essential component of creating a numerical model. Schematization choices have implications for the results and their uncertainty.

Geometry subsoil layers

Because of heterogeneity and multiple-layer systems, the subsoil structure is uncertain in reality. Including all variabilities is overly complex and may cause issues when analyzing the most influential piping variables. As a result, the individual layers are defined horizontally and with a constant thickness across the width of the cross-sectional model. This schematization choice is based on the assumptions of Sellmeijer (1988) that piping erosion only occurs at the top of the aquifer, the two-dimensional approach of the model (Sellmeijer, 1988) and the fact that horizontal flow velocities dominate piping.

In this thesis, the maximum number of layers when schematizing different subsoil layers to implement in the model is set to 5. This value is chosen to avoid overcomplicating the model as the subsoil can be divided into an infinite number of layers. It means that the subsoil is divided into a maximum of 5 layers from the surface level to the first geohydrological base. The geohydrological base is an impermeable subsoil layer that also serves as the bottom of a numerical model.

The number of layers and layer thicknesses implemented determine the model depth. Aguilar-López et al. (2016b) demonstrated that the effect of model depth on the hydraulic gradient in the pipe reaches an optimum, implying that the model depth can be chosen more efficiently than previously indicated. In Section 3.3.6 an analysis is performed to optimize the depth of the cross-sectional models.

Determining the representative grain size

To perform analytical calculations using the Sellmeijer design rule and to calculate the critical hydraulic gradient using the 2 forces method, the d_{70} (70%-quantile of the grain size distribution by weight) for the subsoil layer in which the pipe develops must be determined. The pipe is assumed to form directly at the top of the aquifer beneath the dike or the impermeable cover layer.

The required grain size can be derived from previous research or sieve curve analyses of soil samples

collected at the research locations. Several site-specific studies are examined for each research location, and the grain size is determined for several important quantiles of the grain size distribution by weight. The analysis of different soil samples and grain sizes is carried out in Appendix A.

For each research location, the average analyzed grain size is implemented in the model. For example, the d_{70} implemented in the cross-sectional model of Buggenum and the analytical Sellmeijer design rule, is the average of all the d_{70} derived from sieve curves of soil samples taken at Buggenum.

Permeability/hydraulic conductivity determination
One of the most important input parameters in cross-sectional models is the permeability or hydraulic conductivity of the subsoil layers. However, estimating this hydrogeological characteristic of a subsoil layer accurately can be hard because hydraulic conductivity in the subsoil layer is not constant throughout the layer. Each subsoil layer in the cross-sectional model is assigned a single value for hydraulic conductivity.

There are several methods for determining the hydraulic conductivity of the subsoil layers in the model. To begin, the hydraulic conductivity can be determined using the hydraulic conductivity of a similar layer from another study conducted at the research site. Pumping tests were performed in Well, Buggenum, and Thorn during the study of Koopmans & Janssen (2018) to evaluate the hydraulic conductivity of the subsoil layers.

Another way to derive the permeability or hydraulic conductivity of a subsoil layer is by using empirical formulas. In Appendix A.3, the hydraulic conductivity is derived as a function of the representative grain size for the subsoil layers using the empirical formulas of Kozeny-Carman, Den Rooijen (1992), Seelheim, and Hazen. Waterschap Limburg (2020) proposes to use the empirical formula of Den Rooijen.

Once all options for calculating permeability or hydraulic conductivity have been investigated and the results have been determined, a decision is made on the final value for permeability or hydraulic conductivity. The values are checked to ensure that they are in the same order as suggested by the pumping test results of Koopmans & Janssen (2018). Afterwards, it is carefully considered whether the average value results in a representative hydraulic conductivity of the layers. The final hydraulic conductivity is shown in the schematization in the following sections.

Porosity
The porosity describes the number of pores in a total volume (V_{tot}). The number of pores is also expressed in the volume of pores/voids (V_v) and then the porosity (ϵ_p) is expressed as:

$$\epsilon_p = \frac{V_v}{V_{tot}} \tag{3.12}$$

There is no data on the porosity of the various soil materials available for the Limburg research locations. As a result, it has been decided to work with generalized assumptions for the porosity of clay, sand, and gravel from the northern Maasvallei in Limburg:

$$\text{Porosity of clay: } \epsilon_{\text{clay}} = 0.5$$
$$\text{Porosity of sand: } \epsilon_{\text{sand}} = 0.42$$
$$\text{Porosity of gravel: } \epsilon_{\text{gravel}} = 0.375$$
$$\text{Porosity of the pipe: } \epsilon_{\text{pipe}} = 1.0$$

(An)isotropy
In isotropic soils, it is assumed that the vertical (κ_v [m^2]) and horizontal permeabilities (κ_h [m^2]) are equal. However, due to the heterogeneous properties of the soil, the isotropic assumption is not realistic. The difference between horizontal and vertical permeability is called anisotropy. The standard anisotropy factor is $\kappa_h/\kappa_v = 3$, meaning that the vertical permeability is 3 times lower than the horizontal permeability. However, an exploratory analysis of the HWBP project Noordelijke Maasvallei and Fugro revealed κ_h/κ_v values ranging from 4 to 6 for river deposits (Waterschap Limburg, 2018), while the typical anisotropy factor for coarse sand ranges from 1 to 3 (Slot & Lipzig, 2016).

Anisotropy works as a resistance against piping. A lower vertical permeability makes the flow of groundwater toward the erosion channel more difficult. An anisotropy factor of 1 is frequently used in piping assessments to assess the normative situation (Waterschap Limburg, 2018). This is the reason that the isotropic assumption corresponding to an anisotropy factor of 1 is implemented in the cross-sectional models. The effect of anisotropy is further investigated in Appendix B.

Foreland and hinterland length

Rijkswaterstaat (2021) proposes that the foreland and hinterland lengths that influence piping depend on the leakage length (λ) of the research location. The leakage length is the distance required for the hydraulic head in the aquifer to decrease by a factor of 1/e, as a result of flow through the low permeable cover layer. A short leakage length causes a rapid reduction of the hydraulic head, resulting in a higher hydraulic head gradient and thus increased piping risk. A thinner or more permeable cover layer results in a shorter leakage length (Rosenbrand & Knoeff, 2020).

The leakage length can be calculated with Equation 3.13 and depends on the thickness and hydraulic conductivity of the aquifer (D_a [m], K_a [m/d]) and the cover layer (D_c [m], K_c [m/d]). It reads (Rijkswaterstaat, 2021):

$$\lambda = \sqrt{\frac{K_a D_a D_{\text{clay}}}{K_{\text{clay}}}} \tag{3.13}$$

For the research locations, the leakage length is determined with the average hydraulic conductivity of the aquiferous layers (K_a). This includes all subsoil layers except for the clay layer. The thickness is the sum of the thicknesses of the aquiferous layers. The leakage length is calculated for each research location (see Table 3.2).

	K_{clay} [m/d]	D_{clay} [m]	K_a [m/d]	D_a [m]	λ [m]	3λ [m]
Well	0.6	1.5	109	14	61.62	184.87
Hout-Blerick	0.46	2	53	14	57	171.03
Buggenum	0.29	1.0	141	18.5	94.9	283.15
Thorn	0.49	1.5	79	16	62.34	187.02

Table 3.2: Leakage length per research location

According to Rijkswaterstaat (2021), the foreland length in a piping assessment should be equal to the leakage length or the distance from the dike to the river (L_1). The length of the foreland is equal to the leakage length when $L_1/\lambda > 2$. This means that the model contains the shortest of the two lengths. Because the Maas is quite far from the dike section at Well, Hout-Blerick, and Thorn, the leakage length is implemented as the foreland length in the cross-sectional models. The cooling channel besides the dike section near Buggenum functions as the water source in the piping assessment. As a result, it is decided to include a short foreland length of 3 m in the Buggenum cross-sectional model. The hinterland length of the cross-sectional models equals 3 times the leakage length of the research locations (see last column of Table 3.2) (Rijkswaterstaat, 2021).

General material properties

To be able to solve Darcy's Law (Equation 3.2), the 2 forces equilibrium (Equation 3.7) and the Sellmeijer design rule, several general material properties are required. Table 3.3 demonstrates the general properties of soil and water that are implemented in the numerical models.

Table 3.3: General soil and water properties (Rijkswaterstaat, 2021)

Description		Unit	Value
Specific weight sand	γ_s	[kN/m^3]	26.5
Specific weight water	γ_w	[kN/m^3]	10
Density of water	ρ_w	[kg/m^3]	1000
Kinematic viscosity water	v	[m^2/s]	$1.33\cdot10^{-6}$
Dynamic viscosity water	μ	[kg/m·s]	0.00133

The value for the kinematic and dynamic viscosity of water corresponds to a water temperature of 10 degrees. This is assumed to be the average temperature of groundwater. Calculations often use the submerged weight of sand particles, which equals:

$$\gamma_{sp} = \gamma_s - \gamma_w = 26.5 - 10 = 16.5 \text{kN/m}^3$$

3.3.2. 60.070 Well

The research location near Well is located along dike ring 60, near dike pole 60.070. This is the most northerly research location and lies on the right bank of the Maas. The evaluated dike section is located just outside the village of Well (see Figure 3.10) and is part of the primary flood defence system. Well is surrounded by several water bodies: Maas, Leukermeer, Strandbad Seurenheide, and Reindersmeer. The dike section itself is also surrounded by small drainage ditches and waterway the Papenbeekse Broeklossing. Each of these water bodies influences the hydrogeological circumstances near the dike section.

Figure 3.10: Location Well cross-section, dike pole 60.070 (Google, 2022)

Surface level and dike profile

Figure 3.11 shows the dike profile at the research location near Well. The elevation profile can be analyzed with elevation data from AHN (2022) and the standpipe register (see Appendix C). AHN (2022) being the general digital elevation map of the Netherlands. The elevation data in the standpipe register is measured at the exact location of the dike section, whereas the location in AHN (2022) is estimated. As a result, if the elevation data from the sources differs, the elevation data in the numerical model is derived from the standpipe characteristics.

The elevation of the inner and outer toe of the dike lie respectively at approximately 12.68 and 12.10 m+NAP, while the average elevation of the hinterland is 12.37 m+NAP and the foreland is 12.35 m+NAP and decreasing towards the river, according to AHN (2022). The standpipe register states a foreland

level height of approximately 13 m+NAP and a hinterland level of 12.8 m+NAP. The width of the dike can also be derived from the elevation profile and is approximately equal to 24 m.
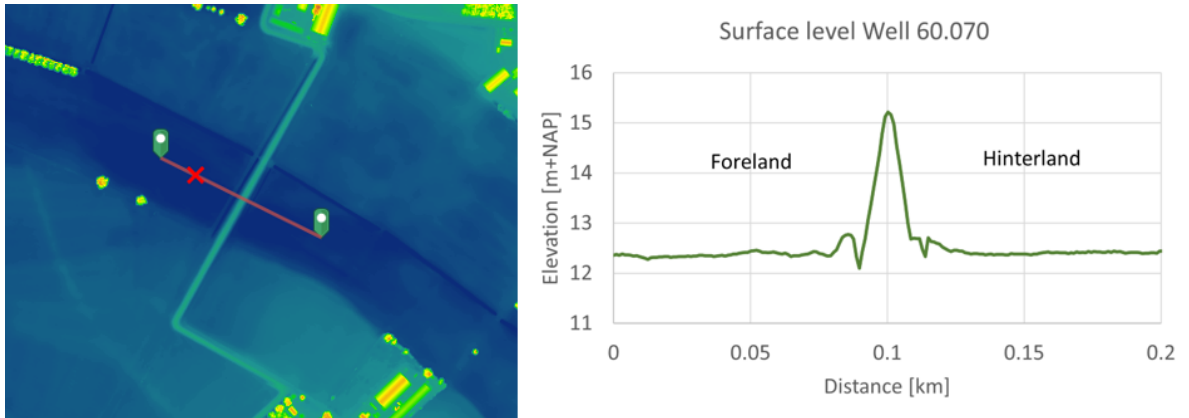
Figure 3.11: Location and surface level elevation of dike section near Well (AHN, 2022)

Subsoil and hydrogeological characteristics

Table 3.4 displays the subsoil layers and corresponding characteristics that make up the cross-sectional model of Well. The schematization of the subsoil layers is based on cone penetration tests (CPTs) near Well, manually drilled samples and the subsoil model from DINOloket (2022), which is an open source database of Dutch subsoil data. All evidence from the soil and the elaborated version of the soil schematization are included in Appendix A.

Below the gravel layer, shown in Table 3.4, a subsoil layer of the Kiezeloöliet and Breda formation is present. These layers serve as a geohydrological base and are thus excluded from the model. Another reason is the choice of maximum model depth. The determination of the hydraulic conductivity and d_{70} of the subsoil layers is discussed in Appendix A.3.

Table 3.4: Model subsoil configuration Well

Description/ material	Underside layer [m+NAP]	D [m]	K [m/d]	d_{70} [mm]
Surface level	13 / 12.8			
Clay	11.5	1.5 / 1.3	0.6	-
Sand	8.5	3	48	0.66
Gravel	-2.5	11	125	-

The cross-section geometry of Well's numerical model is shown in Figure 3.12. Because the model geometry is too long to display in full, this figure also includes the values for foreland and hinterland length. Appendix D discusses other model parameters that define the geometry.
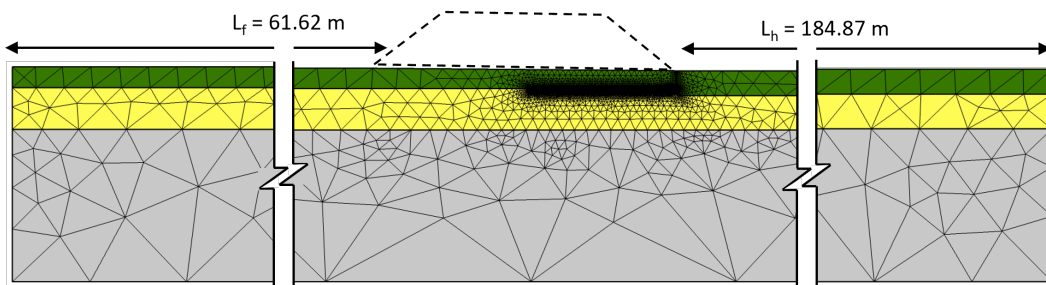
Figure 3.12: Cross-section geometry of the numerical model of Well

3.3.3. 70.075 Hout-Blerick

The second research location is the dike section in dike ring 70 at dike pole 70.075, near Hout-Blerick. The dike section is located on the left bank of the Maas and is part of the primary flood defence system of Hout-Blerick, which is a city district of Venlo. The hydrogeological characteristics of the dike section at 70.075 are influenced by the presence of a stream (Springbeek) and a fishpond (Tangkoel) for which the water level is regulated by a pumping station, just behind the dike.
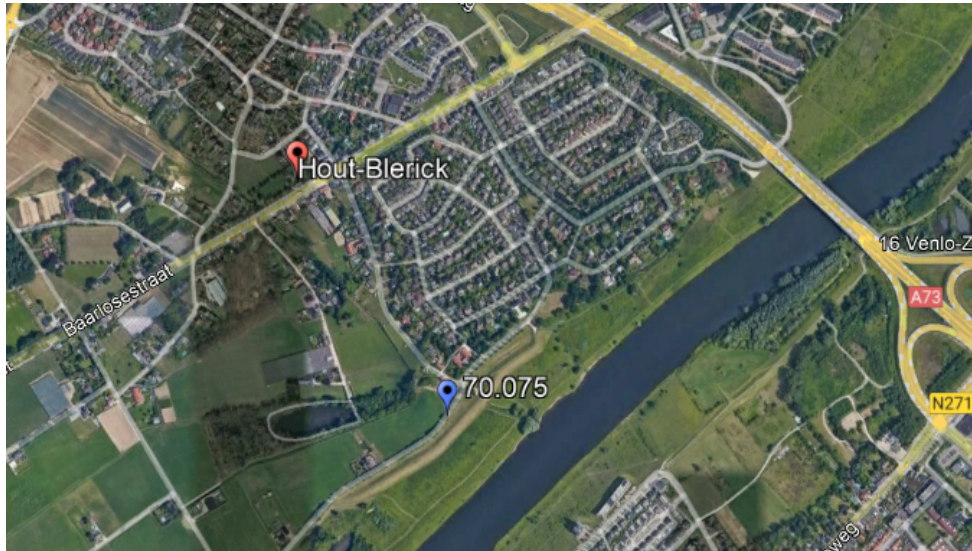
Figure 3.13: Location Hout-Blerick cross-section, dike pole 70.075 (Google, 2022)

Surface level and dike profile

For the research location near Hout-Blerick an elevation profile of the dike has been derived from AHN (see Figure 3.14). From the elevation profile can be found that the dike crest lies at 19 m+NAP and the dike width is approximately 29 m. The surface level at the hinterland and foreland lie respectively at about 16 m+NAP and 14 m+NAP. The hinterland surface level that is applied in the model is corrected to 14.50 m, according to the standpipe information in Appendix C.

A second peak in the foreland is visible in the elevation profile in Figure 3.14. This is most likely the result of a tree standing in the foreland and is not considered further in the process.
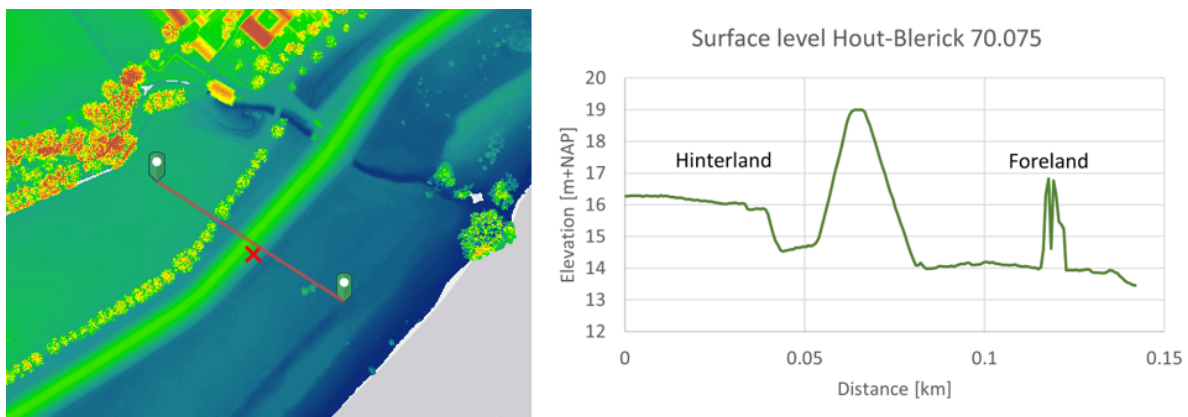
Figure 3.14: Location and surface level elevation of dike section near Hout-Blerick (AHN, 2022)

Subsoil and hydrogeological characteristics

There are fewer studies and data available for Hout-Blerick than for the other research locations. Except for the monitoring project of the standpipe data in Appendix C, the dike near Hout-Blerick has not been involved in any recent studies.

The grain size data for the research location comes from the project 'Monitoring grondwaterstanden langs de Maas' (Van Heerebeek, 2013) (see Appendix A). The Hout-Blerick subsoil schematization is based on the interpretation of several cone-penetration tests (CPT), as shown in Appendix A in Figure A.5. To validate the interpretation, the CPT tests were compared to DINOloket (2022) deep subsoil models. Empirical formulas are used to determine the hydraulic conductivity of the sand layer beneath the clay layer (see Appendix A.3). The hydraulic conductivity of the clay and deepest sand layer is extracted from the project (Koopmans & Janssen, 2018). Table 3.5 shows the subsoil configuration implemented in the Hout-Blerick cross-sectional model and Figure 3.15 demonstrates the corresponding model geometry.

Table 3.5: Model subsoil configuration Hout-Blerick

Description/ material	Underside layer [m+NAP]	D [m]	K [m/d]	d_{70} [mm]
Surface level	14 / 14.5			
Clay	12	2 / 2.5	0.46	-
Sand 1	6.5	5.5	20	0.5
Sand 2	-2	8.5	75	-
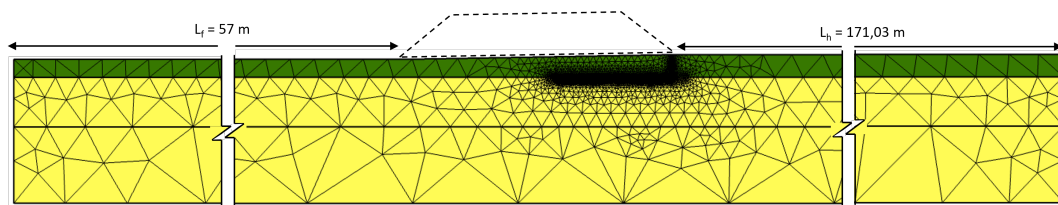
Figure 3.15: Cross-section geometry of the numerical model of Hout-Blerick

3.3.4. 75.030 Buggenum

The third research location is situated near Buggenum, which is a small village on the left bank of the Maas. The research location in Buggenum is situated near dike pole 75.030 because at this location a monitoring network is present to measure the hydraulic head in the dike. The data from the monitoring network are later used to calibrate the cross-sectional model of the dike (see Section 3.4).
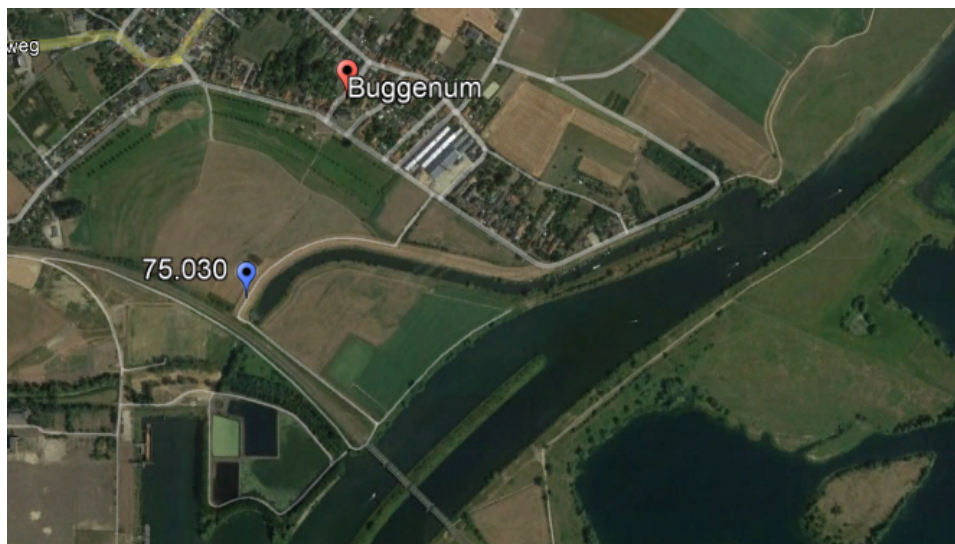
Figure 3.16: Location Buggenum cross-section, dike pole 75.030 (Google, 2022)

The dike is built along a cooling channel from a former power plant. Normally, this channel has a draining function for the groundwater level of the hinterland. A nearby port and the cooling channel

influence both the hydrogeological conditions of the dike section near Buggenum. The foreland length of the cross-sectional model of Buggenum is restricted by the cooling channel because the cooling channel functions as the nearest water body.

Surface level and dike profile
Figure 3.17 depicts the profile and elevations of the dike in the research area of Buggenum. From the dike profile, can be seen that the crest level is at 20.60 m+NAP and the width of the dike is approximately equal to 29 m. However, in the near future, the crest level of the dike is to be increased to 22.10 m+NAP.
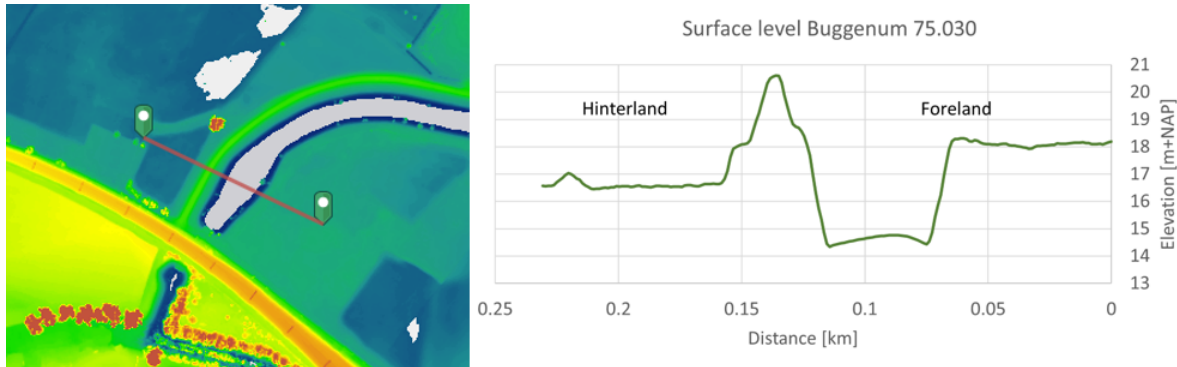
Figure 3.17: Location and surface level elevation of dike section near Buggenum (AHN, 2022)

The outer toe of the dike is located at an elevation of 14.34 m+NAP. From Figure 3.17 can easily be assumed that the inner slope of the dike contains a berm. However, this is an incorrect assumption, because the berm is actually an excavation of the original surface level. As a result, the inner toe of the dike is located at an elevation of 18.12 m+NAP, rather than at 16.63 m+NAP which is the lowest level of the excavation.

Subsoil and hydrogeological characteristics
Buggenum contains fine and coarse subsoil layers. For the gravel layers, the permeability is derived from pumping tests which give a hydraulic conductivity of 110-184 m/day (Slot & Lipzig, 2016). The permeability of the sand layer is derived using the empirical formula of Den Rooijen Equation A.3 (see Appendix A.3). Waterschap Limburg uses this empirical formula to calculate the hydraulic conductivity for soil layers without available data (Waterschap Limburg, 2020). The full determination of the hydraulic conductivity and d_{70} is discussed in Appendix A.

The configuration of the cross-section geometry of the numerical model of Buggenum is shown in Table 3.6 and Figure 3.18. Due to the length of the geometry of the cross-sectional model, it could not be displayed in full.

Table 3.6: Model subsoil configuration Buggenum

Description/ material	Underside layer [m+NAP]	D [m]	K [m/d]	d_{70} [mm]
Surface level	18 / 17			
Clay	16	2 / 1.0	0.29	-
Sand	15.2	0.8	37	0.9
Gravel 1	7	8.2	184	-
Gravel 2	-2.5	9.5	110	-

$L_f = 3$ m $L_h = 283.15$ m
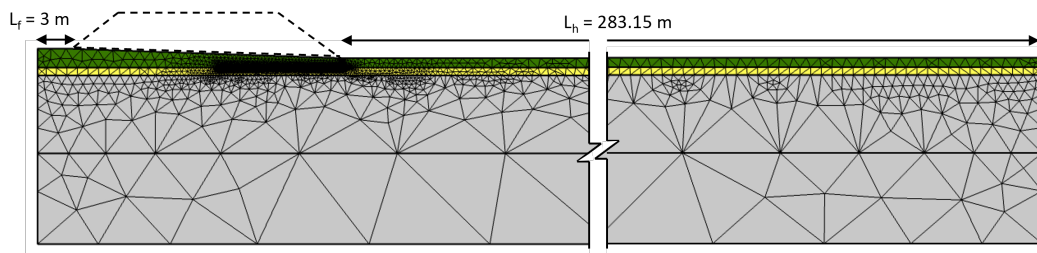
Figure 3.18: Cross-section geometry of the numerical model of Buggenum

3.3.5. Thorn

The most southerly located research location is near the town of Thorn, which is located on the lower terrace of the Maas near the Belgian border. Thorn is connected to the Maas through the lake 'De Grote Hegge' (see Figure 3.19). The model of Thorn is based on a cross-section of the dike from dike ring 79. At 79.037+12, a network of monitoring wells is situated to monitor the hydraulic head over the dike. In addition to that, extensive groundwater and subsoil surveys were conducted at this location as part of the project 'POV Piping - Invloed Maasklei en Grindlagen (Koopmans & Janssen, 2018).
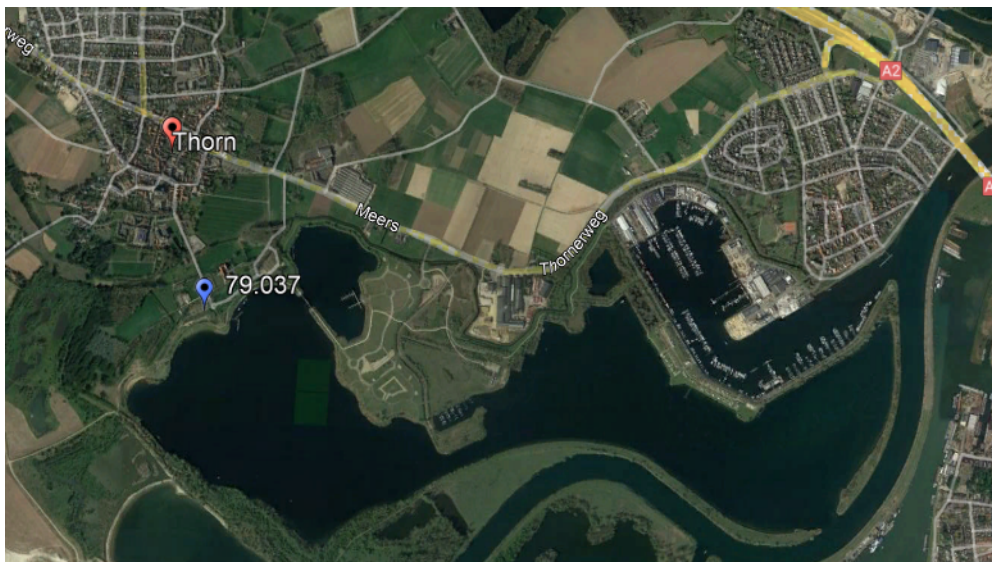
Figure 3.19: Location Thorn cross-section, dike pole 79.037

Surface level and dike profile

Besides being the most southerly, Thorn is also the most elevated research location. The dike profile of this research location is retrieved with data from AHN (2022). In Figure 3.20 the crest level of the dike lies at 24.91 m + NAP, while the inner and outer toe level lies respectively, at 22.94 m+NAP and 23.7 m+NAP. The crest level of the dike is to be heightened by 0.5 m shortly, which sets the crest level height at 25.4 m+NAP. The elevation of the foreland decreases towards the lake 'De Grote Hegge', while the elevation of the hinterland slowly increases. From the dike elevation profile data is derived that the width of the dike is approximately 14 m.

Subsoil and hydrological characteristics

The drilling profiles and DINOloket (2022) subsoil model included in Appendix A, provide the geological data to schematize the subsoil structure of the cross-sectional model. The soil layers are extremely simplified in the cross-sectional model, but aim to represent an overall average layer structure.

The upper subsoil of Thorn consists of three layers, a clay cover layer, a coarse sand layer and underneath a thick gravel layer. The pumping test (Slot, 2016) has provided the hydraulic conductivity of the
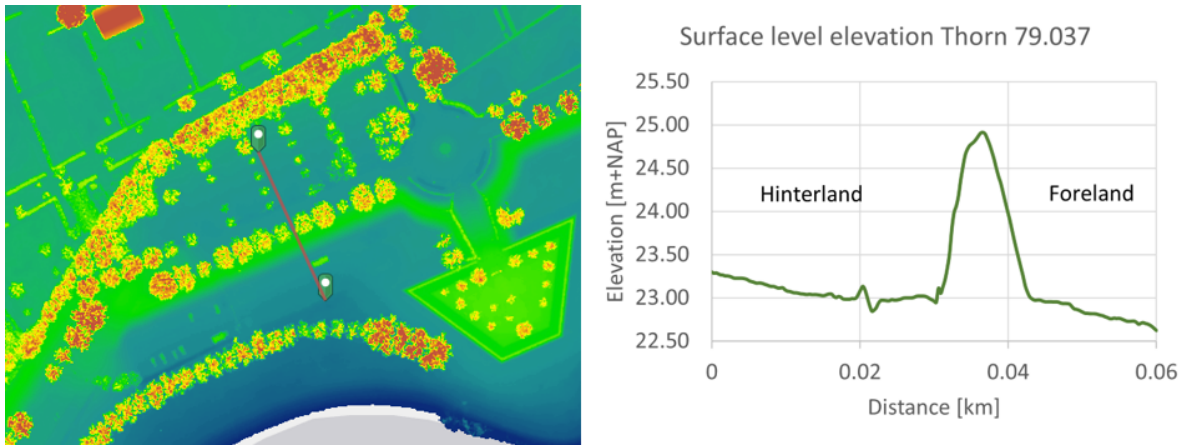
Figure 3.20: Location and surface level elevation of dike section near Thorn (AHN, 2022)

layers near Thorn. The hydraulic conductivity of the gravel layer is mainly determined by the amount of sand in the pores between the gravel particles (Koopmans & Janssen, 2018).

Table 3.7: Model subsoil configuration Thorn

Description/ material	Underside layer [m + NAP]	D [m]	K [m/d]	d_{70} [mm]
Surface level	22.94 / 23.7			
Clay	22.2	0.72 / 1.5	0.49	-
Sand	20.4	1.8	30	0.46
Gravel	6.1	14.3	85	-

Figure 3.21 shows the cross-section geometry of the numerical model of Thorn. This figure also includes the values of foreland and hinterland length, since the model geometry is too long to display in full. Other model parameters that define the geometry are discussed in Appendix D.
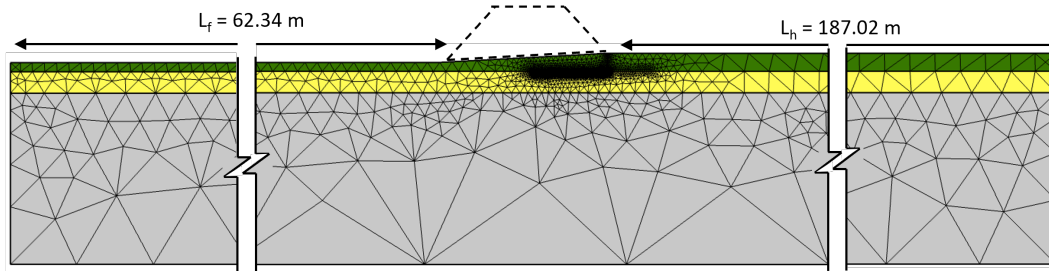
Figure 3.21: Cross-section geometry of the numerical model of Thorn

3.3.6. Optimization of the model depth

In the previous subsections, the research locations were schematised into a multiple subsoil layer system. It might not be necessary to include a large aquifer depth in the cross-sectional models for the piping assessment, since a smaller model geometry makes the model more efficient. Aguilar-López et al. (2016b) proposed that the hydraulic head gradient in the pipe is influenced by a limited aquifer thickness. This means that the change in hydraulic head gradient becomes smaller until it is negligible for a certain aquifer thickness. The effect of aquifer depth on the hydraulic gradient in the pipe is investigated to determine whether this assumption can be applied in cross-sectional piping models.

The total thickness of the aquifer (D_a) consists of the sum of the cover layer, the sand layer and any underlying layers. In this analysis, the aquifer thickness is varied by changing the thickness of the

deepest subsoil layer in the model (D_i). Tables 3.8, 3.9, 3.10 and 3.11 demonstrate the change in the hydraulic gradient with increasing depth of the aquifer.

Table 3.8: Well: Aquifer depth influence on gradient

D_{grav} [m]	D_{a} [m]	dh/dx [m/m]
0.5	5	0.000633
3.5	8	0.000958
5.5	10	0.00105
11	15.5	0.00114

Table 3.9: Hout-Blerick: Aquifer depth influence on gradient

$D_{\mathrm{sand,2}}$ [m]	D_{a} [m]	dh/dx [m/m]
0.1	7.6	0.0022
0.5	8	0.0023
2.5	10	0.0028
8.5	16	0.0039

Reducing depth of the Buggenum model to the proposed aquifer depth influences three subsoil layers, because the schematization of Buggenum is very deep. Therefore, the three corresponding layers are included in the aquifer depth analysis.

Table 3.10: Buggenum: Aquifer depth influence on gradient

$D_{\mathrm{grav,1}}$ [m]	$D_{\mathrm{grav,2}}$ [m]	D_{riv} [m]	D_{a} [m]	dh/dx [m/m]
6.2	0	0	8	0.0058
8.2	0	0	10	0.0065
8.2	5	0	15	0.0074
8.2	9.5	0	19.5	0.0083
8.2	9.5	18	37.5	0.0099

Table 3.11: Thorn: Aquifer depth influence on gradient

D_{grav} [m]	D_{a} [m]	dh/dx [m/m]
1.7	5	0.0013
4.7	8	0.0017
6.7	10	0.0019
11.7	15	0.0023
14.3	17.6	0.0024

From this analysis can be concluded for the research locations Well, Thorn, and Hout-Blerick, that the change in hydraulic head reaches an optimum for a total aquifer depth of approximately 8 to 10 m. This optimization is not directly visible from Table 3.10, but for the last depth variation, the total depth of the aquifer is nearly doubled compared to the previous variation, and the hydraulic gradient does not change significantly. Subsequently, the model depth is limited to the order of 10 to 20 m.

3.4. Model calibration

Model calibration is a process used in model development to establish an adequate representation of the reality in the model. Calibration is accomplished by comparing the hydraulic head development over the dike as determined by the FEM numerical models to field measurement data from standpipes at the research locations. Before performing the actual calibration, the data from the standpipes and pore pressure gauges are analyzed, and a sensitivity analysis is performed in Appendix B, to understand the impact of the model parameters. Finally, a discussion of the calibration results is presented to interpret the results.

3.4.1. Field measurement data analysis

The Waterschap of Limburg has provided hydraulic head data of standpipes and pore pressure gauges present at the research locations for the period 01-07-2021 until 01-08-2022, which includes the flood event in Limburg from around 13-07-2021 until 23-07-2021. Appendix C contains standpipes and pore pressure gauges characteristics, such as location in the dike and measurement depth. Graphs depicting the development of the hydraulic head in July 2021 for multiple standpipes (PB-#) and pore pressure gauges (WSP-#) at each research location are also included in Appendix C (see Figures C.9,

C.10, C.11 and C.12). The depth and location of the standpipes and pore pressure gauges in the cross-sectional models are shown in Figures C.5, C.6 and C.7.

For uplift, heave and piping to occur, groundwater must flow in the direction from the foreland and floodplains, towards the inner toe and hinterland of the dike. However, because the surface level of the hinterland is higher than the surface level of the foreland and the Maas has a draining character in terms of groundwater flow, seepage flow at the research locations is in the direction of the Maas under normal conditions. For piping to occur the water levels of the flood event must be sufficiently high to reverse the direction of the groundwater flow.

Well, Hout-Blerick and Buggenum
While keeping in mind that groundwater flows from a high hydraulic head to a lower hydraulic head and the position of the standpipes and pore pressure gauges on the dike as proposed in Appendix C, the direction of seepage flow can be derived from Figures C.9, C.10, C.11 and C.12. During the flood event, the standpipe and pore pressure gauges on the outside of the dike (in the outer toe and foreland) measure a higher hydraulic head than the standpipe and pore pressure gauges more inwards (crest, inner toe, and hinterland) at the research locations Well, Hout-Blerick, and Buggenum. This indicates that the seepage flow at these research locations has the proper flow direction to initiate the piping failure mechanism.

Thorn
According to Figure C.12 in Appendix C, under the extreme conditions of the flood event, the seepage flow direction remains dominant toward the outside of the dike and the Maas. The pore pressure gauge in the hinterland (WSP-18) measures a greater hydraulic head than the pore pressure gauge in the outer toe (WSP-21), implying that seepage flows in the direction of the outer toe. The data of the standpipes and pressure gauges at Thorn cannot be used to calibrate a cross-sectional model that is made to assess piping. Subsequently, unlike the other cross-sectional models, the Thorn cross-sectional model is not calibrated because the data series show that the piping is not a dominant failure mechanism at the dike cross-section near Thorn.

3.4.2. Method
The cross-sectional models of Well, Hout-Blerick, and Buggenum are calibrated using hydraulic head field measurement data. A new model configuration is created specifically for calibration of each research location. Because no piping signs were observed during the data measurement period, the new model configurations used in the calibration do not include a pipe. The foreland and hinterland length of the model is determined by the standpipe and pore pressure gauge located the most in the foreland or hinterland. The reason for this decision is that at the location of the standpipes and pore pressure gauges the hydraulic head is known from the field measurement data. At the corresponding location, this data is implemented as boundary conditions (see Figures C.5, C.6 and C.7).

To quantify the calibration, for each cross-section, one or two standpipes or pore pressure gauges are used that are located under the crest of the dike and measuring the hydraulic head in the aquifer beneath the dike. These standpipes and gauges are located between the two standpipes or gauges used for boundary conditions.

The hydraulic head from the FEM numerical models at the location of the standpipes in the dike, is compared to the measurement data corresponding to that standpipe to calibrate the models. Because the hydraulic head data is measured over time, time-dependent studies are used in the models to simulate the hydraulic head. The parameters (hydraulic conductivity, layer thickness and anisotropy) are then fine-tuned for each cross-sectional model until the difference between the hydraulic head determined by the models and the measured hydraulic head (calibration error) is sufficiently small. The calibration error target is set to a maximum of 10% of the measurement range. Note that this target is a rule-of-thumb criterion. This calibration criterion is set with the help of a senior (geo)hydrologist from Arcadis with expert knowledge of the Limburg subsoil.

3.4.3. Calibration results
The calibration results for Well, Hout-Blerick and Buggenum are shown in Figures 3.22, 3.23 and 3.24. The asterisks in the figures represent data points from the standpipes' and pore pressure gauges' field

measurement data. Simultaneously, the solid lines represent the evolution of the hydraulic head over time as simulated by the cross-sectional FEM models. The field measurement data and associated hydraulic head lines are displayed in the same colours. An additional standpipe is available for Hout-Blerick and Buggenum model calibration, whereas the cross-sectional model of Well is calibrated for only one pore pressure gauge. That is why Well only has one set of data points and one line comparison, whereas Hout-Blerick and Buggenum have two.
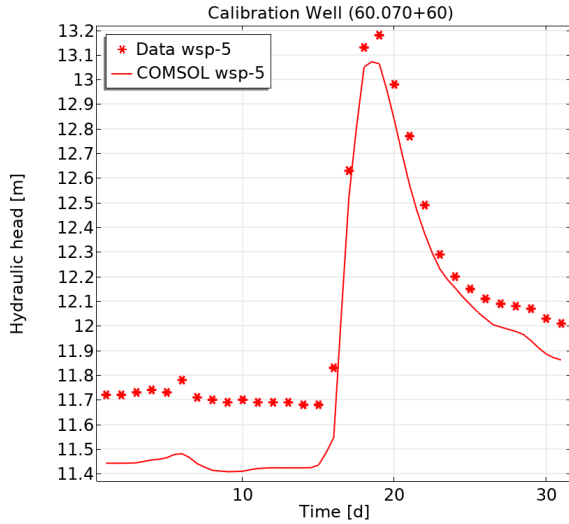
Figure 3.22: Calibration results Well
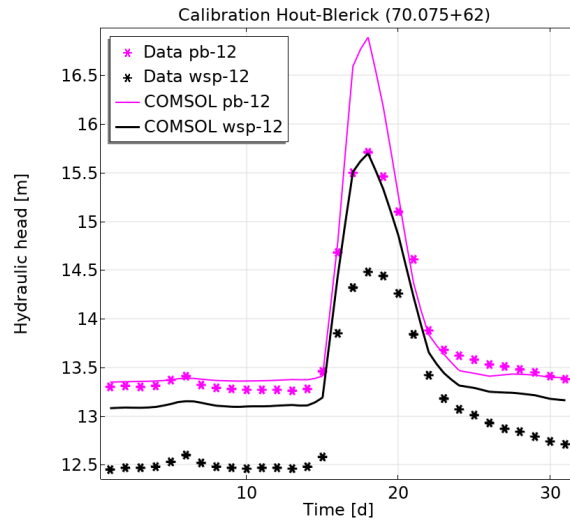
Figure 3.23: Calibration results Hout-Blerick
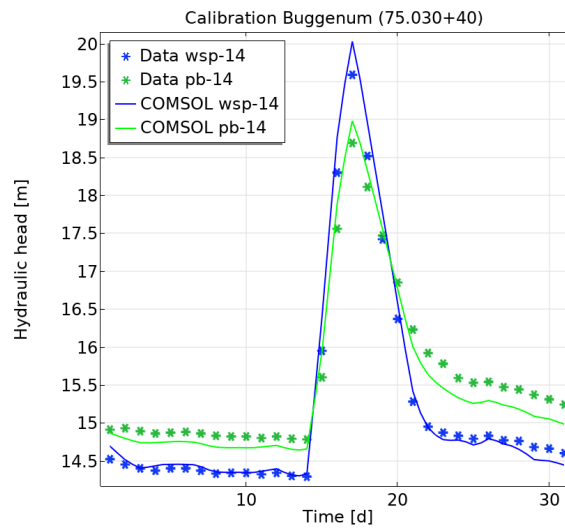
Figure 3.24: Calibration results Buggenum

Figure 3.22 displays the calibration results for the cross-sectional model of Well. The model is calibrated to data of pore pressure gauge WSP-5. The hydraulic head development simulated by the FEM model shows similarities to the field measurement data of the pore pressure gauge. However, some offset is visible, particularly in the time series before (t < 16 d) and after the flood event has passed. At the most extreme conditions of the flood event (peak t = 19 d), the model offset is at a minimum, which is 0.12 m. The calibration error target is met at this time step because the range of observations is 1.5 m, so the maximum calibration error is 0.15 m. Before the flood event (t < 16 d) the model estimates an undershoot of approximately 0.25 m. After the flood event, the simulated hydraulic head development shows an increasing undershoot as time progresses.

The calibration of the cross-sectional model of Hout-Blerick is performed for a standpipe (PB-12) and a pore pressure gauge (WSP-12) which are both located in the aquifer beneath the crest (see Figure 3.23).

Note that the asterisks and lines with identical colours belong together. The figure demonstrates that the Hout-Blerick calibration is quite poor for extreme conditions (16 d < t < 20 d) and in general for WSP-12. However, the hydraulic head determined by the FEM model at the location of PB-12 shows a similar trend under normal conditions, at the beginning and end of the flood event (t < 15 d and t > 19 d) as the measurements of standpipe PB-12. The calibration error for the estimated hydraulic head at PB-12 is approximately 0.1 m under normal conditions, but the error is about 1.2 m under extreme conditions for PB-12. Under normal conditions, the error for PB-12 meets the target criteria, but for extreme conditions, the error exceeds the target criteria and is too big. The hydraulic head estimated with the FEM model at location WSP-12 shows a vertical offset under normal and extreme conditions, which exceeds the target calibration error. It is coincidental that the PB-12 data points and the hydraulic head derived by COMSOL for WSP-12 match under extreme conditions.

The cross-sectional model of Buggenum has the most successful model calibration (see Figure 3.24). The calibration error for both the WSP-14 pore pressure gauge and the PB-14 standpipe is within the limits of the calibration error criterion. The maximum error set by the error criterion for standpipe PB-14 is 0.39 m. The maximum calibration error for standpipe PB-14 is 0.29 m under extreme conditions (t = 17 d) and 0.26 m under normal conditions (t < 14 d and t > 22 d). The maximum estimated calibration error under extreme conditions (t = 17 d) for WSP-14 is equal to 0.43 m and 0.16 m under normal conditions (t < 14 d and t > 22 d). Both estimated calibration errors for WSP-14 are in line with the maximum calibration error set by the criterion, which is 0.53 m.

3.4.4. Discussion
The calibration of the cross-sectional models did not go exactly as planned. There were several set-backs and issues, and due to time constraints, it was not possible to improve the calibration of the cross-sectional models. The calibration difficulties, possible explanations for calibration errors and consequences for the results of the FEM model are discussed further below.

Fine-tuning of the model parameters
The objective of the calibration was to fine-tune the hydraulic conductivity and layer thickness (of the clay, sand and gravel layers) and anisotropy of the aquifer, in order to make the cross-sectional model as realistic as possible and thus simulate the hydraulic head evolution in the dike geometry as accurately as possible.

Appendix B analyzes the sensitivity of the FEM model for the hydraulic conductivity and layer thickness, anisotropy of the aquifer and foreland and hinterland length. However, the variability of the subsoil characteristics (hydraulic conductivity, layer thickness and anisotropy) affects the magnitude of the hydraulic gradient only in the order of centimetres, which is not sufficient to influence the calibration results of the FEM models. Therefore, these model parameters could not be fine-tuned according to this calibration method. Consequently, the models corresponding to the calibration results and the piping assessment in the next chapters consist of the subsoil characteristics as derived in Section 3.3.

Calibration errors
Calibration results for the Well and Hout-Blerick cross-sectional models show errors that exceed the criterion maximum error, whereas the calibration of the Buggenum cross-sectional model results in small calibration errors. Several factors, which are discussed further below, may have contributed to these findings.

Well
The locations of the standpipes and pore pressure gauges for research location Well are shown in Figure C.1 in Appendix C. Because the WSP-06 pore pressure gauge is located in a ditch behind the dike, it was advised not to use its field measurement data as input for the boundary condition. The WSP-7 pore pressure gauge provides a more accurate representation of the hydraulic head in the hinterland and is thus used as an input for the hinterland boundary condition during calibration. For the foreland boundary condition, the WSP-4 pore pressure gauge field measurement data are used.

The calibration result in Figure 3.22 demonstrates that the hydraulic head measured by pore pressure gauge WSP-5 is greater than that simulated by the model. The presence of several water bodies (Strandbad Seurenheide, Het Leuken, and the Maas) that induce three-dimensional groundwater flow

could explain this difference. The greater hydraulic head measured by WSP-5 could be due to the three-dimensional groundwater flow beneath the dike. Another reason could be that the presence of ditches with draining or saturating functions influences the hydraulic head in the hinterland.

The fact that the FEM model underestimates the hydraulic head under normal conditions but estimates a similar hydraulic head under extreme conditions indicates that the model is overly permeable. Under normal conditions, it appears that too few fluxes enter the model, but it is also possible that groundwater flows through other subsoil layers that are not connected to the WSP-5 pore pressure gauge.

Because the calibration of the Well cross-sectional model is performed for a single pore pressure gauge, it is difficult to determine the head development across the dike width, and thus the hydraulic gradient. The hydraulic head at WSP-5 is underestimated by the FEM model, whereas the boundary condition is based on true hydraulic head measurements in the foreland. This implies that the FEM model overestimates the decrease in hydraulic head across the dike width, as well as the hydraulic gradient driving piping. It implies that the piping assessment performed using the cross-sectional model of Well is somewhat conservative.

Hout-Blerick
The cross-sectional model of Hout-Blerick is calibrated for standpipe PB-12 and pore pressure gauge WSP-12. PB-12 is located at the crest of the dike, while WSP-12 is located 28 m further in the inner toe of the dike. The model overshoot under extreme conditions for both locations (see Figure 3.23) demonstrates that the model contains insufficient resistance against the water level variation induced by the boundary conditions. This could be due to an overly permeable aquifer or clay layer, or a foreland that is too short. A longer foreland, on the other hand, would result in more fluxes entering the model, potentially increasing the hydraulic head derived by the model.

The vertical translation of the standpipe PB-12 field measurement data and the pore pressure gauge WSP-12 suggests that some drainage or water level regulation occurs between the two measurement locations. This effect could be caused by a nearby pumping station that regulates Springbeek's water level (see Figure C.2 in Appendix C). Because the model is two-dimensional, it cannot account for groundwater flow towards the pumping station, which could explain the vertical difference between the field measurement data and the hydraulic head simulated by the model at WSP-12.

The hydraulic head difference of the field measurement data of the standpipe PB-12 and pore pressure gauge WSP-12, indicates that the hydraulic head decreases between the crest (PB-12) and inner (WSP-12) toe of the dike. Because the change in the hydraulic head of the field measurement data is greater than the change in head determined by the FEM model, the FEM model underestimates the hydraulic gradient of the Hout-Blerick dike section. During the piping assessment, must be kept in mind that the true hydraulic gradient is almost certainly greater than the one determined by the FEM model.

Buggenum
The calibration error for Buggenum does not exceed the criterion's maximum calibration error, indicating that the model calibration result is adequate. The small calibration error is most likely due to the short foreland assumption being applicable in Buggenum due to the presence of a channel shortly in front of the dike (see Figure C.3 in Appendix C). The water level in the channel has a significant impact on the hydraulic head development under the dike and is measured by standpipe PB-13, which serves as boundary condition input. The implementation of the boundary conditions is analogous to having a water body in the foreland and/or hinterland in reality, as is the case for the research location Buggenum.

Due to time constraints, better schematizations for the geometry of the cross-sectional model (subsoil layering) or an assumption to include the above-mentioned external influences could not be found. As a result, it was decided to continue the research using the calibration results shown in Figures 3.22, 3.23 and 3.24. Appendix D sums up the model parameters used in the following chapters.

$$4$$
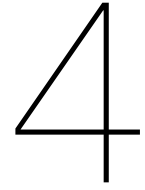
Deterministic piping assessment

This chapter evaluates piping analytically using the original and revised Sellmeijer design rule, as well as numerically using the FEM models proposed in Chapter 3. All analyses in this chapter are performed deterministically. To begin, the critical head of each dike cross-section of the research locations is determined analytically, using both Sellmeijer design rules. Second, for each research location, a deterministic piping assessment is performed using the proposed cross-sectional models. Within the cross-sectional models, the analytically derived critical heads using Sellmeijer design rules serve as the loading conditions.

4.1. Analytical piping assessment using the Sellmeijer design rule

This section assesses piping analytically with two forms of the Sellmeijer design rule. Both design rules are demonstrated below to display the difference between the two, which is present in the scale factor (F_s).

The design rule derived from the Sellmeijer model (Sellmeijer, 1988) with the new geometric factor as presented by Sellmeijer et al. (2011) is referred to as the 'original Sellmeijer design rule' in this thesis (see Equation 4.1). The new geometric factor represents the 2 forces approach.

The original Sellmeijer design rule is the predecessor of the design rule that is now commonly used to evaluate piping, which is referred to as the revised Sellmeijer design rule (Rijkswaterstaat, 2021) (see Equation 4.2). The revised Sellmeijer design rule was derived in 2011, as a result of experimental research and regression through the results (see Section 2.2).

Original Sellmeijer design rule (1988/2011)	**Revised Sellmeijer design rule** (2021)
$$\frac{H_{c,o}}{L} = \frac{1}{c} = F_R F_{S,o} F_G$$ $$F_R = \eta \frac{\gamma'_{sp}}{\gamma_w} \tan\theta$$ $$F_{S,o} = \frac{d_{70}}{\sqrt[3]{\kappa L}}$$ $$F_G = 0.91 \left(\frac{D}{L}\right)^{\left(\frac{0.28}{\left(\frac{D}{L}\right)^{2.8}-1}+0.04\right)}$$ $$(4.1)$$	$$\frac{H_{c,rev}}{L} = \frac{1}{c} = F_R F_S F_G$$ $$F_R = \eta \frac{\gamma'_{sp}}{\gamma_w} \tan\theta$$ $$F_{S,rev} = \frac{d_{70m}}{\sqrt[3]{\kappa L}}\left(\frac{d_{70}}{d_{70m}}\right)^{0.4}$$ $$F_G = 0.91 \left(\frac{D}{L}\right)^{\left(\frac{0.28}{\left(\frac{D}{L}\right)^{2.8}-1}+0.04\right)}$$ $$(4.2)$$

Several factors must be considered before applying the Sellmeijer design rule to the research locations. When working with a groundwater system consisting of multiple soil layers, Waterschap Limburg (2020) and Rijkswaterstaat (2021) recommend using a permeability (κ_a) scaled over the thickness of the aquiferous layers (see Equation 4.3 and Equation 4.4 (Rijkswaterstaat, 2021)). Furthermore, when applying

the Sellmeijer design rule on a dike in Limburg where d_{70} is greater than the applicability range of the revised Sellmeijer design rule (2021) (150 μm $\leq d_{70} \leq$ 430 μm) allows, the calculated critical head should be multiplied by a factor of 1.8 (Waterschap Limburg, 2020) (see Sections 2.2 and 2.3.2).

$$K_a = \frac{K_1 D_1 + K_2 D_2 + ...}{D_1 + D_2 + ...} \qquad (4.3)$$

$$\kappa_a = \frac{K_a \cdot v}{g} \qquad (4.4)$$

For each research location an analytical calculation of the critical head according to the original ($H_{c,o}$ (1988/2011)) and revised ($H_{c,rev}$ (2021)) Sellmeijer design rule is performed. The critical head multiplied by the factor 1.8 is also presented for both design rules. The results are shown in Table 4.1, where the height of the dike crest is also implemented for comparison.

Table 4.1: Analytical results Sellmeijer design rules

	$H_{c,o}$ [m] (1988/2011)	1.8 $H_{c,o}$ [m] (1988/2011)	$H_{c,rev}$ [m] (2021)	1.8 $H_{c,rev}$ [m] (2021)	Crest height [m]
Well	3.33	5.99	1.67	3.00	2.25
Hout-Blerick	3.53	6.34	2.08	3.75	5
Buggenum	4.65	8.37	1.93	3.47	4.10
Thorn	1.66	2.98	1.03	1.85	2.46

The model parameters that are used for the calculations are included in Appendix D. It should be noted that, in order to objectively assess the design rule, these results are obtained without using any safety factors other than those already used in Equations 4.1 and 4.2. For example, the average of the expected d_{70} that is found in samples at the research locations is used in the calculations.

The results of both the Sellmeijer design rules (1988/2011) (2021) and the dike crest level (as shown in Table 4.1) are used as input values for the boundary conditions of the outside water level in cross-sectional models.

Analytical Sellmeijer calculation for Well
To demonstrate how analytical calculations are performed with the Sellmeijer design rules, that lead to the results in Table 4.1, the calculation for the dike section near Well is included. The example includes the calculation with the original Sellmeijer design rule (1988/2011) and the revised design rule (2021). Similar calculations are performed for the other research locations using different input parameters included in Appendix D. The calculation is carried out step by step and the input parameters are shown in Table D.3 in Appendix D.

To calculate the critical head using the Sellmeijer design rules, the resistance, scale, and geometric factor must first be determined. The factors are computed in the order specified. The scale factor distinguishes the original and revised Sellmeijer design rules. Therefore, a distinction is made in Equation 4.1 and Equation 4.2 and the scale factor is expressed as $F_{S,o}$ (1988/2011) and $F_{S,rev}$ (2021). An elaborate description of the factors and the implemented constants are given in Section 2.2 and Section 3.1.2 and is only repeated shortly in this section.

The resistance factor of the Sellmeijer design rule describes the roll resistance of the sand particles against the groundwater flow. The resistance input parameters are captured by Sellmeijer et al. (2011) and are used consistently in all piping research and assessments.

$$F_R = \eta \frac{\gamma'_{sp}}{\gamma_w} \tan\theta = 0.25 \frac{26.5}{10} \tan(37) = 0.311$$

The scale factor is the second factor to be calculated. The scale factor in the revised Sellmeijer design rule (2021) has been calibrated to a series of research experiments. This factor change determines the

difference between the original (1988/2011) and revised Sellmeijer design rules and is thus calculated in both ways. Before calculating the scale factor, the aquifer permeability must be determined with Equation 4.3.

$$K_a = \frac{K_1 D_1 + K_2 D_2 + ...}{D_1 + D_2 + ...} = \frac{D_{sand} K_{sand} + D_{grav} K_{grav}}{D_{sand} + D_{grav}} = \frac{3 \cdot 48 + 11 \cdot 125}{3 + 11} = 108.5 \text{ m/d} = 0.0013 \text{ m/s}$$

$$\kappa_a = \frac{K_a \cdot v}{g} = \frac{0.0013 \cdot 1.33 \cdot 10^{-6}}{9.81} = 1.70 \cdot 10^{-10} \text{ m}^2$$

$$F_{S,o} = \frac{d_{70}}{\sqrt[3]{\kappa L}} = \frac{6.6 \cdot 10^{-4}}{\sqrt[3]{1.70 \cdot 10^{-10} \cdot 24}} = 0.413$$

$$F_{S,rev} = \frac{d_{70m}}{\sqrt[3]{\kappa L}} \left(\frac{d_{70}}{d_{70m}} \right)^{0.4} = \frac{2.08 \cdot 10^{-4}}{\sqrt[3]{1.70 \cdot 10^{-10} \cdot 24}} \left(\frac{6.6 \cdot 10^{-4}}{2.08 \cdot 10^{-4}} \right)^{0.4} = 0.206$$

The last factor is the geometric factor, which is identical in Equation 4.1 and Equation 4.2. The geometric factor is determined for the total aquifer depth, which is the sum of the layer thicknesses with the exception of the clay layer. For simplicity, the exponent in the formula of the geometric factor (B) is determined separately beforehand. The geometric factor requires the seepage length as input. The seepage length is always chosen to be equal to the width of the dike because the clay layer at the research locations is relatively permeable compared to other cover layers in the rest of the Netherlands. This can result in uniform seepage flow through the clay layer, meaning that the shortest seepage path starts at the outside toe of the dike and ends at the inner dike toe.

$$D_a = D_1 + D_2 + ... = D_{sand} + D_{grav} = 3 + 11 = 14 \text{ m}$$

$$B = \frac{0.28}{\left(\frac{D}{L} \right)^{2.8} - 1} + 0.04 = \frac{0.28}{\left(\frac{14}{24} \right)^{2.8} - 1} + 0.04 = -0.319$$

$$F_G = 0.91 \left(\frac{D}{L} \right)^B = 0.91 \left(\frac{14}{24} \right)^{-0.319} = 1.081$$

Now all necessary factors to determine the critical head with the original Sellmeijer design rule ($H_{c,o}$) and the revised design rule ($H_{c,rev}$) are calculated. The critical head according to the original (1988/2011) and the revised Sellmeijer design rule (2021) is:

$$H_{c,o} = F_R F_{S,o} F_G L = 0.311 \cdot 0.413 \cdot 1.081 \cdot 24 = 3.33 \text{ m}$$

$$H_{c,rev} = F_R F_{S,rev} F_G L = 0.311 \cdot 0.206 \cdot 1.081 \cdot 24 = 1.67 \text{ m}$$

The applied d_{70} = 660 μm lies outside the range of application of the revised Sellmeijer design rule (2021) (150 μm $\leq d_{70} \leq$ 430 μm), therefore according to the Waterschap Limburg (2020), the determined critical head should be multiplied by a factor 1.8. This should create a more realistic critical head and reduce the degree of conservatism in the piping assessment. However, in some cases, the calculated critical head becomes higher than the dike crest level, which is impossible.

4.2. Numerical piping assessment

The objective of the FEM numerical models is to simulate site-specific groundwater flow systems, including groundwater flow through the pipe. The most important output from the models is the average hydraulic gradient that is used to assess the possibility of piping at the research locations. The hydraulic gradient corresponding to hydraulic head changes in the pipe itself is called the local hydraulic gradient. The model parameters that compose the cross-sectional models for the deterministic piping assessment are included per research location in Appendix D.

To assess piping, the local hydraulic gradient derived with the cross-sectional models is compared with the critical gradient imposed by the 2 forces method (see Section 3.1.2). If the local hydraulic gradient is larger than the 2 forces gradient, piping can occur. However, both gradients depend on the pipe geometry in the model. The choice of schematization for the shape of the cross section of the pipe is discussed in Section 3.1, but it remains unknown how to schematize the height of the pipe. Therefore, the simulated hydraulic gradient and the critical gradient from the 2 forces are both determined as a function of the pipe height. The height of the pipe (a [m]) is always expressed as a function of the number of grains (n_g [-]) and the representative grain size, d_{70}:

$$a = n_g \cdot d_{70} \tag{4.5}$$

Subsequently, the piping assessment becomes dependent on the pipe height expressed in number of grains. The criterion is established that piping can only occur for realistic pipe heights, but since the true pipe height remains unknown, the criterion is based on the proposition of Van Esch et al. (2013). According to them, the pipe height ranges from 0 to 3 grains in small-scale experiments, 0 to 10 grains in field experiments, and 0 to 30 grains in real dikes. As a result, the piping criterion is set that the pipe height should be at least 3 grains.

Two piping analyses for different pipe lengths were performed for each research location. The models in the first analysis, assess piping for a pipe length equal to 10% of the dike width (0.1L). In the second analysis, a pipe is assessed that has developed until approximately the midpoint of the dike. This is according to Sellmeijer (1988) the critical pipe length; once the pipe grows beyond this length erosion continues independently of the external loading conditions until failure of the dike. The critical pipe length is expressed as 44% of the dike width (0.44L) (Sellmeijer & Koenders, 1991).

The short pipe analysis (0.1L) is used to determine whether the hydraulic gradient is sufficient to make the pipe grow beyond 10% of the dike width. The hydraulic gradient for a pipe length of 10% of the dike width, is expected to be greater than for longer pipes, because the presence and size of the pipe dampens the hydraulic gradient that initiates piping. That is, if the hydraulic gradient is insufficient to induce piping for a pipe length equal to 10% of the dike width, the pipe cannot develop until it reaches the critical pipe length, and the second length analysis (0.44L) is irrelevant.

The cross-sectional models require an input of the outside water level at the domain boundary that functions as the external loading conditions for the piping assessment. To assess the applicability of the Sellmeijer design rules (Equations 4.1 and 4.2) at the research locations, the results of the Sellmeijer design rules as presented in Table 4.1, are used as input for boundary conditions in the cross-sectional models. These results represent the critical hydraulic head according to the original Sellmeijer design rule (1988/2011), the revised Sellmeijer design rule (2021) and their multiplication with 1.8, so whenever these water levels are exceeded, piping occurs and thus the average hydraulic gradient from the numerical model should surpass the critical gradient from the 2 forces method. An outside water level equal to the crest level is also analyzed, as this is the maximum water level that can stand against the dike.

Another output parameter from the cross-sectional models is the Reynolds number (R_e) of the flow inside the pipe. The Reynolds number indicates whether the flow is in a laminar ($R_e < 2300$), transitional ($2300 < R_e < 3500$) or turbulent ($R_e > 3500$) regime. The main principles of the piping model (Darcy's law, Hagen-Poiseuille flow and the conceptual model of Sellmeijer (Sellmeijer, 1988), see Section 3.1), are built on the assumption of laminar flow in the pipe. To be able to enforce these principles, it must be proven that a laminar flow regime is present inside the pipe of the numerical models. The Reynolds number is derived by:

$$R_e = \frac{uD_h\rho}{\mu} = \frac{u \cdot 2a \cdot \rho}{\mu} = \frac{u \cdot 2n_g d_{70} \cdot \rho}{\mu} \tag{4.6}$$

The Reynolds number is a function of the hydraulic diameter (D_h [m]) of the pipe cross section, the flow velocity in the pipe (u [m/s]), fluid density (ρ [kg/m^3]) and the dynamic viscosity of the fluid (μ [kg/m·s]) (Aguilar-López et al., 2016a). The hydraulic diameter corresponding to a fracture flow cross-section is equal to twice the pipe height ($2a$). Subsequently, the Reynolds number is examined as a function of the number of grains, similarly to the hydraulic gradient analysis.

4.2.1. Well

For the research location Well, Figures 4.1a and 4.1b demonstrate the hydraulic head development across the dike and the average hydraulic gradient for a pipe length of 10% of the dike width (0.1L). Figures 4.2a and 4.2b display the hydraulic head development over the dike and the average hydraulic gradient for a pipe length equal to 44% of the dike width (0.44L).

(a) Hydraulic head across the dike width

(b) Hydraulic gradient as a function of the number of grains (discontinuity due to interpolation)
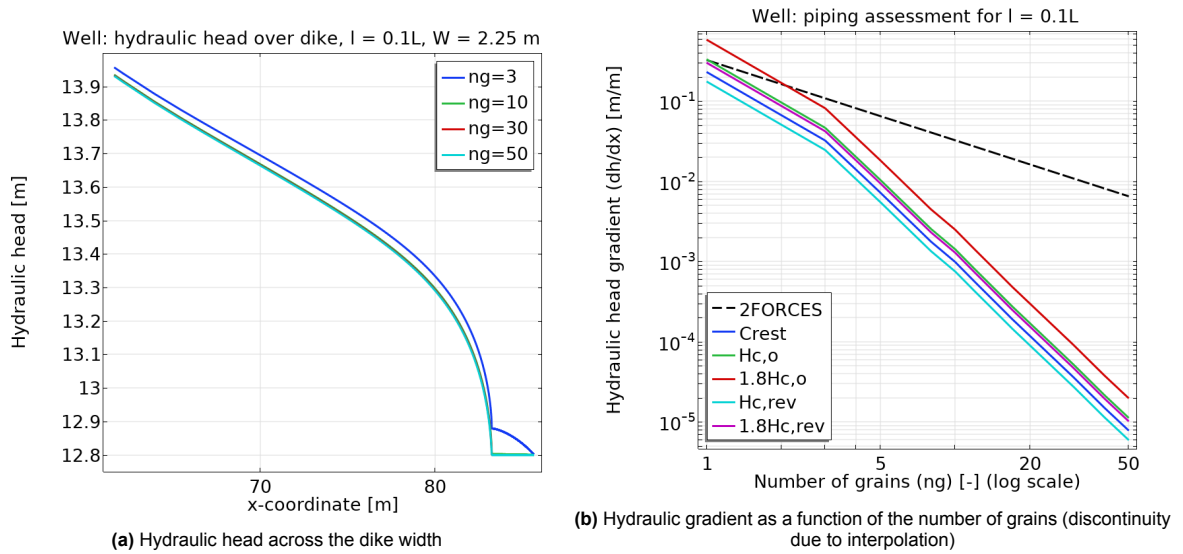
Figure 4.1: Well: deterministic piping assessment for pipe length 0.1L

(a) Hydraulic head across the dike width

(b) Hydraulic gradient as a function of the number of grains (discontinuity due to interpolation)
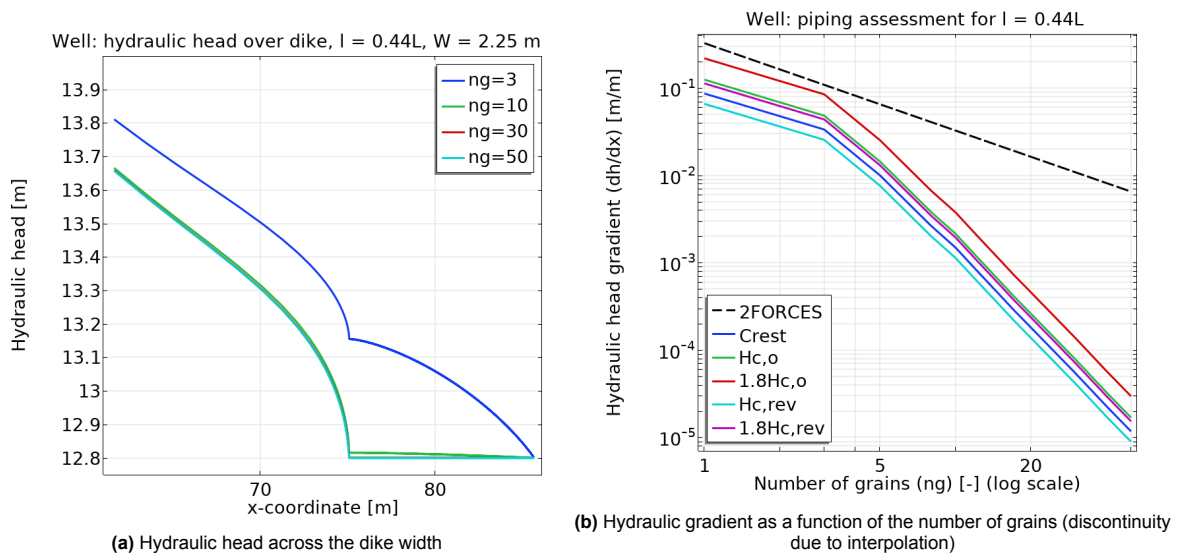
Figure 4.2: Well: deterministic piping assessment for pipe length 0.44L

The hydraulic head in Figures 4.1a and 4.2a is calculated for an outside water level equal to the crest level of the dike (W = 2.25 m). The hydraulic head is determined in the aquifer along a horizontal line that spans the entire width of the dike (through the unaffected aquifer and the pipe) and lies on a vertical level equal to the pipe's center.

The hydraulic gradient in Figures 4.1b and 4.2b is expressed as a function of the pipe height (number of grains) and is compared to the critical gradient of the 2 forces method for 5 different outside water levels. With increasing pipe height, the hydraulic gradient decreases and becomes very small (order 10^{-5}). A similar trend can seen in Figures 4.1a and 4.2a, where the hydraulic head in the pipe becomes nearly constant for pipe heights of 10 grains or greater.

The analysis of the hydraulic gradient for a short pipe length (0.1L) (see Figure 4.1b) results in a similar plot as demonstrated in the analysis of the pipe length equal to 0.44L. For pipes larger than approximately 5 grains, the hydraulic gradient of the 0.1L pipe length analysis lies generally just below the hydraulic gradient determined for a pipe length of 0.44L.

For pipes with a length of 0.1L, the hydraulic gradient for the most extreme water level analyzed ($1.8H_{c,o} = 5.99$ m) exceeds the 2 forces critical gradient (dashed black line) for a pipe height consisting of 2.3 grains (see Figure 4.1b). This implies that pipe growth continues for pipes with pipe heights of 2.3 grains or less, for an outside water level of 5.99 m. However, the realistic pipe height criterion states that the pipe height should consist of at least 3 grains. Therefore is concluded that the hydraulic gradient is insufficient to drive piping beyond 10% of the dike width and the analysis for a pipe length of 0.44L is irrelevant.

From Figure 4.2b, can be seen that the 2 forces critical gradient (dashed black line) is not intersected by the graphs of the hydraulic gradients for a pipe length of 0.44L. This suggests that calculated critical heads using the original (1988/2011) and revised Sellmeijer design rule (2021) ($H_{c,o}$ and $H_{c,rev}$ from Table 4.1) do not lead to piping at the research location Well for a pipe length of 0.44 times the dike width.

Table 4.2: Flow regime analysis Well: 0.1L; W = 2.25 m

n_g [-]	dh/dx_{2F} [m/m]	dh/dx_{FEM} [m/m]	R_e [-]
3	0.10850	0.032287	304.60
10	0.032551	9.9056E-4	346.11
20	0.016276	1.1850E-4	331.24
30	0.010850	3.5992E-5	339.54
40	0.0081378	1.4923E-5	333.70
50	0.0065102	7.8101E-6	341.11

Table 4.3: Flow regime analysis Well: 0.44L; W = 2.25 m

n_g [-]	dh/dx_{2F} [m/m]	dh/dx_{FEM} [m/m]	R_e [-]
3	0.10850	0.033439	315.46
10	0.032551	0.0014909	520.92
20	0.016276	1.8033E-4	504.05
30	0.010850	5.4509E-5	514.23
40	0.0081378	2.2645E-5	506.37
50	0.0065102	1.1739E-5	512.71

Using Equation 4.6, the Reynolds number has been derived for flow in the pipe consisting of a length of 0.1L and 0.44L and an outside water level equal to the crest height (W = 2.25 m). The Reynolds number and corresponding hydraulic gradient for the cross-sectional model of Well are shown in Tables 4.2 and 4.3. The Reynolds numbers in both tables indicate that a laminar flow regime is present in the pipe, independent of the pipe height and pipe length. It can be concluded that the Reynolds number is larger for the longer pipe, but this pipe length is irrelevant for Well. In both cases (0.1L and 0.44L), can be seen that the Reynolds number does not grow proportionally to the pipe height.

4.2.2. Hout-Blerick

The hydraulic head development over the dike and hydraulic gradient analyses for Hout-Blerick are demonstrated in Figures 4.3a and 4.3b for a pipe length equal to 10% of the dike width (0.1L) and in Figures 4.4a and 4.4b for a pipe length of 44% of the dike width (0.44L). The analyses are performed in a manner similar as just discussed for Well, with the cross-sectional model of Hout-Blerick and the critical heads of Table 4.1 for Hout-Blerick are implemented as input outside water levels.

Figures 4.3a, 4.3b, 4.4a and 4.4b and Tables 4.4 and 4.5 demonstrate that the hydraulic gradient decreases with increasing pipe height. Similarly to the results of Well, the hydraulic gradients for the Hout-Blerick cross-sectional model containing the shorter pipe length (0.1L), are greater for smaller pipe heights ($n_g < 5$), but lower for larger pipe heights ($n_g > 5$) compared to the hydraulic gradients

derived with the longer pipe length (0.44L). This can be seen in Figures 4.3b and 4.4b, but even more clearly by comparing the values of the hydraulic gradient in Tables 4.4 and 4.5.

In the 0.1L pipe length analysis, the hydraulic gradient for the maximum water level of $1.8H_{c,0} = 6.34$ m exceeds the critical gradient for a pipe height of 1.2 grains (see Figure 4.3b). This means that for a pipe height of 1.2 grains or less, the pipe can grow beyond 10% of the dike width. However, the pipe height criterion deems this pipe height unrealistic, so it is concluded that piping does not exceed 10% of the dike width. Subsequently, at a pipe length of 44% of the dike width, the hydraulic gradients of the different water levels do not exceed the critical gradient of the 2 forces method (see Figure 4.4b).

(a) Hydraulic head across the dike width

(b) Hydraulic gradient as a function of the number of grains (discontinuity due to interpolation)
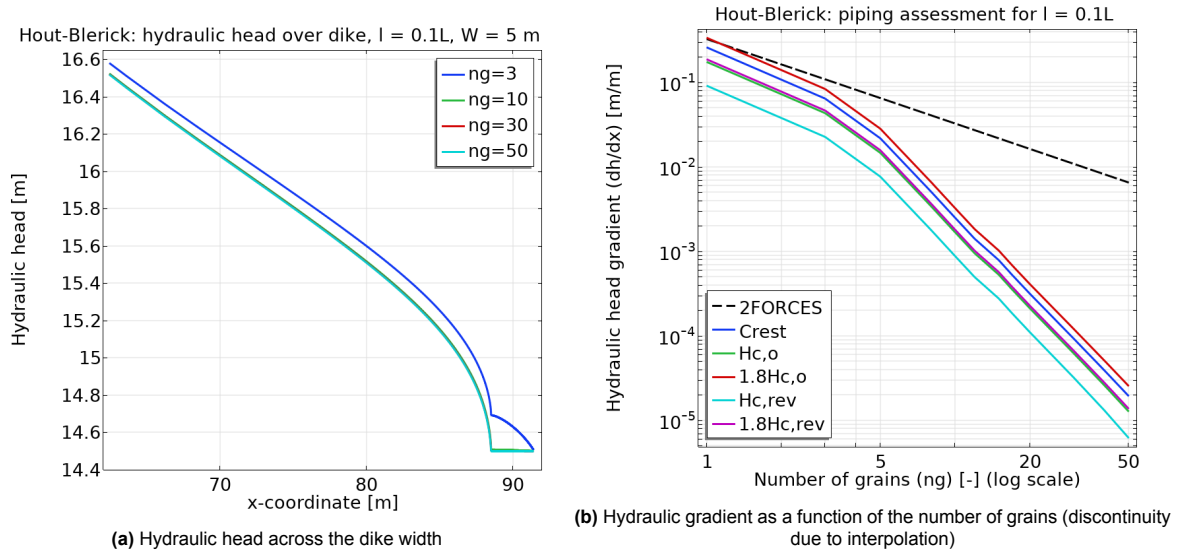
Figure 4.3: Hout-Blerick: deterministic piping assessment for pipe length 0.1L

(a) Hydraulic head across the dike width

(b) Hydraulic gradient as a function of the number of grains (discontinuity due to interpolation)
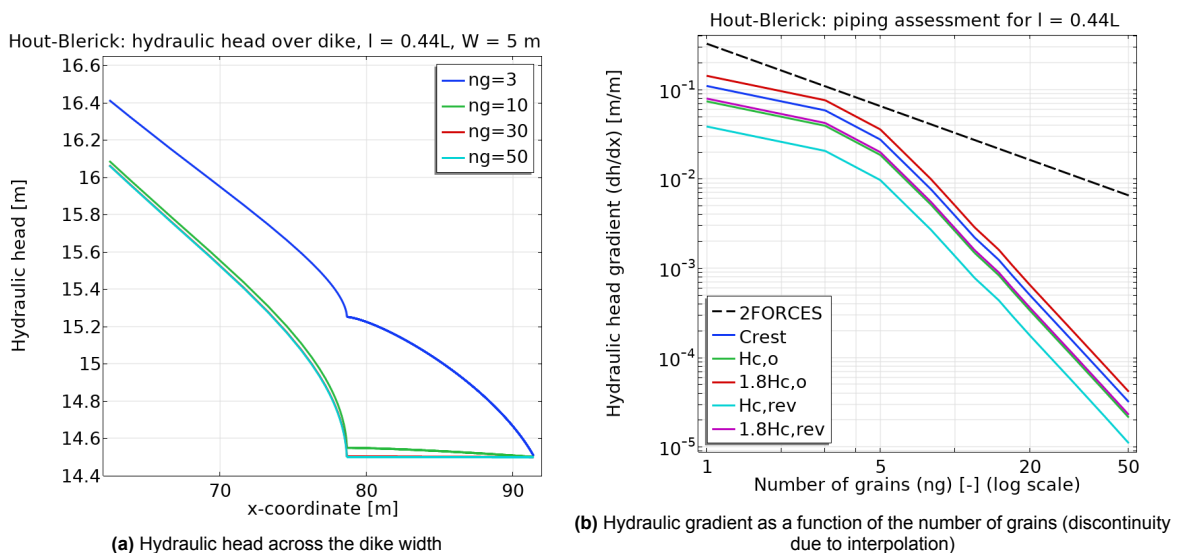
Figure 4.4: Hout-Blerick: deterministic piping assessment for pipe length 0.44L

For the Hout-Blerick cross-sectional model must be assessed whether the flow in the pipe is in a laminar flow regime. This analysis is carried out for the outside water level equal to the crest height (W = 5 m) because this is the maximum water level that can stand against the dike in reality. From Tables 4.4 and 4.5 can be seen that the flow in the pipe is laminar, regardless of the pipe height or length. This analysis shows that the Reynolds number increases as the length of the pipe increases. The pipe

height appears to make the Reynolds number increase as well, but not proportionally.

Table 4.4: Flow regime analysis Hout-Blerick: 0.1L; W = 5 m

Table 4.5: Flow regime analysis Hout-Blerick: 0.44L; W = 5 m

n_g [-]	dh/dx_{2F} [m/m]	dh/dx_{FEM} [m/m]	R_e [-]	n_g [-]	dh/dx_{2F} [m/m]	dh/dx_{FEM} [m/m]	R_e [-]
3	0.10850	0.064132	263.05	3	0.10850	0.058292	239.10
10	0.032551	0.0024956	379.12	10	0.032551	0.0038507	584.99
20	0.016276	3.1438E-4	382.08	20	0.016276	4.9899E-4	606.44
30	0.010850	9.2737E-5	380.38	30	0.010850	1.4844E-4	608.88
40	0.0081378	3.8620E-5	375.49	40	0.0081378	6.2453E-5	607.21
50	0.0065102	1.9303E-5	366.55	50	0.0065102	3.1774E-5	603.37

4.2.3. Buggenum

The cross-sectional model of Buggenum is different from the cross-sectional models of the other research locations. The Buggenum model contains a short foreland length of 3 m, while the others contain a foreland length equal to the leakage length, which is in the order of 60 m. The same analyses have been performed for Buggenum with the corresponding water levels from Table 4.1, as before discussed for Well and Hout-Blerick.

For a pipe length of 0.1L the critical gradient is exceeded for a pipe height of 3.4 grains in combination with the maximum implemented water level ($1.8H_{c,o} =$8.37 m) (see Figure 4.5b). Implying that the pipe can grow beyond 10% of the dike width. Now, it is necessary to perform the analysis for the critical pipe length (0.44L).

Figure 4.6b demonstrates that for a pipe length of 0.44L and the maximum implemented water level, the hydraulic gradient exceeds the 2 forces critical gradient for a pipe height of approximately 4.5 grains. These results imply that piping can occur in Buggenum for pipes with a pipe height less than 4.5 grains. This pipe height is deemed realistic according to the pipe height criterion set before.

Theoretically, Figure 4.6b shows that piping can occur at the dike cross-section near Buggenum. However, the only water level that lead to piping is the maximum implemented water level ($1.8H_{c,o} =$8.37 m). It should be kept in mind that this level of water exceeds the level of the crest height (W = 4.1 m). For an outside water level equal to the crest level the critical gradient is not exceeded in either pipe length configuration (0.1L and 0.44L).

(a) Hydraulic head across the dike width

(b) Hydraulic gradient as a function of the number of grains (discontinuity due to interpolation)
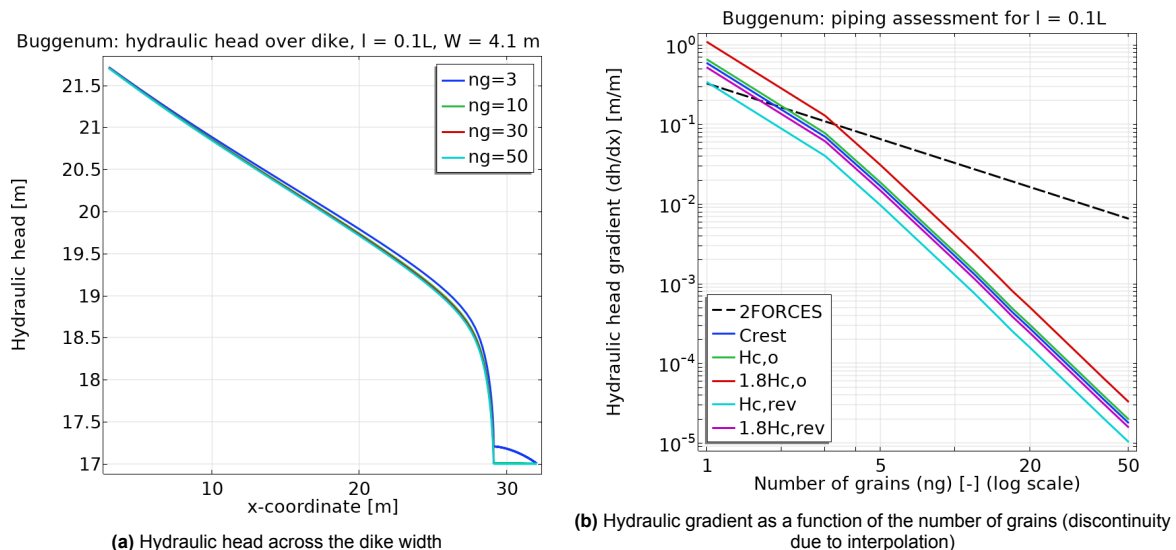
Figure 4.5: Buggenum: deterministic piping assessment for pipe length 0.1L

(a) Hydraulic head across the dike width

(b) Hydraulic gradient as a function of the number of grains (discontinuity due to interpolation)
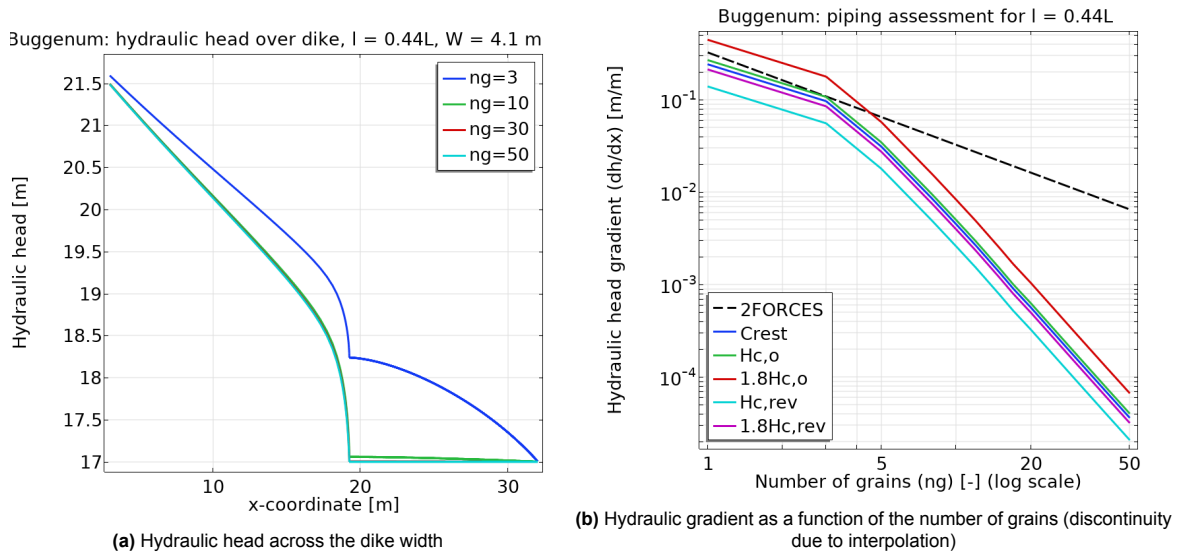
Figure 4.6: Buggenum: deterministic piping assessment for pipe length 0.44L

Table 4.6: Flow regime analysis Buggenum: 0.1L; W = 4.1 m   **Table 4.7:** Flow regime analysis Buggenum: 0.44L; W = 4.1 m

n_g	dh/dx_{2F}	dh/dx_{FEM}	R_e
[-]	[m/m]	[m/m]	[-]
3	0.10850	0.064132	1658.0
10	0.032551	0.0022043	1953.0
20	0.016276	2.7307E-4	1935.5
30	0.010850	8.0855E-5	1934.2
40	0.0081378	3.4111E-5	1934.2
50	0.0065102	1.7675E-5	1957.5

n_g	dh/dx_{2F}	dh/dx_{FEM}	R_e
[-]	[m/m]	[m/m]	[-]
3	0.10850	0.096520	2308.9
10	0.032551	0.0045096	3995.4
20	0.016276	5.6553E-4	4008.4
30	0.010850	1.6642E-4	3981.0
40	0.0081378	7.0280E-5	3985.1
50	0.0065102	3.6194E-5	4008.4

The Reynolds number of flow in the pipes of the cross-sectional models of Buggenum is much higher than previously observed at Well and Hout-Blerick. For the short pipe length (0.1L, see Table 4.6) the flow in the pipe is laminar, but the Reynolds number is still one order of magnitude higher than observed in the analyses of Well and Hout-Blerick. Table 4.7 demonstrates that flow in pipes with pipe heights equal to 10 grains or larger is in the turbulent flow regime ($R_e > 3500$), for a pipe length of 0.44L. The reason for the high Reynolds number is investigated in Appendix E.

4.2.4. Thorn

The final deterministic analyses are performed for the cross-sectional model of Thorn. In Section 3.4 has been discussed that even during extreme conditions, such as the flood event of 2021, the direction of seepage flow beneath the dike remains in the direction of the foreland and the lake 'De Grote Hegge'. Piping cannot occur unless groundwater flows in the opposite direction, toward the hinterland. As a result, it can be concluded that piping is not a dominant failure mechanism of the dike section at Thorn's research location. Despite this conclusion, the research location near Thorn has been treated as if piping is a relevant failure mechanism, which means that a cross-sectional model is built and the deterministic piping analysis is performed in the same way as for the other research location.

The hydraulic gradient of the pipe with a length equal to 10% of the dike width (0.1L) and calculated with the highest implemented water level ($1.8Hc,o = 2.91$ m), exceeds the critical gradient for a pipe height consisting of 1.2 grains (see Figure 4.7b). These results imply that, in theory, it is possible for the pipe to grow past 10% of the dike width with a pipe height equal to or smaller than 1.2 grains. However, the pipe height criterion deems this pipe height unrealistic, concluding that the piping does not continue beyond 10% of the dike width.

(a) Hydraulic head across the dike width

(b) Hydraulic gradient as a function of the number of grains (discontinuity due to interpolation)
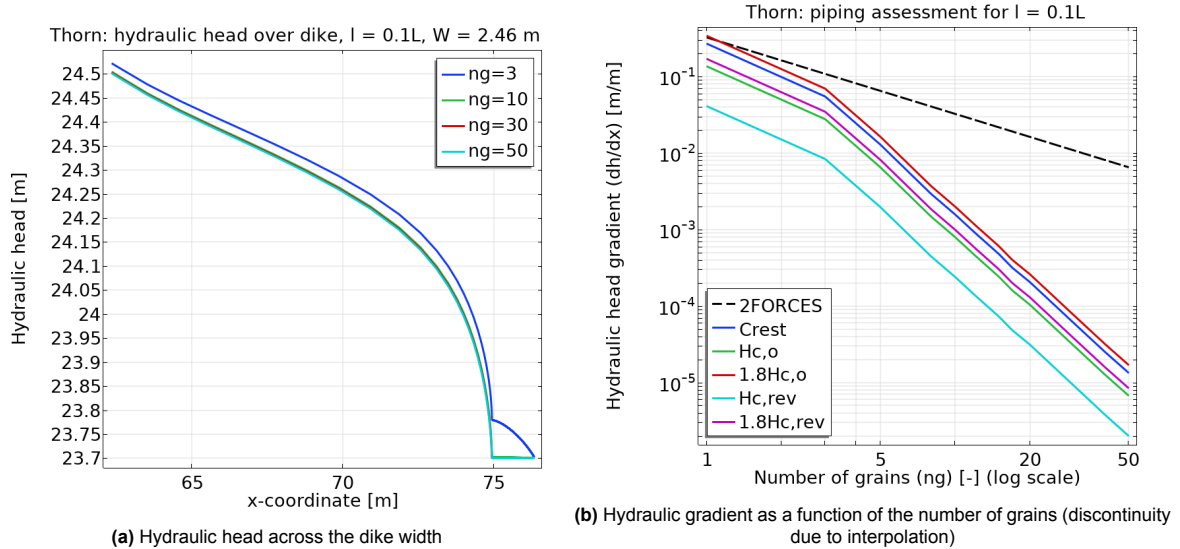
Figure 4.7: Thorn: deterministic piping assessment for pipe length 0.1L

(a) Hydraulic head across the dike width

(b) Hydraulic gradient as a function of the number of grains (discontinuity due to interpolation)
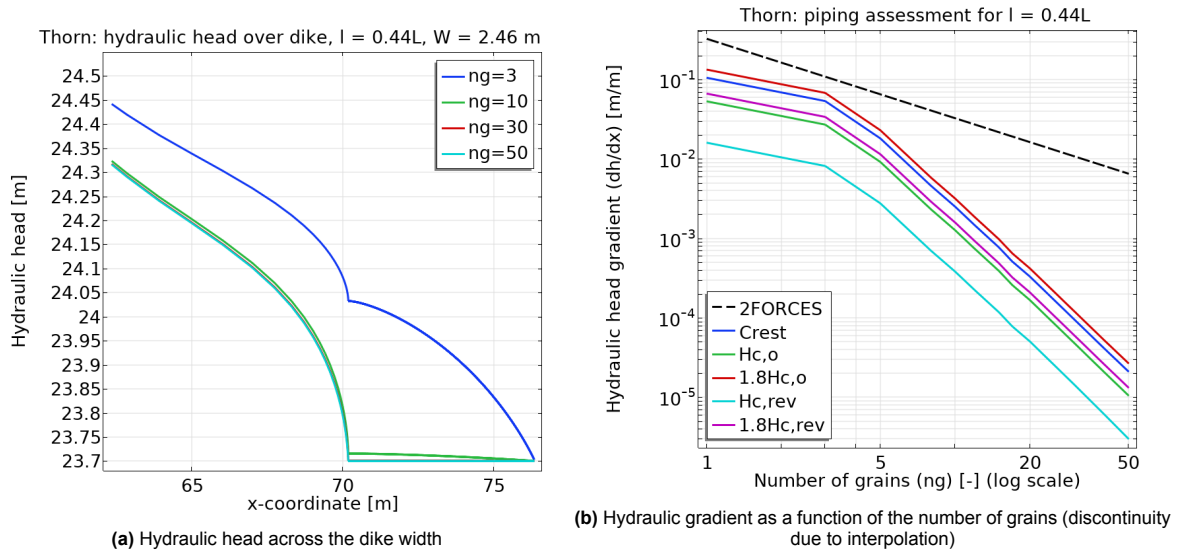
Figure 4.8: Thorn: deterministic piping assessment for pipe length 0.44L

Figures 4.8a and 4.8b demonstrate the hydraulic head development across the dike and the hydraulic gradient for a pipe length equal to 44% of the dike width (0.44L). From these figures, it can be seen that the hydraulic gradient decreases for larger pipe heights, and the hydraulic gradients for different water levels do not exceed the critical gradient determined with the 2 forces method (black dashed line). This implies that erosion of the grains does not occur for pipes with a pipe length of 44% of the dike width. Therefore, piping cannot cause the dike to fail.

For both pipe length conditions (0.44L and 0.1L) the Reynolds number of flow in the pipe has been derived for different pipe heights in combination with an outside water level equal to the crest level. From the values for the Reynolds number in Tables 4.8 and 4.9 can be derived that the flow in the pipe is laminar ($R_e < 2300$). This result holds independent of the pipe length and pipe height.

Table 4.8: Flow regime analysis Thorn: 0.1L; W = 2.46 m

| n_g | dh/dx_{2F} | dh/dx_{FEM} | R_e |
[-]	[m/m]	[m/m]	[-]
3	0.10850	0.054862	164.05
10	0.032551	0.0015742	174.34
20	0.016276	2.0546E-4	182.04
30	0.010850	6.0131E-5	179.80
40	0.0081378	2.5294E-5	179.28
50	0.0065102	1.3320E-5	184.40

Table 4.9: Flow regime analysis Thorn: 0.44L; W = 2.46 m

| n_g | dh/dx_{2F} | dh/dx_{FEM} | R_e |
[-]	[m/m]	[m/m]	[-]
3	0.10850	0.053501	159.98
10	0.032551	0.0025085	277.81
20	0.016276	3.3095E-4	293.21
30	0.010850	9.7181E-5	290.59
40	0.0081378	4.0703E-5	288.50
50	0.0065102	2.0965E-5	290.22

5

Stochastic evaluation of the Sellmeijer design rule

This chapter describes how the Sellmeijer design rule is stochastically evaluated using the proposed FEM numerical model. The geometry of the numerical model is adapted to perform stochastic analyses more efficiently. Afterwards, evaluation process begins with the creation of 1000 randomly generated dike cross-sections that are assessed on piping, which are called (piping) scenarios. These scenarios are then analyzed and the failure scenarios are used to evaluate the Sellmeijer design rule.

5.1. Model adaptation for stochastic analyses

The deterministic numerical piping assessment of Chapter 4 is performed with cross-sectional models including site-specific conditions to analyse piping for that specific dike section, as proposed in Sections 3.3 and 3.4. However, when the piping assessment is performed with stochastic parameters, the cross-sectional model is no longer consistent with the research locations. Therefore, a more general model geometry can be used in stochastic analyses to reduce computational demand and solving time (see Section 3.2.1). An analysis is carried out to determine to what extent the length of the foreland and the hinterland can be reduced in the model and the effect on the hydraulic gradient in the pipe. The stochastic analyses are performed for a pipe length equal to 44% of the dike width, which is according to Sellmeijer & Koenders (1991) the critical pipe length (0.44L).

In Section 3.3.6, the effect of the aquifer depth on the hydraulic gradient in the pipe is examined. Based on the findings, it is decided to reduce the total depth of the aquifer in the stochastic analyzes to 10 m. The change in hydraulic head gradient is more significant for shallower aquifer depths than aquifer depths deeper than 10 m.

Foreland and hinterland length reduction
Implementing a shorter foreland and hinterland length results in a more efficient model in stochastic analyses. Before doing so, the effect of the length of the foreland and hinterland on the hydraulic head and hydraulic gradient must be evaluated.

A variety of foreland and hinterland lengths are investigated for each research location. The legends of Figures 5.1, 5.2, 5.3 and 5.4 show the values of the varying lengths of the hinterland. Exactly the same values are implemented in the cross-sectional models for the foreland length, which is displayed on the horizontal axis. The markers in Figures 5.1, 5.2, 5.3 and 5.4 demonstrate the hydraulic gradient in the pipe (vertical axis) for the different foreland and hinterland length combinations. The lines through the markers display the trend effect of the varying length combinations. The intersection point of the yellow dotted line with the yellow trend line indicates the hydraulic gradient in the pipe for the combination in which the length of the foreland is equal to the length of the leakage and the length of the hinterland is three times the length of the leakage, which is the recommended value of Rijkswaterstaat (2021).
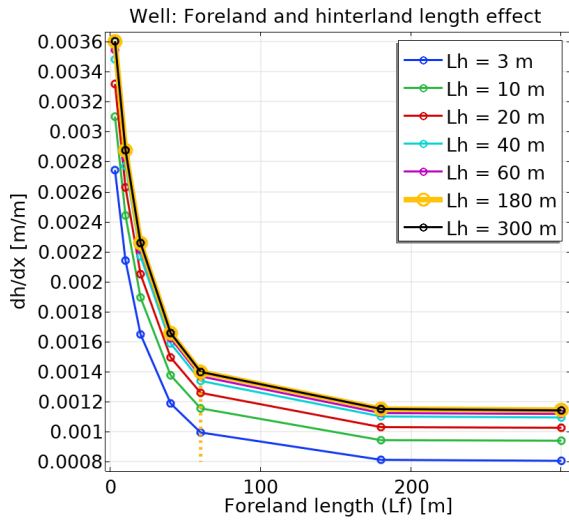
Figure 5.1: Well: foreland and hinterland effect
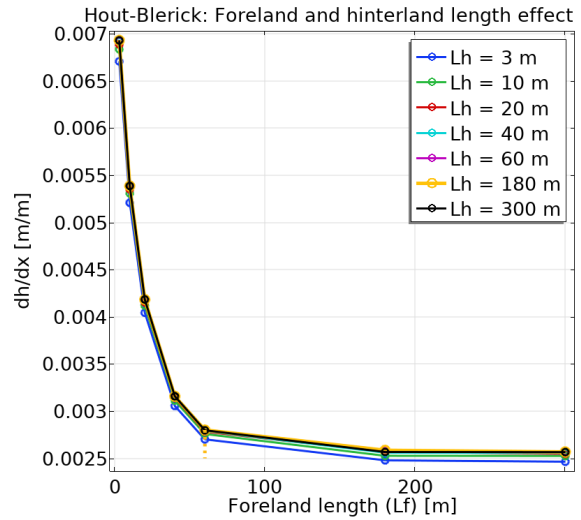
Figure 5.2: Hout-Blerick: foreland and hinterland effect
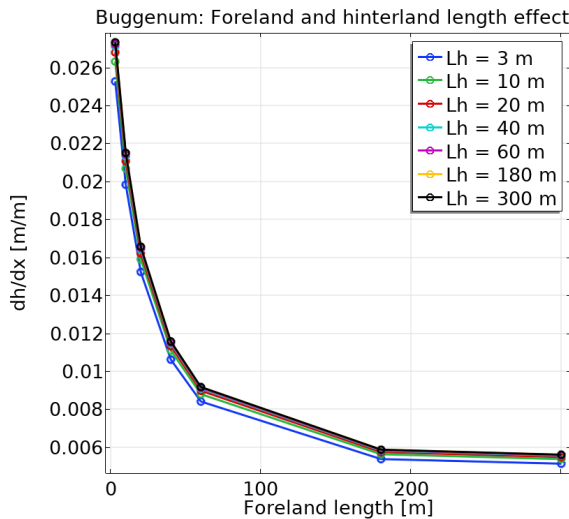
Figure 5.3: Buggenum: foreland and hinterland effect
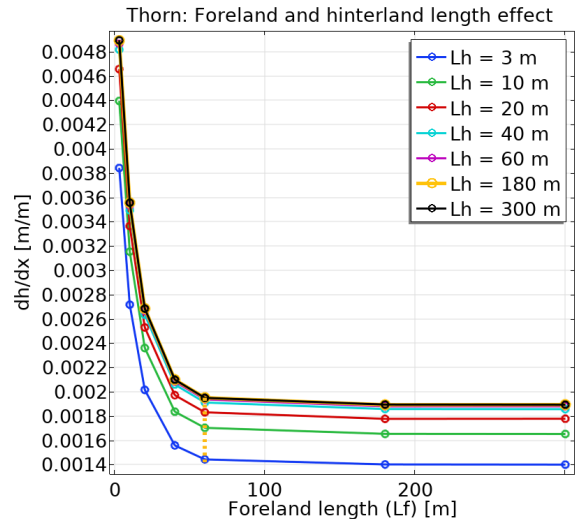
Figure 5.4: Thorn: foreland and hinterland effect

Figures 5.1, 5.2, 5.3 and 5.4 demonstrate the trend that a longer foreland length results in a low hydraulic gradient and the opposite applies for a short foreland length. The variation in foreland length causes the curving trend in the hydraulic gradient to change. For Figures 5.1 and 5.4 applies that the hinterland length variation (demonstrated in different colours) induces a total offset for the trend in the hydraulic gradient in the pipe. The influence of the hinterland length reaches an optimum, since the influence is almost negligible for lengths greater than 60 m.

It can be concluded that the lengths of the foreland and the hinterland affect the hydraulic gradient. However, the order of change induced in the hydraulic gradient will not be decisive for the overall piping assessment. In this study, the critical gradient, determined by the two forces method, varies approximately between 10^{-1} and 10^{-2} for a pipe height varying between 3 and 50 grains and the local d_{70} (see Section 4.2) and a pipe length of 0.44L. As a result, small changes in the hydraulic gradient of the order 10^{-3} or less are unlikely to be normative.

In light of the piping assessment, it is better to make a conservative estimation of the hydraulic gradient in the pipe. Since Figures 5.1, 5.2, 5.3 and 5.4 demonstrate that the hydraulic gradient in the pipe is more conservative for a shorter foreland and hinterland length, it is decided that the length of the foreland and hinterland in the numerical model can be reduced for the stochastic analyses. It is chosen

to generate the random piping scenarios from the stochastic analyses with a model geometry that contain a foreland length of 3 m and a hinterland of 20 m. From Figures 5.1, 5.2, 5.3 and 5.4 can be seen that this combination of foreland and hinterland length leads to relatively high hydraulic gradients in the pipe. A hinterland length of 20 m is chosen because a balance between hydraulic gradient change and model efficiency is found. When compared to the cross-sectional models in the deterministic piping analysis, the total model length implemented in the stochastic analysis is reduced by more than 200 m.

5.2. Stochastic model parameters

Multiple model parameters are implemented stochastically, to evaluate a wide range of combinations of model parameters and thus generate 1000 random piping scenarios. Each unique combination of model parameters represents a distinct dike cross-section (scenario). All stochastically implemented model parameters play a role in the piping assessment according to the original and revised Sellmeijer design rule as shown in Equations 4.1 and 4.2. The aquifer depth is not included as a stochastic parameter, because this is a geometry parameter that causes the model to be re-meshed and the influence is limited (see Sections 3.2.1 and 3.3.6).

The model parameters that are stochastically implemented in the numerical model are randomly chosen from uniform distributions. It is decided to perform the stochastic analysis solely with uniform distributions, meaning that every parameter value has the same probability of occurring, to minimize the probabilistic bias in the stochastic analysis. As a result, the failure probability of the randomly generated piping scenarios is the equal for each scenario. Table 5.1 displays the lower and upper bounds of the uniform distribution of each stochastic model parameter.

Table 5.1: Bounds of the uniform distribution of the model parameters

Parameter	Unit	Lower bound	Upper bound
Seepage length, L	[m]	0	100
Water level, W	[m]	1	16
Hydraulic conductivity, K_a	[m/s]	$4 \cdot 10^{-4}$	$3 \cdot 10^{-3}$
$\log(K_a)$	[-]	-4.4	-2.5
Grain size, d_{70}	[m]	$1 \cdot 10^{-4}$	$9 \cdot 10^{-4}$
Number of grains, ng	[-]	3	100

The bounds of the distribution of the seepage length and the water level are based on the values used by Sellmeijer (1988). In a comparison of the empirical results of the Bligh (1910) method and the theoretical results of Sellmeijer (1988), the hydraulic head that forms the outside water level varies between 0 and 16 m, and the variation of the seepage length is between 0 and 100 m, as shown by Figure 5.5. To reduce computational demand, the seepage length is not randomly sampled, but rather 10 evenly distributed samples between 0 and 100 m ($L = 5, 15, ... 95$ m) are chosen.

The parameter bounds for the aquifer hydraulic conductivity are derived from representative values for sand and gravel as proposed by Domenico & Schwartz (1990). This range is chosen to include the representative hydraulic conductivity for both fine sand (lower bound) and gravel (upper bound). This means that the hydraulic conductivity of sand types ranging from fine sand to gravel is taken into account.

However, parameter values of the hydraulic conductivity should not be chosen from a uniform distribution, because in reality, hydraulic conductivity is log-normally distributed. The log-normal distribution and the change in the order of magnitude within the value range, cause the probability of occurrence of a value in a random sample to become lower the further away this value is from the mean. In Figure 5.6a is demonstrated that the probability is the largest near the mean of the log-normal distribution (orange area). Therefore, hydraulic conductivity is converted to the uniformly distributed exponent x with Equation 5.1, for which the distribution bounds are also given in Table 5.1. Once the random sample of x is created, the corresponding random hydraulic conductivity values can be backtracked from 10^x.

$$\log(K_a) = x \Leftrightarrow K_a = 10^x \tag{5.1}$$
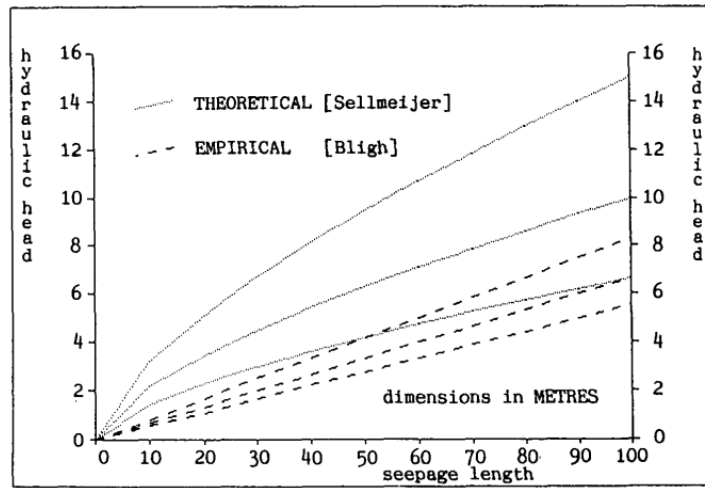
Figure 5.5: Comparison between results Sellmeijer and Bligh (Sellmeijer, 1988)

The distribution bounds of d_{70} are set with the intention of expanding the applicability range that was used in the calibration of the revised Sellmeijer design rule (2021) (150 μm $\leq d_{70} \leq$, 430 μm, see Table 2.2) and to include the grain sizes found at the research locations in Limburg. Therefore, the upper bound is set to 900 μm, which is the maximum d_{70} found in Buggenum. The lower bound of the d_{70} distribution is set slightly lower than for the calibration of the revised Sellmeijer design rule (2021).

As stated above, the true height of the pipe is unknown. Several hypotheses can be found in the literature, but no definitive answer has yet been provided. As a result, the distribution bounds of the number of grains in Table 5.1 are set to include small pipes of 3 grains and large pipes of 100 grains.

5.3. Generating a random sample

A statistical method known as Latin Hypercube Sampling (LHS) (Olsson et al., 2003) is used to generate a random sample of model parameter values from the distribution bounds shown in Table 5.1. Figure 5.6c demonstrates an example of two-dimensional (2D) LHS. The sample spaces are equally divided into a number of areas equal to the desired number of sampling points (n). Then for each row and column one sample is drawn from within the divided areas.

The advantage of LHS over ordinary random sampling is that the generated samples are evenly distributed over the sampling spaces. For ordinary random sampling, there is the possibility that the samples are drawn very close to each other with little parameter variation (see Figure 5.6b). LHS enables that the chosen values of the model parameters of Section 5.2 are evenly distributed over the uniform distribution of the parameters.

(a) Log-normal/uniform   **(b)** Uniform/uniform   **(c)** 2D Latin Hypercube Sampling, n=6
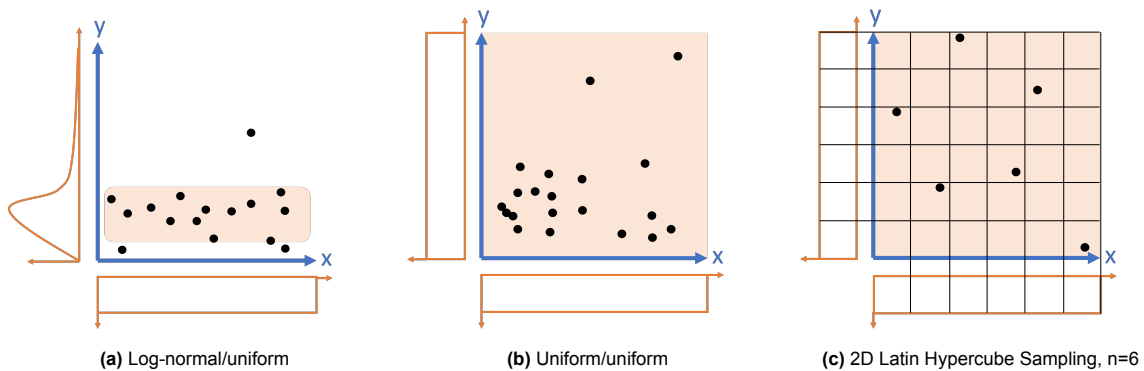
Figure 5.6: Random sampling examples; based on (Olsson et al., 2003)

Table 5.2 displays the data from the random sample generated with multidimensional LHS for 1000 sample points or observations. The quality of the random sample can be checked with the mean and the coefficient of variation of the sampled parameter values. For each parameter, it is demonstrated in Table 5.2 that the mean is approximately the average of the parameter application range. This indicates that the LHS method has generated an evenly distributed sample over the parameter distributions of Table 5.1.

The coefficient of variation expresses a parameter's degree of uncertainty. The column in Table 5.2 displays correctly that the hydraulic conductivity sample is the most uncertain. The reason for this is that the parameter application range in Table 5.1 includes the hydraulic conductivity for relatively poorly permeable sand until highly permeable gravel. The coefficient of variation for d_{70} and the number of grains is in the expected order for soil characteristics.

Table 5.2: Quality check of the random sampled values of the model parameters

Parameter	Unit	Obs	Mean	Std. Dev.	COV [-]	Min	Max
Water level, W	[m]	1000	8.5	4.33	0.57	1.00	15.99
Hydraulic conductivity, K	[m/s]	1000	$7.14 \cdot 10^{-4}$	$7.96 \cdot 10^{-4}$	1.12	$3.99 \cdot 10^{-5}$	$3.16 \cdot 10^{-3}$
Grain size, $d_{70,\text{stoc}}$	[m]	1000	$5.00 \cdot 10^{-4}$	$2.31 \cdot 10^{-4}$	0.46	$1.01 \cdot 10^{-4}$	$8.99 \cdot 10^{-4}$
Number of grains, $n_{g,stoc}$	[-]	1000	51.51	28.00	0.54	3	100

5.4. Scenario analysis

A piping scenario is a unique combination of model parameters from the random sample implemented the FEM numerical model, that represents a possible dike cross-section where piping could occur. In this manner, 1000 distinct piping scenarios are generated from the random sample and assessed on the occurrence of piping. The piping scenarios are unique due to the nature of the random sample generated by Latin Hypercube Sampling, as explained in Section 5.3. The scenarios that resulted in piping progression according to the 2 forces equilibrium (see Section 3.1.2) and contain a realistic pipe height ($3 \leq n_g \leq 60$) are selected and used in the evaluation of the Sellmeijer design rule.
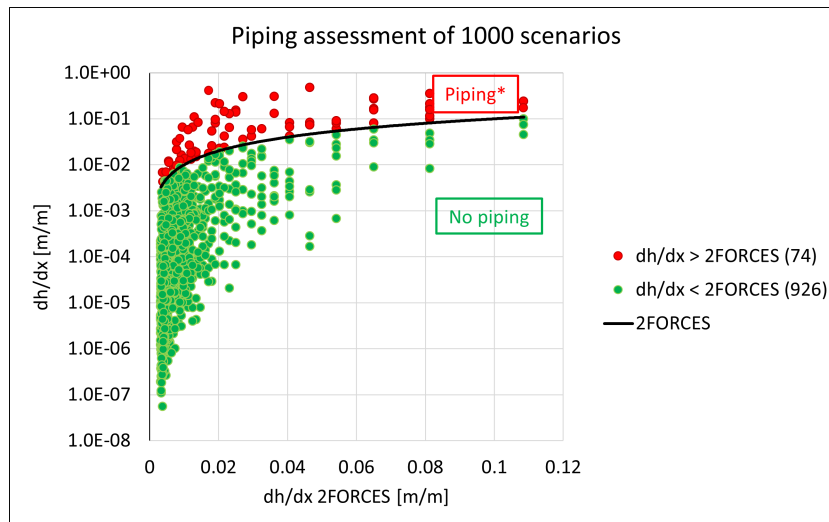
Figure 5.7: Scenarios that result in piping (or not) according to the 2 forces equilibrium for a pipe length equal to 44% of the dike width; *piping remains conditional to pipe geometry

The piping assessment for the scenarios is similar to previously described assessments for pipes with a pipe length equal to 44% of the dike width (0.44L) (see Sections 3.1 and 4.2): piping occurs if the local hydraulic gradient inside the pipe exceeds the critical 2 forces gradient (see Section 3.1.2). Figure 5.7 displays the piping assessment for every unique scenario. The 926 green markers in Figure 5.7 represent all scenarios in which the hydraulic gradient inside the pipe does not exceed the 2 forces gradient (black line in Figure 5.7), which implies that piping does not occur for the specific combination of model

parameters of that scenario. The red markers represent the 74 out of 1000 scenarios in which piping occurs, because the average hydraulic gradient in the pipe exceeds the critical 2 forces gradient.

The hydraulic gradient and the 2 forces gradient are unique for each piping scenario and depend on the pipe height, which is a function of the number of grains and d_{70}. Therefore it must be analyzed whether the 74 scenarios in which piping occurs contain a realistic pipe height for the equilibrium condition ($a_{eq}[m]$, see Equation 5.2), corresponding to the smallest hydraulic gradient required for piping to occur in that particular dike geometry.

The number of grains ($n_{g,eq}$ [-]) and $d_{70,\text{eq}}$ corresponding to the equilibrium condition, are used to identify whether the pipe height is realistic. To quantify, criteria are set stating the number of grains must be between 3 and 60 grains and the $d_{70,\text{eq}}$ must be greater than 0.15 mm. The criterion of the number of grains is based on the proposed criterion of Van Esch et al. (2013), which states that for real dikes a realistic pipe height consists of 3 to 30 grains. In this thesis, the number of grains criterion of Van Esch et al. (2013) is expanded to include scenarios with larger pipe heights, but is limited to 60 grains to rule out unrealistic pipe heights. The criterion of the $d_{70,\text{eq}}$ is set to include only real grain diameters and is based on the lowest parameter application bound of the revised Sellmeijer design rule (2021) (see Table 2.2). However, this criterion does not rule out any scenarios.

The number of grains corresponding to the equilibrium condition, is found by solving the local hydraulic gradient inside the pipe ($\frac{dh}{dx_{stoc}}$ [m/m]), of the 74 selected scenarios, for the 2 forces equilibrium (see Equation 5.3 and Section 3.1.2).

$$a_{eq} = n_{g,eq} \cdot d_{70,\text{eq}} \tag{5.2}$$

$$\frac{dh}{dx_{stoc}} = \frac{\pi}{3} \frac{\gamma_{sp}}{\gamma_w} \frac{d_{70,\text{eq}} \eta \tan(\theta)}{a_{eq}} = \frac{\pi}{3} \frac{\gamma_{sp}}{\gamma_w} \frac{\eta \tan(\theta)}{n_{g,eq}} \tag{5.3}$$

$$d_{70,\text{eq}} = \frac{a_{stoc}}{n_{g,eq}} = \frac{n_{g,stoc} \cdot d_{70,\text{stoc}}}{n_{g,eq}} \tag{5.4}$$

Subsequently, the $d_{70,\text{eq}}$ corresponding to the equilibrium condition is found by dividing the stochastically implemented pipe height (a_{stoc} [m]) by the number of grains corresponding to the equilibrium condition (see Equation 5.4).
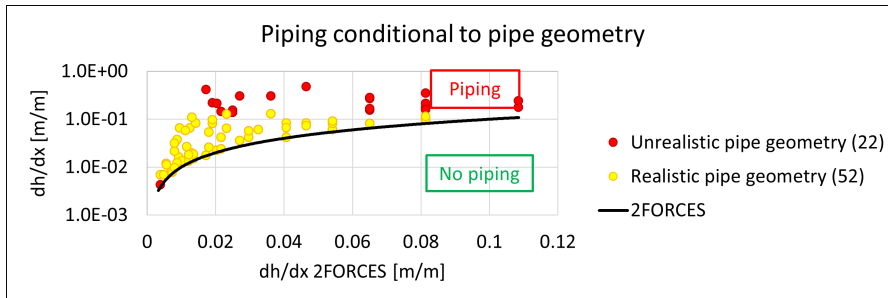
Figure 5.8: Selected piping scenarios conditional to pipe geometry with a pipe length equal to 44% of the dike width

52 of the 74 scenarios in which piping occurs have a realistic pipe height ($3 \leq n_g \leq 60$) for the equilibrium condition. The 74 scenarios in which the hydraulic gradient in the pipe is greater than the 2 forces gradient (black line) are displayed in Figure 5.8. The yellow markers, on the other hand, represent the 52 scenarios with a realistic pipe height. These scenarios are called failure scenarios.

5.5. Evaluation of the Sellmeijer design rule
The original Sellmeijer design rule with the new geometry factor (1988/2011) as displayed in Section 4.1 is evaluated with the 52 failure scenarios in which piping occurs for a realistic pipe geometry (yellow markers in Figure 5.8), as explained prior. Essentially, the design rule is evaluated by comparing the Sellmeijer scale factor, determined with the stochastically implemented $d_{70,\text{stoc}}$ from Table 5.2, that

follows directly from the failure scenarios ($F_{\text{S,stoc}}$ [-]) and the scale factor determined with the $d_{70,\text{eq}}$ corresponding to the equilibrium condition of the 52 failure scenarios ($F_{\text{S,eq}}$ [-]) (see Equation 5.5). The permeability (κ [m^2]) and seepage length (L [m]) are equal in both formulas of Equation 5.5 and correspond to the observed failure scenario.

$$F_{\text{S,stoc}} = \frac{d_{70,\text{stoc}}}{\sqrt[3]{\kappa L}} \qquad\qquad F_{\text{S,eq}} = \frac{d_{70,\text{eq}}}{\sqrt[3]{\kappa L}} \tag{5.5}$$
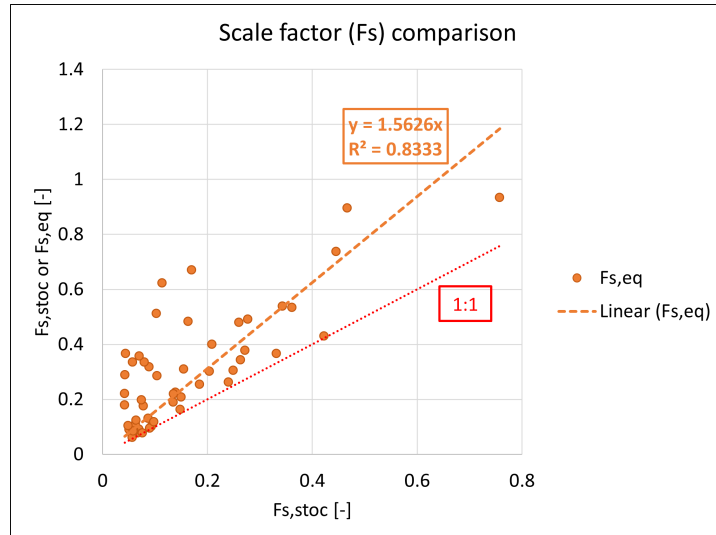
Figure 5.9: Linear regression of the scale factor comparison

The comparison of the two scale factors is demonstrated in Figure 5.9. The red 1:1 line represent the stochastically determined scale factor ($F_{\text{S,stoc}}$), since the vertical and horizontal axis both represent $F_{\text{S,stoc}}$. The orange markers represent the scale factor corresponding to the equilibrium condition of the scenarios ($F_{\text{S,eq}}$), for which the values are plotted against $F_{\text{S,eq}}$ on the vertical axis and $F_{\text{S,stoc}}$ on the horizontal axis.

A line is fitted through the data points of the scale factor corresponding to the equilibrium condition of the failure scenarios using a linear regression (see Figure 5.9, providing a linear relationship between $F_{\text{S,stoc}}$ and $F_{\text{S,eq}}$. The linear regression is characterized by the coefficient of determination (R^2) and the regression equation. R^2 is a goodness-of-fit measure, that tells how much variation in $F_{\text{S,eq}}$ can be reduced by taking $F_{\text{S,stoc}}$ into account. The regression has a coefficient of 0.83, meaning that the variation of $F_{\text{S,eq}}$ is reduced by 83%, when taking $F_{\text{S,stoc}}$ into account.

The function corresponding to the linear regression of $F_{\text{S,eq}}$ has a slope value of 1.5626. Since the vertical axis represents $F_{\text{S,eq}}$ and the horizontal axis represents $F_{\text{S,stoc}}$, the function of the scale factor corresponding to the equilibrium condition of the failure scenarios can be rewritten as:

$$y = 1.5626x \Rightarrow F_{\text{S,eq}} = 1.5626 F_{\text{S,stoc}} \tag{5.6}$$

This implies that the scale factor of the original Sellmeijer design rule with the new geometry factor (1988/2011) as displayed in Section 4.1 can be applied on dike cross-sections in Limburg with an additional factor of 1.56. Equation 5.7 may also be applied on other dike cross-section for which the revised Sellmeijer design rule 2021 is not applicable and the values of the dike parameters fall in between the proposed bounds of the parameter distributions displayed in Table 5.1. The original Sellmeijer design rule with the new geometry factor (1988/2011) and the correction of the scale parameter becomes:

$$\frac{H_{\text{c,o}}}{L} = F_{\text{R}} 1.56 F_{\text{S,o}} F_{\text{G}} \tag{5.7}$$

<div style="text-align: right; font-size: 4em;">6</div>

Discussion

The FEM numerical model and the results of Chapters 4 and 5 are interpreted in this chapter. Before analyzing the results, the complications and flaws of the proposed numerical model are discussed. The order of this chapter must aid in contextualizing the results of Chapters 4 and 5.

6.1. Model imperfections

The primary objective of numerical modelling is to accurately simulate physical processes. However, reality is far too complex to be fully represented in the models. As a result, the numerical model is only an idealized schematization of reality. Evaluating the model imperfections leads to a better understanding of the model results.

Soil heterogeneity

The geometry of the cross-sectional models consists of a multiple-layer system and the layers are schematized with a constant depth. Each subsoil layer has site-specific soil characteristics. However, these characteristics are assumed to be constant for the entire layer, implying that the soil properties are assumed to be homogeneous for each individual layer. These assumptions make it impossible to account for soil heterogeneity. Groundwater flow, for example, can be obstructed by a boulder or an underlying clay layer that is not represented in the model. As a result, the flow patterns in the model and reality differ.

Foreland length, hinterland length and aquifer depth effect

The analyses in Section 3.3.6 and Section 5.1 demonstrate the effect that a varying aquifer depth, foreland length and hinterland length have on the hydraulic gradient in the pipe. It is concluded that the aquifer depth effect reaches an optimum at approximately 10 m total aquifer depth. The foreland and hinterland length analysis shows that as total model length (sum of foreland and hinterland length) increases, the hydraulic gradient in the pipe decreases.

Rijkswaterstaat (2021) recommends using long foreland and hinterland lengths, resulting in a low hydraulic gradient for the research locations Well, Thorn and Hout-Blerick. Using shorter model lengths (Buggenum) results in relatively higher hydraulic gradients, but above all, a remarkable change is observed in the Reynolds number for flow inside the pipe. For the cross-sectional model of Buggenum, the flow in the pipe approaches a turbulent flow regime. The analysis in Appendix E shows that the Reynolds number increases for shorter model lengths.

Because model parameters are examined individually, the combined effect of aquifer depth and total model length on the hydraulic gradient inside the pipe is not considered. However, it appears that the effect of the two geometry parameters on the hydraulic gradient inside the pipe is correlated. The correlation between aquifer depth and model length and its effect on the hydraulic gradient and the flow regime inside the pipe are not further elaborated in this thesis.

Schematization of the pipe geometry

The schematization of the average pipe cross-section geometry remains a source of uncertainty in the model geometry. Especially, the choice for a fracture flow method cross-section is disputed by Aguilar-López et al. (2016a), who reasons that parallel plates should not be applied in numerical modelling and proposes a circular cross-section. Aguilar-López et al. (2016a) also demonstrates that using a fracture flow cross-section leads to a lower hydraulic gradient inside the pipe than when using a circular pipe cross-section. However, Bersan et al. (2013); Sellmeijer (1988) argue without comparing it to the 2 forces equilibrium that it is possible to use the fracture flow method for the pipe cross-section.

The piping assessment results of the proposed numerical model are also conditional to the applied pipe height or number of grains that make up the pipe height in the model. This approach is chosen because it remains unknown what the true average pipe height is for a developing pipe under the dike. Van Esch et al. (2013) reports that the pipe height varies for small-scale experiments between 0 and 3 grains, for field experiments between 0 and 10 grains and between 0 and 30 grains for a real dike. However, the pipe height must be larger than 1 grain, for a grain to pass through the pipe and 3 grains allows to have at least one grain sticking out from the side. Therefore an absolute minimum pipe height of 3 grains is assumed throughout this thesis. This pipe height criterion is used to analyse the randomly generated pipe heights in the stochastic analysis in Chapter 5, in order select the random samples with a realistic pipe height for the stochastic evaluation of the Sellmeijer design rule (yellow markers in Figure 5.8).

Time dependency

The proposed numerical model is designed for a steady-state condition in which an equilibrium is reached, implying that the model ignores the time dependency of piping. According to Pol et al. (2019), time-dependent loading conditions influence pipe development. For example, the period of time that an extreme outside water level exists can influence the development of the pipe. Furthermore, the rate at which the outside water level rises or falls influences groundwater flow in the aquifer.

Two- and three-dimensional groundwater flow

When working with a two-dimensional groundwater flow model, water or fluxes can only leave the model geometry at the predefined horizontal or vertical model boundaries of the model domain. Groundwater flow, on the other hand, is a three-dimensional problem. Hydraulic head losses or increases caused by groundwater flow perpendicular to the dike cross-section cannot be registered in the proposed model, resulting in an underestimation or overestimation of the hydraulic head (gradient) in the model.

Another disadvantage of using a two-dimensional groundwater flow model is that water or fluxes can only enter the pipe through the lower boundary, whereas in reality (if the fracture flow assumption is not applied), water can also enter the pipe through the vertical side walls.

Hagen-Poiseuille flow

The Hagen-Poiseuille flow assumption is combined with Darcy's Law to derive the function for the pipe's fictitious permeability. One-dimensional laminar and incompressible flow through a long pipe with a constant cross-section is described by Hagen-Poiseuille flow. The presence of a laminar flow regime inside the pipe is demonstrated by the cross-sectional models of Well, Hout-Blerick, and Thorn. The Buggenum cross-sectional model, on the other hand, demonstrates turbulent flow inside the pipe, which contradicts the condition of Hagen-Poiseuille flow.

Another requirement for using Hagen-Poiseuille flow is a no-slip condition along the sides of the pipe as well as mass conservation between the tip of the pipe and the sandboil. However, water enters the pipe through the bottom of the pipe between the tip and the sand boil in the FEM model. This implies that using the Hagen-Poiseuille flow assumption is fundamentally incorrect.

Calibration

Calibration in Section 3.4 did not succeed for the cross-sectional models of Well and Hout-Blerick because the calibration errors exceeded the maximum criterion (10% of the measurement range). The calibration errors could not be reduced due to time constraints and model imperfections (overly permeable and two-dimensional groundwater flow). When interpreting the results of the Well and Hout-Blerick cross-sectional models, the consequences of calibration must be considered. The hydraulic gradient inside the pipe is most likely overestimated in the cross-sectional model of Well, resulting in a more

conservative piping assessment. Whereas, the cross-sectional model of Hout-Blerick underestimates the hydraulic gradient in the pipe.

Before the calibration of Thorn's cross-sectional model, it was discovered that groundwater flows in the opposite direction than necessary for piping. Hydraulic head measurement data from standpipes and pore pressure gauges of the flood event in July 2021, show that groundwater flows in the direction of the foreland, the Maas, and lake the Grote Hegge. As a result, the cross-sectional model of Thorn could not be calibrated and it can be concluded that piping did not occur during the flood event.

An elaborate discussion of the calibration result is included in Section 3.4.

6.2. Analysis of the results

Before delving into the FEM model results, it is important to note that they should not be interpreted as a general piping assessment for the province of Limburg, as the assessment is limited to four dike sections provided by Waterschap Limburg. Even when applying the results to the corresponding research locations, keep in mind that the results only apply to the dike geometry schematizations implemented in the proposed numerical model.

Thorn
Despite the fact that the Thorn cross-sectional model could not be calibrated due to the opposite direction of seepage flow than required for piping, the Thorn piping assessment is carried out in the same manner as the other research locations (see Section 4.2). Because the direction of seepage flow could in an extreme case be reversed, if the groundwater level in the hinterland is lowered in combination with extremely high outside water levels.

The piping assessment for Thorn is performed as if the groundwater flow beneath the dike in the direction of the hinterland. The critical heads derived with the Sellmeijer design rules can give an indication of the global gradient required for piping in case the direction of groundwater flow is reversed.

Results of the analytical piping assessment using the Sellmeijer design rules (Section 4.1)
Section 4.1 demonstrates an analytical piping assessment according to the original Sellmeijer design rule with the new geometry factor (1988/2011) and revised Sellmeijer design rule (2021). The determined critical heads for both design rules are summarized per research location in Table 4.1. This table also contains the height of the dike crest and the multiplication of critical heads by a factor of 1.8 because this version of the Sellmeijer design rule is used in Limburg (Waterschap Limburg, 2020).

The estimated critical head of the original Sellmeijer design rule (1988/2011) multiplied by 1.8 ($1.8H_{c,o}$) exceeds the actual crest level at all four research locations. For the research locations Well and Buggenum, the actual crest level is also exceeded by the critical head estimated by using the original Sellmeijer design rule (1988/2011, $H_{c,o}$) and the revised Sellmeijer design rule (2021) multiplied by 1.8 ($1.8H_{c,rev}$). This is probably due to the applied d_{70} of Well ($d_{70} = 660$ μm) and Buggenum ($d_{70} = 900$ μm), which exceed the Sellmeijer (2021) d_{70} application range (150 μm $\leq d_{70} \leq 430$ μm).

On the contrary, for Thorn and Hout-Blerick, the critical heads ($H_{c,o}$ and $1.8H_{c,rev}$) remain below the crest height, but their d_{70} are only just outside the bound (Thorn $d_{70} = 460$ μm, Hout-Blerick $d_{70} = 500$ μm).

Despite that the determined critical heads that exceed the crest height, can never occur as an outside water level against the dike, the results might hold some core of truth. The water level during the flood event was almost equal to the crest level of the dikes, but piping was not observed. This implies that the piping equilibrium limit state has not yet been exceeded, so the critical head must be greater than the crest height. It must be kept in mind that the estimated global gradient (corresponding to the critical head exceeding the crest level) may be plausible for an extreme case with a lower groundwater level in the hinterland.

The critical head derived with the revised Sellmeijer design rule (2021, $H_{c,rev}$) remains for every research location below the crest height, but this proves to be conservative.

The critical heads in Table 4.1 also revealed that the results of the original Sellmeijer design rule (1988/2011, $H_{c,o}$) and the revised Sellmeijer design rule (2021) multiplied by 1.8 ($1.8H_{c,rev}$) are very

similar.

Results of the deterministic piping assessment using the FEM numerical model (Section 4.2)
Section 4.2 contains the piping assessment results from the proposed numerical models. The critical heads and the crest height from Table 4.1 are implemented as outside water level at each research location.

No outside water level equal to the crest level induces a hydraulic gradient inside the pipe that exceeds the critical gradient corresponding to grain stability in any of the research locations. In reality, an outside water level equal to the crest level is the highest water level that can stand against the dike before other dike failure mechanisms play a role. This means that the schematized dike cross-sections of the research locations are not susceptible to piping, according to the proposed model. However, keep in mind that the Sellmeijer design rules provide the global gradient, which means that lowering the groundwater level in the hinterland raises the hydraulic gradient for a water level equal to the crest level. If the groundwater level is sufficiently lowered, piping can occur.

Furthermore, none of the critical heads (from Table 4.1) determined using the original (1988/2011) or revised Sellmeijer design rule (2021) result in a hydraulic gradient greater than the critical gradient for a realistic pipe height.

The critical head of the original Sellmeijer design rule (1988/2011) multiplied by 1.8 ($1.8H_{c,o}$) serves as the highest outside water level for each research location. This water level causes a hydraulic gradient greater than the critical gradient for a pipe height of 1 to 2 grains and a pipe length of 10% of the dike width in Well and Hout-Blerick. Because the pipe height is not considered realistic according to the set pipe height criterion ($3 \leq n_g \leq 60$), the pipe cannot grow beyond 10% of the dike width. According to the proposed models, piping cannot occur at Well or Hout-Blerick.

For the research location Buggenum, the highest critical head of Table 4.1 ($1.8H_{c,o}$) results in a hydraulic gradient that exceeds the critical gradient in the pipe for a pipe height of 3.4 grains combined with a pipe length equal to 10% of the dike width and for a pipe height of 4.5 grains combined with a pipe length equal to 44% of the dike width. This implies, theoretically, that piping can occur for very small pipe heights combined with the critical head of the original Sellmeijer design rule (1988/2011) multiplied by 1.8. However, because this critical head exceeds the crest level, it cannot occur in reality. The global gradient, which corresponds to this critical head and implemented groundwater level, could occur in the case of a realistic water level and a lower groundwater level, which could lead to piping. Van Esch et al. (2013); Aguilar-López et al. (2016a) argue that a realistic pipe height is in the order of 10 to 30 grains and, therefore, deem the observed pipe height in Buggenum too small.

According to the results of Buggenum's cross-sectional model, model geometries with a shorter foreland or total model length simulate a higher hydraulic gradient inside the pipe. A shorter model length appears to result in higher Reynolds numbers, implying that the flow in the pipe is approaching a turbulent flow regime. Appendix E demonstrates that the Reynolds number increases with shorter foreland lengths. However, the exact relationship between the Reynolds number and the model geometry length, on the other hand, is unknown.

Results of the stochastic evaluation of the Sellmeijer design rule (Chapter 5)
The original Sellmeijer design rule with the new geometry factor (1988/2011) has been stochastically evaluated using the FEM numerical model proposed in Chapter 5. The Sellmeijer scale factor (F_s) is used to find the correction factor that allows to apply the Sellmeijer design rule to a broader application range, because the difference between the original Sellmeijer design rule with the new geometry factor (1988/2011) and the revised Sellmeijer design rule (2021), is found in the scale factor.

By comparing the Sellmeijer scale factor of the 52 stochastically generated piping scenarios ($F_{S,stoc}$) and the scale factor corresponding to the equilibrium condition ($F_{S,eq}$), a factor 1.56 difference is found in between the two scale factors (see Section 5.5):

$$F_{S,eq} = 1.56F_{S,stoc}$$

This means that the scale factor for the new application ranges (100 μm $\leq d_{70} \leq$ 900 μm, see other model parameters in Table 5.1) is 1.56 times larger than the scale factor of the original Sellmeijer

design rule (1988/2011), which corresponds to the equilibrium condition. As a result, the original Sellmeijer design rule with the new geometry factor (1988/2011) can be applied with a factor 1.56 to dike cross-sections for which the revised Sellmeijer design rule (2021) is not applicable and the parameters correspond to the new application ranges of Table 5.1.

$$\frac{H_{c,o}}{L} = 1.56 F_{S,o} F_G F_R$$

Based on the findings of Van Beek (2019), Waterschap Limburg has adopted a factor 1.8 in the piping assessment for dike cross-sections with gravel layers. This factor appears to be similar, to the factor 1.56 found in Section 5.5. However, the factor of 1.8 is used to correct the determined critical head using the revised Sellmeijer design rule (2021) when a gravel layer is present directly beneath the cover layer. The correction factor 1.56 is derived to allow the original Sellmeijer design rule to be applied at dike cross-sections with coarse sand layers beneath the cover layer, for which the d_{70} lies outside the application ranges of the revised Sellmeijer design rule (150 μm $\leq d_{70} \leq$ 430 μm), but within the newly sets bounds of the stochastic analysis in Table 5.1 (see Chapter 5).

Sellmeijer design rule
The applicability of the Sellmeijer conceptual model and the derived design rules should be assessed apart from each other. The theory of the Sellmeijer conceptual model describes the processes that contribute to piping exceptionally well.

However, Sellmeijer (1988) argues that "such a theoretical study however has value if and only if it serves practical interests" (Sellmeijer, 1988). Therefore, (Sellmeijer, 1988) derives the original Sellmeijer design rule from the conceptual model theory to provide a practical design rule for engineers. However, the exponents of the design rule are biased for the parameter values of the experiments that Sellmeijer (1988) used to derive the design rule. Similarly, the revised Sellmeijer design rule (2021) is only valid to apply within the parameters bounds that were used in the experiments to calibrate the new design rules.

7

Conclusion and recommendations

This chapter concludes this thesis by answering the proposed research questions and the objective of the thesis. Following, several recommendations for further research are discussed.

Conclusion

The objective of this thesis is to assess the applicability of the Sellmeijer design rule in the northern Maasvallei in Limburg and make an improved estimation of piping. The conclusions corresponding to the objective are:

- According to the numerical model proposed in this thesis, conditionally to the pipe height, piping does not occur at the research locations Well, Hout-Blerick and Thorn.
- Piping is theoretically possible at Buggenum for a pipe with a pipe height of less than 3.4 grains and a very extreme global hydraulic gradient, according to the numerical model. It is, however, highly unlikely.
- The revised Sellmeijer design rule (2021) gives conservative results for dike sections in Limburg.
- The original Sellmeijer design rule with the new geometry factor (1988/2011) gives similar critical heads as the revised Sellmeijer design rule (2021) multiplied by 1.8.
- At dike sections where the revised Sellmeijer design rule (2021) is not applicable, piping can be assessed with the original Sellmeijer design rule with the new geometry factor (1988/2011) multiplied by 1.56.

What are the primary reasons why the Sellmeijer design rule may not apply to Limburg dikes?
The Sellmeijer model is a conceptual model proposed by Sellmeijer (1988) original that covers three piping processes: groundwater flow beneath the dike in the subsoil, flow through the pipe, and grain stability of sand particles at the pipe's bottom. The conceptual model is designed for a simple dike geometry that consists of a fully impermeable dike with a horizontal bottom resting on a permeable homogeneous sandy aquifer with a limited constant thickness. Furthermore, the particle diameter d_{70} is implemented in the model because Sellmeijer (1988) suggests that larger particles define the limit state equilibrium because smaller particles are quickly eroded away.

The original Sellmeijer design rule (1988) was calibrated to a series of small and medium-scaled experimental tests in 2011 (Sellmeijer et al., 2011). However, the revised Sellmeijer design rule (2021) is only applicable to the parameter ranges used in the experiments and the applied model. The most restrictive model parameter range is d_{70}, with a minimum of 150 μm and a maximum of 430 μm (Sellmeijer et al., 2011). The experimental setup of Sellmeijer et al. (2011) is similar to the conceptual model of Sellmeijer (1988), consisting of a single homogeneous sandy aquifer with limited depth.

The composition of a dike cross-section in Limburg differs from the dike configuration used in the Sellmeijer model (Sellmeijer, 1988) in several ways. To begin, Limburg's subsoil is a multi-layered system composed of various types of soil material. Because each layer influences the hydrogeological system

differently, this layer system cannot be simplified to a single aquifer, as proposed by the Sellmeijer model. Furthermore, because natural soil characteristics are generally heterogeneous, homogeneous soil characteristics are a simplified schematization assumption. Permeability and representative grain size are not constant, especially when the soil characteristics of a layer are examined at different locations. Furthermore, a dike cross-section in Limburg may have a less permeable or impermeable clay cover layer resting on top of the aquifer. The cover layer induces a resistance to piping that is not accounted for in the Sellmeijer model.

Furthermore, the applicability of the revised Sellmeijer design rule (2021) in Limburg is also questioned, because on several locations in Limburg, the subsoil composition consists of coarse sand layers and/or gravel layers, for which d_{70} exceeds the parameter application range (150 μm $\leq d_{70} \leq$ 430 μm) of the revised Sellmeijer design rule (2021). Van Beek (2019) concludes that the coarse sand particles in Limburg induce resistance, allowing the critical heads determined by the revised Sellmeijer design rule (2021) to be corrected by a factor of 1.8.

How can piping in Limburg hydrogeological systems be modeled?

A finite element (FEM) numerical model is used to model backward erosion piping. Building a numerical model to assess piping on a predefined research location requires several processes, including assembling the model groundwater and piping principles, schematizing the dike geometry of the research location, and calibrating the site-specific characteristics in the model.

Some model principles of the FEM numerical model are chosen similarly to the Sellmeijer model in order to compare them. Following that, the proposed model is two-dimensional, neglecting three-dimensional groundwater flow. Furthermore, the model is assumed to be in a steady state, which means that the time-dependency of piping is ignored.

The piping limit state equilibrium is defined by the horizontal hydraulic gradient acting on the grains at the bottom of the pipe and the critical gradient corresponding to grain stability. The hydraulic gradient in the pipe is affected by the groundwater flow through the pipe. The flow in the pipe is described using the Hagen-Poiseuille's flow equation for long tubes with a constant cross-section. Darcy's law, on the other hand, is used to simulate flow through the aquifer.

The assessment of the hydraulic gradient and the Hagen-Poiseuille flow equation requires making assumptions for the implementation of the pipe geometry (cross-section, length and height) in the model. Because the model is two-dimensional, the pipe cross-section is not directly implemented in the geometry, but the shape of the cross-section determines the fictitious permeability of the pipe. For the pipe cross-section, the fracture flow method is used. Because the true pipe height is unknown, the piping assessment is performed iteratively for multiple pipe heights.

The proposed model requires a schematization of the dike geometry at the research locations in Limburg. Four consistent cross-sectional models are proposed using general schematization decisions. The soil layering system and soil characteristics are studied for each research location in order to understand the local hydrogeological system and build a well-substantiated model geometry. The foreland and hinterland lengths are also important model geometry parameters that must be defined. The implemented hinterland length is equal to 3 times the leakage length of the dike cross-section. The foreland length is equal to the leakage length or the distance to the nearest outside water body. The shortest of the two lengths is implemented as foreland length in the model geometry. Once all required model parameters have been defined, the model geometries are calibrated using hydraulic head field measurement data from standpipes and pore pressure gauges at the research locations.

What are the differences in the results of the safety assessment between the Sellmeijer conceptual model and the finite element model?

The Sellmeijer design rule determines the global hydraulic head gradient across the dike because the main output of the design rule is the critical head for a dike cross-section or the critical seepage length for a given head.

For seepage length, d_{70}, aquifer permeability, and aquifer depth, the Sellmeijer design rule requires site-specific input values. Because the Sellmeijer model geometry is limited in comparison to actual dike geometries, schematization choices must be made in order to include all required site characteristics in the Sellmeijer design rule. These schematization choices have an impact on the quality

of the design rule's output. Because the Sellmeijer model does not include a multi-layer system, the aquifer permeability of all relevant layers must be calculated as a weighted average. Similarly, the input aquifer thickness is the sum of the thickness of the relevant layers. However, the value of the d_{70} of the aquifer layer in which the pipe develops cannot be assumed to be different from what was found at the research locations. If the research location's d_{70} falls outside the parameter application ranges of the Sellmeijer design rule, the original (1988/2011) and revised Sellmeijer design rule (2021) results become inaccurate, irrelevant, or conservative.

The proposed numerical model is a groundwater model for a dike cross-section containing a pipe with a pipe length equal to 10% or 44% of the dike width. The model examines groundwater flow (or fluxes) through any required subsoil system and conducts analyses at any desired location or depth within the model geometry. Similarly, it can examine the flow (velocity) and pressure throughout the pipe and calculate the average hydraulic gradient along its length. The hydraulic gradient corresponding to head differences in the pipe itself is known as the local gradient, and it is the proposed numerical model's main output.

Afterwards, the derived local gradient is compared to the critical gradient corresponding to the limit state equilibrium of the stability of the grains at the bottom of the pipe. Exceeding the critical gradient means that the grains at the bottom of the pipe can be set in motion so erosion can occur for the examined pipe geometry configuration. The local gradient must always be considered conditional to pipe height and pipe length. The result of the proposed deterministic model are therefore always conditional to the examined configuration of the pipe geometry.

In conclusion, the main difference between a piping assessment performed with the Sellmeijer design rule and the proposed numerical model is found in the result. The Sellmeijer design rules provide a critical head for a given seepage length and vice versa. However, the proposed numerical model can predict the critical head or seepage length for which piping occurs with the corresponding pipe height.

When Limburg parameter values are included in the design rule calibration using the finite element model, how does the Sellmeijer design rule change?
When the original Sellmeijer design rule (1988/2011) is re-calibrated for broader parameter application ranges, the scale factor (F_S) increases by a factor of 1.56 and the original Sellmeijer design rule with the new geometry factor (1988/2011) now becomes:

$$\frac{H_{c,o}}{L} = 1.56 F_{S,o} F_G F_R$$

This design rule can be applied to dike cross-section where the revised Sellmeijer design rule (2021) is not applicable, but the parameters fall in the newly set parameter application ranges of Table 5.1, which include the parameter values found at the research locations in Limburg. For example, the broadened parameter application range of the d_{70} is equal to 100 μm $\leq d_{70} \leq$ 900 μm.

Before calibrating the scale factor, the proposed FEM numerical model was used to assess 1000 unique randomly generated dike cross-sections on piping. Each random dike cross-section is made up of an unique set of randomly sampled model parameters. The model parameters are sampled from carefully defined parameter ranges using Latin Hypercube Sampling (Olsson et al., 2003), making sure that the values of the samples are unique and evenly distributed across the parameter ranges. To ensure that the probability of occurrence for each parameter value is equal and thus minimize probabilistic bias, all parameter ranges are uniform distributions. The limits of the uniform distributions are carefully set, to broaden the application range of the revised Sellmeijer design rule (2021) and to include the parameter values found at the research locations in Limburg (see Table 5.1).

52 out of 1000 randomly generated dike cross-section demonstrate piping for a realistic pipe height ($3 \leq n_g \leq 60$), these cross-section are called failure scenarios. The stochastically generated scale factor ($F_{S,stoc}$) and the scale factor corresponding to the failure scenario's equilibrium condition ($F_{S,eq}$) are compared for each failure scenario. Using a linear regression, it is demonstrated that the scale factor corresponding to the equilibrium condition ($F_{S,eq}$) is 1.56 times greater than the stochastically generated scale factor ($F_{S,stoc}$).

Recommendations

In Chapter 6 the imperfections of the proposed FEM numerical model are discussed. These imperfections form the foundation of the recommendations for further research.

Model geometry effects

The groundwater flow in the pipe is influenced by the model geometry parameters foreland length, hinterland length, and aquifer depth. The influence of aquifer depth has already been studied individually, but not in relation to model length. Numerical modellers typically strive to make their models as efficient as possible. However, before making model length simplifications, the relationship between the model geometry parameters and the hydraulic gradient and Reynolds number must be evaluated.

Three-dimensional groundwater flow

The groundwater flow analysis should be done in a three-dimensional model. This would make the hydraulic head development over the dike even more realistic. As a result, the hydraulic gradient in the pipe becomes more realistic and the piping assessment becomes more accurate.

Pipe geometry

The most uncertain aspect of this study is the pipe geometry schematization. There is no definitive recommendation in the literature on how to schematize a pipe geometry in numerical models. A general schematization strategy for the pipe cross-section should be developed to advance numerical piping models. Furthermore, more piping field experiments should be conducted to determine the true pipe height at various stages of pipe development. In numerical piping models, for example, a relationship between time and pipe height or a relationship between pipe length and pipe height can be implemented.

D-Geo Flow

Deltares released a new version of D-Geo Flow with a redesigned piping assessment module during my thesis. It would be interesting to compare the model principles and the results of this study's proposed numerical model to the principles and results of D-Geo Flow in future research.

General applicability of the Sellmeijer design rule

The purpose of this study was to determine the applicability of the Sellmeijer design rule for four Limburg research locations. However, the design rules are only truly applicable to the experiments that were used to derive the design rule. As a result, the applicability of the Sellmeijer design rules should be evaluated for additional locations in a larger study.

Probabilistic distributions

To minimize probabilistic bias, the stochastic evaluation of the Sellmeijer design rule in Chapter 5 was performed with model parameters sampled from solely uniform distributions. Some parameters, however, are truly distributed differently. Hydraulic conductivity, for example, is lognormally distributed. Therefore, it might be interesting to perform the stochastic evaluation with the corresponding probabilistic distribution of the model parameters.

Relation between Sellmeijer design rule and pipe height

The Sellmeijer design rules determine the global gradient across the dike, independent from the pipe geometry. However, the presence and geometry of the pipe affects the hydraulic head development across the dike. As a result the hydraulic gradient must be assessed for the width of the dike for which the pipe has developed and the width of the dike without the pipe. This means that the global gradient determined by the Sellmeijer design rule is a simplification. Therefore, finding a relationship between the critical global gradient (Sellmeijer design rule) and the pipe height required for piping to occur under these conditions is of interest.

References

Aguilar-López, J., Warmink, J., Schielen, R., & Hulscher, S. (2016a). Piping erosion safety assessment of flood defences founded over sewer pipes. *European Journal of Environmental and Civil Engineering*, *22(6)*, 707-735. doi: 10.1080/19648189.2016.1217793

Aguilar-López, J., Warmink, J., Schielen, R., & Hulscher, S. (2016b). Soil stochastic parameter correlation impact in the piping erosion failure estimation of riverine flood defences. *Structural Safety*, *60*, 117-129. doi: 10.1016/j.strusafe.2016.01.004

AHN. (2022). *AHN viewer (AHN4).* Retrieved 19-5-2022, from `https://www.ahn.nl/ahn-viewer`

Allan, R. (2018). *Backward Erosion Piping.* [PhD Dissertation Thesis, University of New South Wales Australia. Retrieved from `https://primoa.library.unsw.edu.au/permalink/f/1uqach6/TN_cdi _unsw_repository_v2_oai_unsworks_library_unsw_edu_au_1959_4_60238`

Barendsen, L. (2020). *The effect of leakage on backward erosion piping: A modelling study in 2D and 3D.* [Master's Thesis, TU Delft]. Retrieved from `https://repository.tudelft.nl/islandora/ object/uuid%3A4d618b08-b145-4a28-bdc5-ad292e25355d`

Bersan, S., Jommi, C., Koelewijn, A., & Simonini, P. (2013). Applicability of the Fracture Flow Interface to the Analysis of Piping in Granular Material. *Excerpt from the Proceedings of the 2013 COMSOL Conference in Rotterdam.* Retrieved from `https://www.researchgate.net/publication/ 309236859_Applicability_of_the_Fracture_Flow_Interface_to_the_Analysis_of_Piping_in _Granular_Material`

Bligh, W. (1910). Dams Barrages and Weirs on Porous Foundations. *Engineering News*, *64(26)*, 708-710. Retrieved from `https://www.researchgate.net/publication/284080255_Dams_barrages _and_weirs_on_porous_foundation`

Chapuis, R. (2012). Predicting the saturated hydraulic conductivity of soils: a review. *Bulletin of Engineering Geology and Environment*, *71*, 401-434. doi: 10.1007/s10064-012-0418-7

De Limburger. (2021). *Dorpsraad Buggenum kritisch over aanpak wateroverlast, brief verstuurd aan betrokken instanties.* Retrieved 21-12-2022, from `https://www.limburger.nl/cnt/dmf20210730 _93039300`

Deltares. (2012). *Onderzoeksrapport Zandmeevoerende Wellen.* Retrieved from `https:// www.helpdeskwater.nl/publish/pages/130439/onderzoeksrapport_zandmeevoerende_wellen .pdf`

Deltares. (2018). *Fenomenologische beschrijving; Faalmechanismen WBI.* Retrieved from `https://www.helpdeskwater.nl/onderwerpen/waterveiligheid/primaire/beoordelen/ @205760/fenomenologische/#:~:text=Faalmechanismen%20WBI,falen%20van%20de%20kering% 20beschreven.`

DINOloket. (2022). *Ondergrondmodellen.* Retrieved 26-09-2022, from `https://www.dinoloket.nl/ ondergrondmodellen`

Domenico, P., & Schwartz, F. (1990). *Physical and Chemical Hydrogeology* (2nd ed.). John Wiley & Sons. doi: 10.2134/jeq1999.00472425002800060047x

ENW. (2021). *Hoogwater 2021 Feiten en Duiding* (Vol. 2). Retrieved from `https://www.enwinfo.nl/ publicaties/`

Förster, U. (2022). *Dug out pipe at Hedwigepolder.* [Unpublished Photograph].

Google. (2022). *Screenshot of the research locations in Limburg.* [Google Maps]. Retrieved 24-01-2023, from `https://goo.gl/maps/USbCFPYhQeG5UtNS6`

Hoffmans, G., & Van Rijn Emeritus Professor, L. (2017). Hydraulic approach for predicting piping in dikes. *Journal of Hydraulic Research*. doi: 10.1080/00221686.2017.1315747

HWBP. (2022). *HWBP-projecten van Waterschap Limburg.* Retrieved 07-03-2022, from `https://www.hwbp.nl/projecten/overzicht-projecten/limburg/overzicht`

Jonkman, S., R. E. Jorissen, R., Schweckendiek, T., & van den Bos, J. (2021). *Flood Defences, Lecture notes CIE5314* (4th ed.). TU Delft.

Koopmans, R., & Janssen, W. (2018). *POV Piping - Invloed Maasklei en Grindlagen*. Arcadis. Retrieved from `https://publicwiki.deltares.nl/display/HWBPPiping/POV-Piping+Achtergronddocumenten`

Lane, E. (1935). Security from Under-Seepage Masonry Dams on Earth Foundations. *Transactions of the American Society of Civil Engineers*, *100(1)*, 1235-1272. Retrieved from `https://www.researchgate.net/publication/249313415_Security_from_under-seepage_masonry_dams_on_earth_foundations`

Mazzoleni, M., Barontini, S., Ranzi, R., & Brandimarte, L. (2014). Innovative Probabilistic Methodology for Evaluating the Reliability of Discrete Levee Reaches Owing to Piping. *Journal of Hydrologic Engineering*, *20*. doi: 10.1061/(ASCE)HE.1943-5584.0001055

Olsson, A., Sandberg, G., & Dahlblom, O. (2003). On Latin hypercube sampling for structural reliability analysis. *Structural Safety*. doi: 10.1016/S0167-4730(02)00039-5

Pol, J., Van Beek, V., Kanning, W., & Jonkman, S. (2019). Progression rate of backward erosion piping in laboratory experiments and reliability analysis. *7th International Symposium on Geotechnical Safety and Risk (ISGSR 2019): State-of-the-Practice in Geotechnical Safety and Risk*, 769-774. doi: 10.3850/978-981-11-2725-0_IS4-3-cd

Projectbureau Ooijen-Wanssum. (2021). *Foto's Hoogwater 2021*. Retrieved 27-09-2022, from `https://www.ooijen-wanssum.nl/beeld/fotos/hoogwater-2021/25/`

Rijkswaterstaat. (2021). *Schematiseringshandleiding Piping WBI 2017*. Retrieved from `https://www.helpdeskwater.nl/onderwerpen/waterveiligheid/primaire/beoordelen/@205752/schematiseringshandleiding-piping/`

Rijkswaterstaat. (2022). *Rijkswaterstaat Waterinfo.* Retrieved 13-11-2022, from `https://waterinfo.rws.nl/#!/kaart/Waterhoogten`

Robbins, B., Stephens, I., D.A., L., & López-Soto, J. (2016). Laboratory Piping Tests on Fine Gravel. *Canadian Geotechnical Journal*, *55*. doi: 10.1139/cgj-2016-0350

Rosenbrand, E., & Knoeff, H. (2020). *KvK Piping 2018-2019: toepassing ontwikkelde kennis*. Deltares. Retrieved from `https://publications.deltares.nl/11203719_011.pdf`

Sellmeijer, J. (1988). *On the Mechanism of Piping under Impervious Structures*. [PhD Dissertation Thesis, TU Delft]. Retrieved from `https://repository.tudelft.nl/islandora/object/uuid%3A7f3c5919-1b37-4de9-a552-1f6e900eeaad`

Sellmeijer, J. (2006). Numerical computation of seepage erosion below dams (piping). *Verheij, H.J.; Hoffmans, Gijs J. (Hg.): Proceedings 3rd International Conference on Scour and Erosion (ICSE-3), November 1-3*. Retrieved from `https://www.semanticscholar.org/paper/Numerical-computation-of-seepage-erosion-below-dams-Sellmeijer/c8f074750bfbc051689504a9e23a0dff39e90e50`

Sellmeijer, J., J, L., S, L., van Beek, V., & Knoeff, H. (2011). Fine-tuning of the backward erosion piping model through small-scale, medium-scale and IJkdijk experiments. *European Journal of Environmental and Civil Engineering*, *15:8*, 1139-1154. doi: 10.1080/19648189.2011.9714845

Sellmeijer, J., & Koenders, M. (1991). A mathematical model for piping. *Applied Mathematical Modelling*, *15*, 646-651. doi: 10.1061/(ASCE)0733-9410(1992)118:6(943)

Slot, A. (2016). *POV piping grind- en leemlagen, Analyse pompproef deellocatie 4: Thorn*. [Unpublished] INPIJN-BLOKBOEL Ingenieursbureau.

Slot, A., & Lipzig, M. (2016). *POV piping grind- en leemlagen, Analyse pompproef deellocatie 1 (Well) en 3 (Buggenum)*. [Unpublished] INPIJN-BLOKBOEL Ingenieursbureau.

Townsend, F., Bloomquist, D., Shiau, J.-M., Martinez, R., & Rubin, H. (1988). Evaluation of filter criteria and thickness for mitigating piping in sands. *Report to the U.S. Bureau of Reclamation*.

Van Beek, V. (2018). *Grind en grindhoudende lagen in de Maasvallei. Deltares memo 11202002-002-GEO-0002*. Deltares [Unpublished].

Van Beek, V. (2019). *Uitbreiding pipinggevoeligheid grind en grindhoudende zanden Maasvallei. Deltares memo 11202002-002-GEO-0005*. Deltares [Unpublished].

Van Beek, V., Knoeff, J., & Sellmeijer, J. (2011). Observations on the process of piping by underseepage in cohesionless soils in small, medium and large-scale experiments. *European Journal of Environmental and Civil Engineering*, *15(8)*, 1115-1137. doi: 10.1080/19648189.2011.9714844

Van Beek, V., Vandenboer, K., & Bezuijen, A. (2015). Influence of sand type on pipe development in small- and medium-scale experiments. *Scour and Erosion: Proceedings of the 7th International Conference on Scour and Erosion, Perth, Australia*, *2-4*, 111. doi: 10.1201/b17703-14

Van Esch, J. (2014). *WTI 2017: Toetsregel Piping*. Deltares. Retrieved from `https://www.helpdeskwater.nl/onderwerpen/waterveiligheid/primaire/beoordelen/@205823/wti-2017-toetsregel/`

Van Esch, J., Sellmeijer, J., & Stolle, D. (2013). Modeling transient Groundwater Flow and Piping under Dikes and Dams. *3rd International Symposium on Computational Geomechanics (ComGeo III)*. Retrieved from `https://www.researchgate.net/publication/259579510_MODELING_TRANSIENT_GROUNDWATER_FLOW_AND_PIPING_UNDER_DIKES_AND_DAMS`

Van Heerebeek, F. (2012). *Dijken langs de Maas, Resultaten geotechnisch onderzoek, 02P002480*. [Unpublished] INPIJN-BLOKBOEL Ingenieursbureau.

Van Heerebeek, F. (2013). *Monitoring grondwaterstanden Waterkeringen langs de Maas, Resultaten geotechnnisch onderzoek, 02002578-01*. [Unpublished] INPIJN-BLOKBOEL Ingenieursbureau.

Verhulst, P. (2017). *Piping in de Maasvallei, A possibility or far-fetched scenario?* [Master's thesis TU Delft]. Retrieved from `https://repository.tudelft.nl/islandora/object/uuid%3A286a1b6a-6c57-49c3-bb87-b30778f16e45`

Waterschap Hollandse Delta. (2022). *Pipingproef Hedwigepolder*. Retrieved 29-11-2022, from `https://www.wshd.nl/pipingproef`

Waterschap Limburg. (2018). *Piping parameters voor VO+ ontwerp, HWBP Noordelijke Maasvallei*. [Unpublished].

Waterschap Limburg. (2020). *WBI Limburg, Technische Uitgangspunten Notitie. 2019-D36462*. [Unpublished].

Waterschap Limburg. (2021). *Standpipe and pore pressure gauge data 28-06-2021 to 07-08-2021*. [Unpublished raw data].

Wewer, M. (2019). *Development of an optimal sensing strategy for dike monitoring of backward erosion piping with fibre optic cable based sensors*. [Master's Thesis, Technische Universität Dresden].

White, C. (1940). The equilibrium of grains on the bed of a stream. *Proceedings of the Royal Society of London. Series Applied Mathematical and Physical Science.*, *174(958)*, 322-338. doi: 10.2307/97393

Zhou, X., Jie, Y., & Li, G. (2012). Numerical simulation of the developing course of piping. *Computers and Geotechnics*, *44*, 104-108. doi: 10.1016/j.compgeo.2012.03.010

Appendix

A
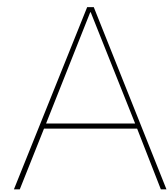
Subsoil characteristics and schematization

This appendix summarises the data and methods that are used to schematize the research locations into the cross-sectional models in Section 3.3. First, an overview of all subsoil composition data is given to schematise a subsoil layer system in the model. Afterwards, the determination of the representative grain size and permeability/hydraulic conductivity is demonstrated.

A.1. Subsoil layering

This section contains all the data that is used to schematize the subsoil layering system of the research location to implement in the numerical models. The results of the schematization are shown in Tables A.6, A.7, A.8 and A.9.

Well

- Figure A.1: Near Well extensive subsoil studies have been performed during the project 'POV piping - Invloed Maasklei en Grindlagen' (Koopmans & Janssen, 2018). However, the research location near Well is situated slighly different this time. Therefore, in order to get a sufficient idea of the subsoil composition the result of several cone penetration tests (CPT) of the project 'Dijken langs de Maas' (Van Heerebeek, 2012) have been interpreted and drawn next to each other in Figure A.1. Figure A.4 is the corresponding legenda.

- Figure A.2: Subsoil model from DINOloket that gives an idea of the deep subsoil layer composition.

- Figure A.3: Drilling profile of the pore pressure gauges at the research location near Well at 60.069+10 (Van Heerebeek, 2013).
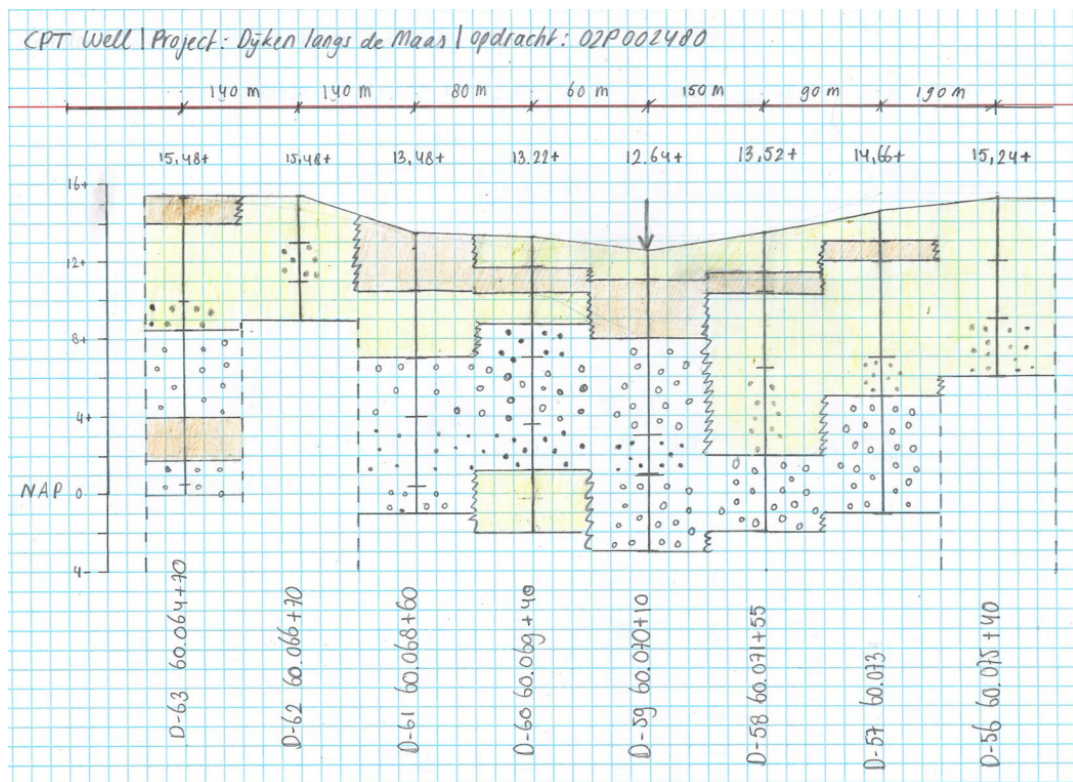
Figure A.1: Subsoil schematization Well - based on 8 CPT of project 'Dijken langs de Maas' (Van Heerebeek, 2012)

Figure A.2: Subsoil model Well BRO GeoTOP v1.4.1 (DINOloket, 2022)
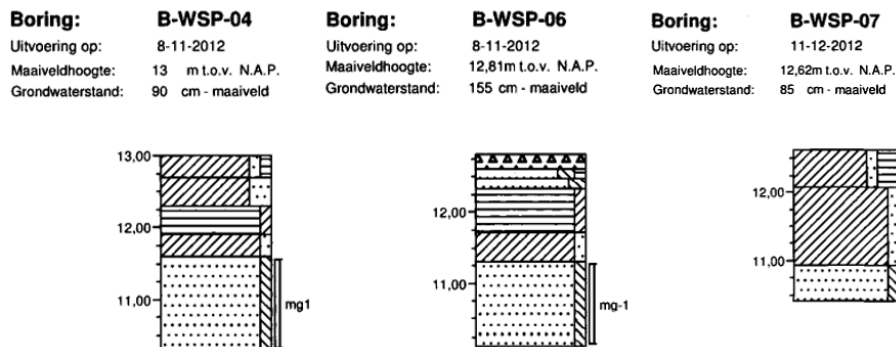
Figure A.3: Drilling profiles of pore pressure meters Well (Van Heerebeek, 2013)

Hout-Blerick

- Figure A.4: shows the legenda corresponding to Figure A.5 and Figure A.1.

- Figure A.5: For the research location near Hout-Blerick there is no extensive subsoil study available that provides deep drilling profiles. Therefor, to get a sufficient idea of the subsoil composition the result of several cone penetration tests (CPT) of the project 'Dijken langs de Maas' (Van Heerebeek, 2012) have been interpreted and drawn next to each other in Figure A.5. Figure A.4.

- Figure A.6: Subsoil model from DINOloket that gives an idea of the deep subsoil layer composition.

- Figure A.7: Drilling profile of the pore pressure gauges at the research location near Hout-Blerick at 70.075+10 (Van Heerebeek, 2013).
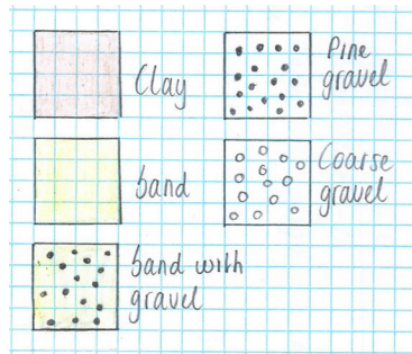
Figure A.4: Legenda drawings subsoil schematizations
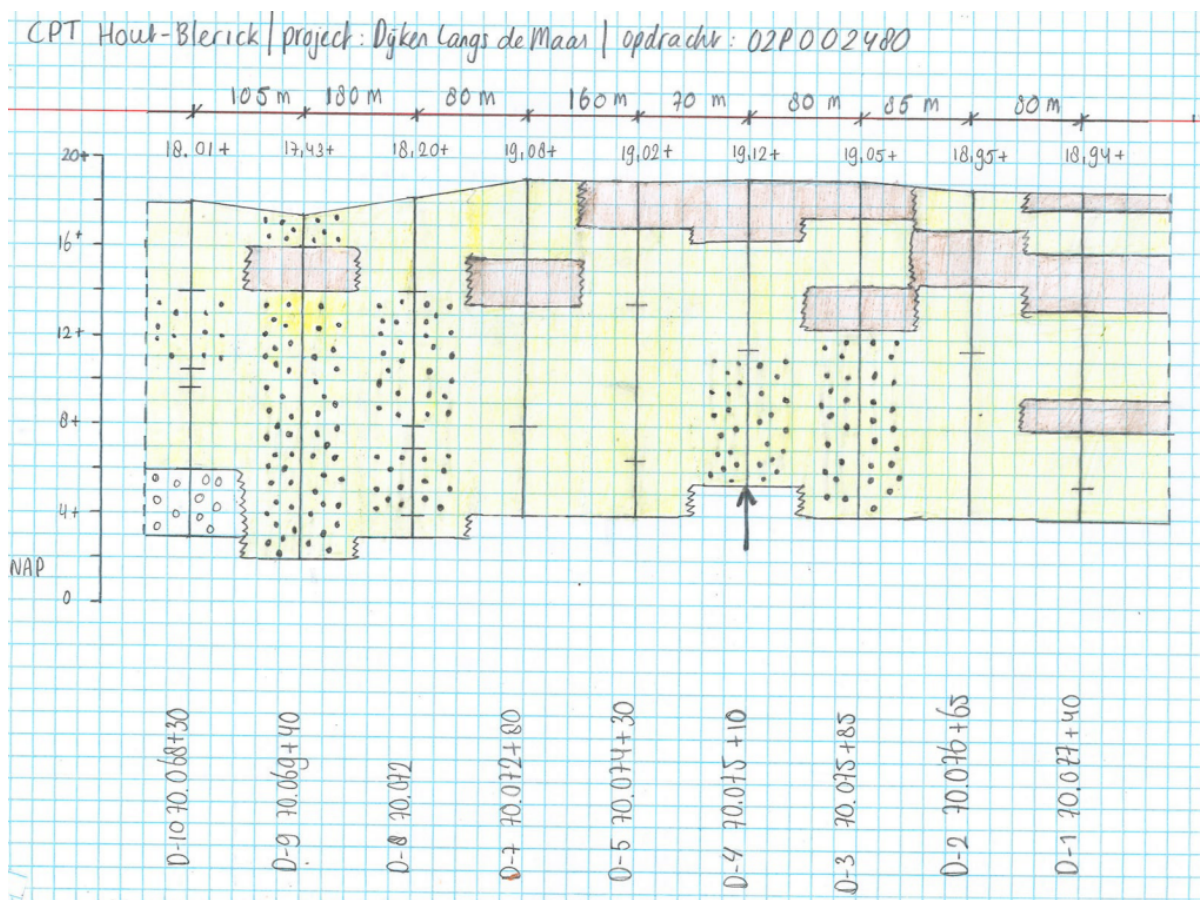
Figure A.5: Subsoil schematization Hout-Blerick - based on 9 CPT of project 'Dijken langs de Maas' (Van Heerebeek, 2012)

Verticale Doorsnede BRO GeoTOP v1.4.1
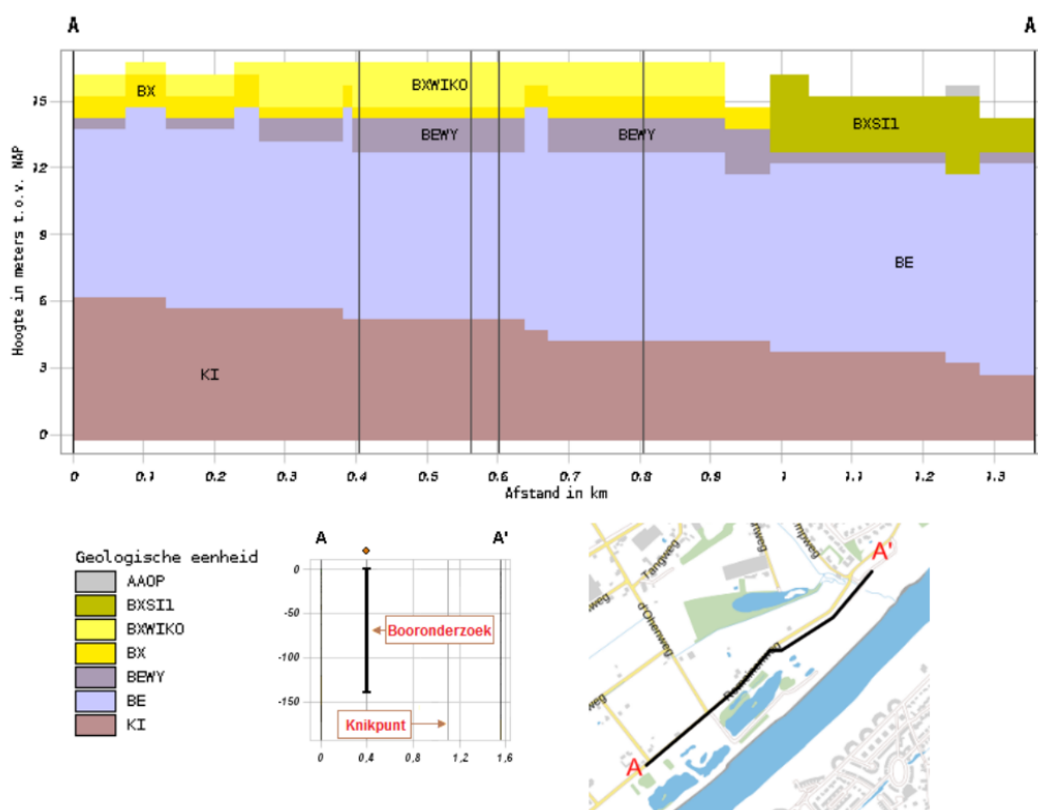
Figure A.6: Subsoil model Hout-Blerick BRO GeoTOP v1.4.1 (DINOloket, 2022)
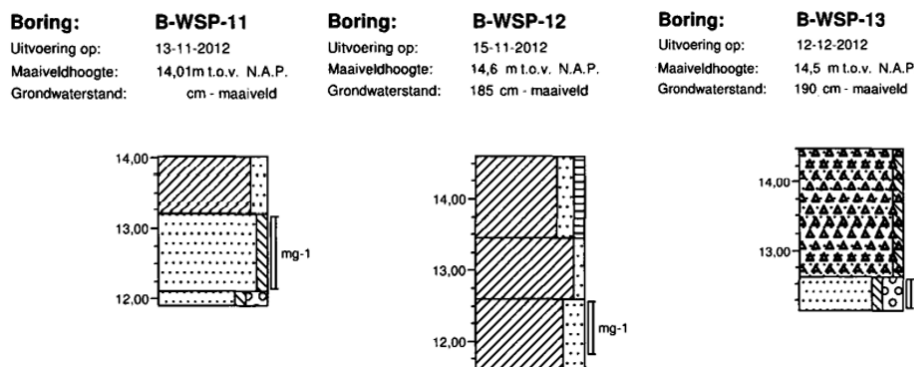
Figure A.7: Drilling profiles of pore pressure meters at Hout-Blerick 70.075+10 (Van Heerebeek, 2013)

Buggenum

- Figure A.8: Drilling profiles of Buggenum at dike section 75.030+50. The profiles are part of the project 'POV piping - Invloed Maasklei en Grindlagen' (Koopmans & Janssen, 2018), but are derived from the pump test by Slot & Lipzig (2016).

- Figure A.9: Subsoil model from DINOloket that gives an idea of the deep subsoil layer composition.

- Figure A.10: Drilling profile of one of the pore pressure gauges at the research location near Buggenum (Van Heerebeek, 2013). However, in the standpipe data three pore pressure gauges are depicted while only one drilling profile is included in the report 'Monitoring grondwaterstanden

Waterkeringen langs de Maas, Resultaten geotechnnisch onderzoek' (Van Heerebeek, 2013).
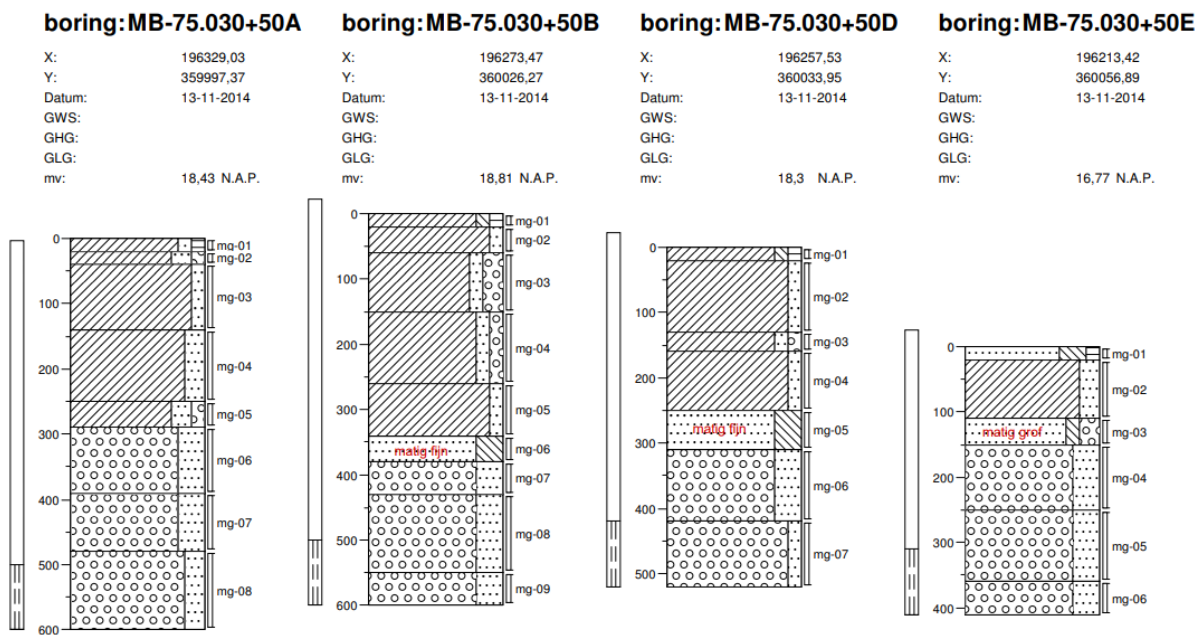
Figure A.8: Drilling samples Buggenum line section 75.030+50

Figure A.9: Subsoil model Buggenum BRO REGIS II v2.2 (DINOloket, 2022)

Boring: **B-WSP-14**

Uitvoering op: 13-12-2012
Maaiveldhoogte: 16,31m t.o.v. N.A.P.
Grondwaterstand: 190 cm - maaiveld
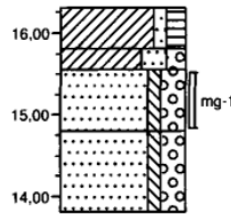
Figure A.10: Drilling profiles of pore pressure meters Buggenum (Van Heerebeek, 2013)

Thorn

- Figure A.11: Drilling profiles of Thorn at dike section 79.037. The profiles are part of the project 'POV piping - Invloed Maasklei en Grindlagen' (Koopmans & Janssen, 2018), but are derived from the pump test by Slot (2016).

- Figure A.12: For these profiles applies the same as Figure A.11. However, these drilling profiles are made at section 79.037+50.

- Figure A.13: Subsoil model from DINOloket that gives an idea of the deep subsoil layer composition.

- Figure A.14: Drilling profile of one of the pore pressure gauges at the research location near Thorn (Van Heerebeek, 2013). However, in the standpipe data four pore pressure gauges are depicted while only one drilling profile is included in the report 'Monitoring grondwaterstanden Waterkeringen langs de Maas, Resultaten geotechnnisch onderzoek' (Van Heerebeek, 2013).
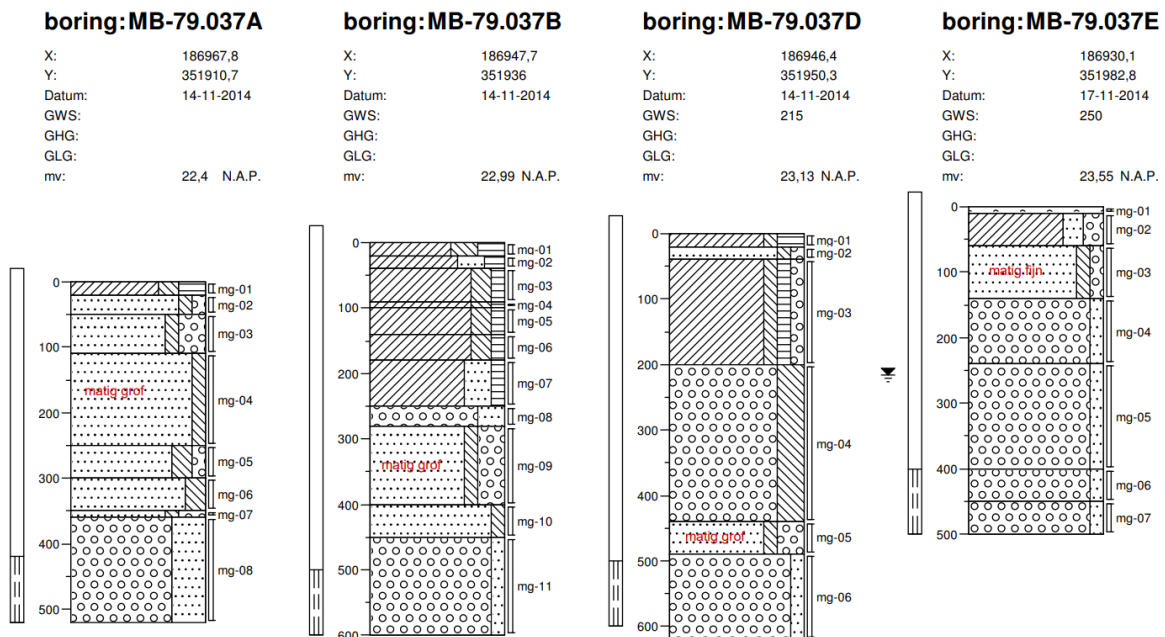
Figure A.11: Drilling samples Thorn dike section 79.037 (Slot, 2016)
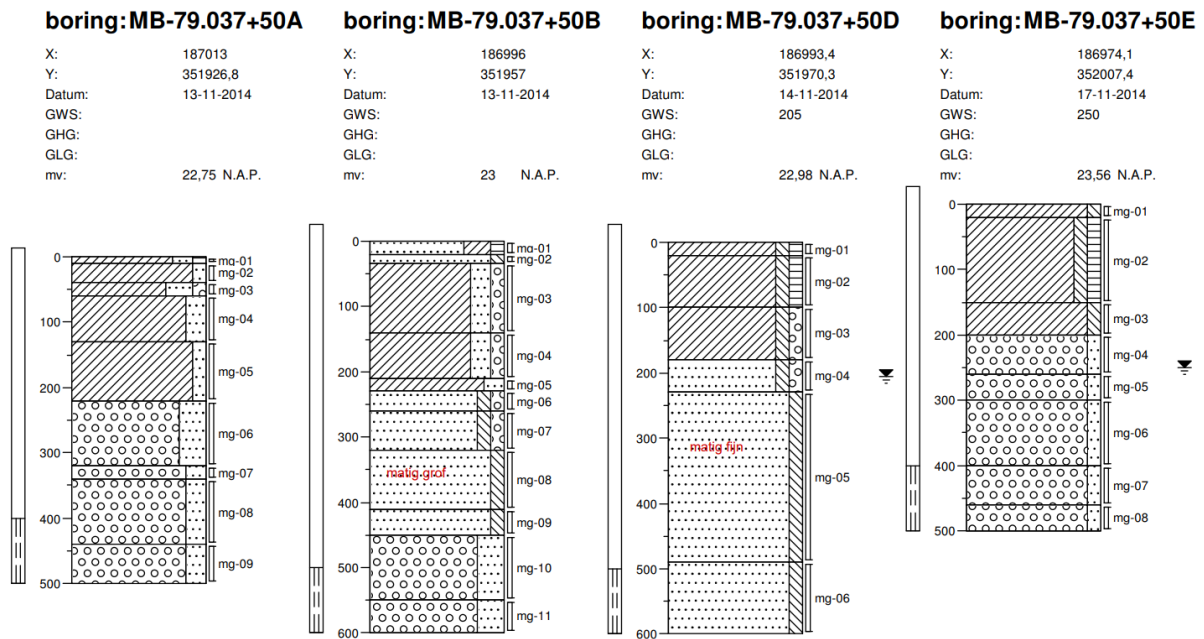
Figure A.12: Drilling samples Thorn line section 79.037+50 (Slot, 2016)
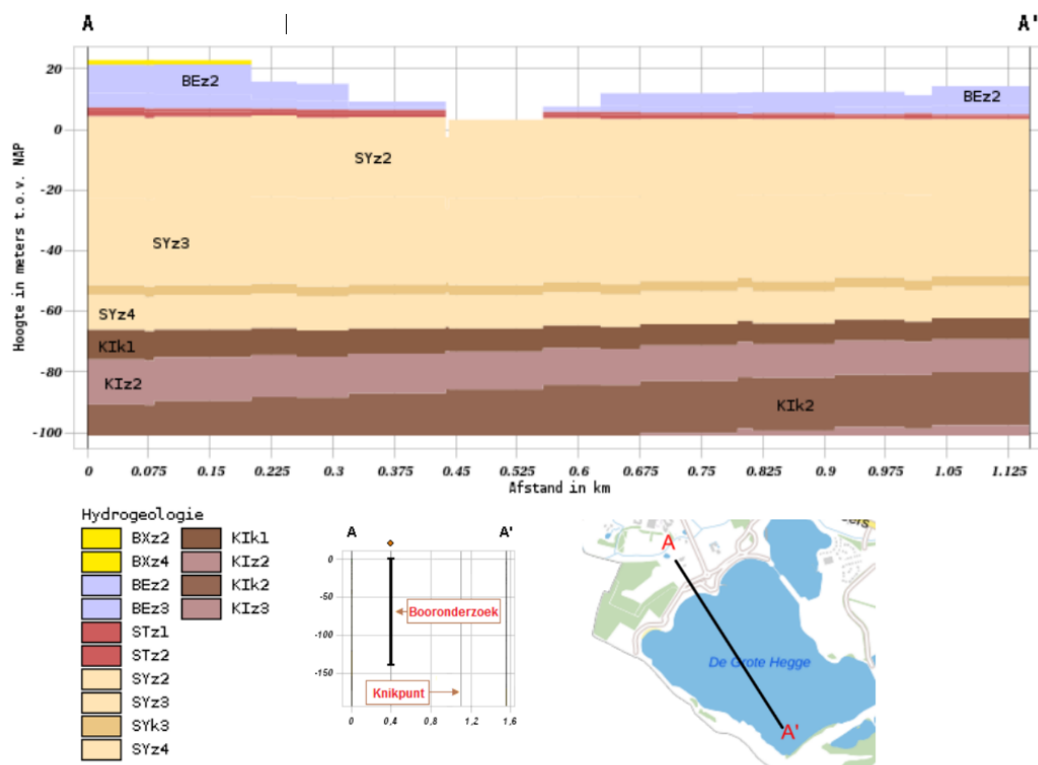
Figure A.13: Subsoil model Thorn BRO REGIS II v2.2 (DINOloket, 2022)

Boring: **B-WSP-18**

Uitvoering op: 14-12-2012
Maaiveldhoogte: 23,7 m t.o.v. N.A.P.
Grondwaterstand: 195 cm - maaiveld
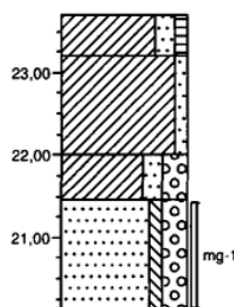
Figure A.14: Drilling profiles of pore pressure meters Thorn (Van Heerebeek, 2013)

A.2. Grain size determination

For each research location, the site-specific hydrogeological parameters are studied and then coupled to the numerical model. Hydrogeological parameters such as hydraulic conductivity and the representative grain size (d_{70}) can be derived from mechanically drilled and manually drilled samples. For fine materials manually drilled samples give a more accurate result than mechanically drilled samples. However, drilling through gravel is not possible by hand. As a result, for coarse materials, mechanically drilled samples are used to calculate hydrogeological parameters.

Tables A.1, A.2, A.3 and A.4 contain a set of representative grain sizes derived from different sieve curve analyses. The representative grain sizes were extracted from several sieve curve samples from the projects 'POV Piping - Invloed Maasklei en Grindlagen' (Koopmans & Janssen, 2018) and 'Monitoring grondwaterstanden Waterkeringen langs de Maas' (Van Heerebeek, 2013). A selection of the sieve curve samples is made. Because it is assumed that piping occurs in a sand layer beneath the cover layer, samples containing gravel are excluded from the selection.

The definite grain sizes that are applied throughout the rest of this study are shown in bold text in Tables A.1, A.2, A.3 and A.4.

Table A.1: Grain size overview Well

Project/source	Material type	d_{10} [mm]	d_{50} [mm]	d_{60} [mm]	d_{70} [mm]
POV-piping (Slot & Lipzig, 2016) *Well (bron) mg-03	very coarse faint silty sand, high gravel content	0.190	0.490	0.680	0.952
*Well (bron) mg-06	extremely coarse sand, high gravel content	0.230	0.475	0.607	0.798
Well (bron) mg-08	extremely coarse sand, medium gravel content	0.210	0.448	0.540	0.695
(Van Heerebeek, 2013) B-WSP-04 mg-1	Extremely coarse faint silty sand medium gravel content	0.182	0.430	0.490	0.650
B-WSP-06 mg-1	Extremely coarse faint silty sand low gravel content	0.178	0.420	0.490	0.600
B-WSP-07 mg-1	Extremely coarse sand medium gravel content	0.255	0.480	0.505	0.720
Average of (Van Heerebeek, 2013)		**0.205**	**0.430**	**0.495**	**0.660**

*Are not taken into account in calculating the average values due to outlier values

Table A.2: Grain size overview Hout-Blerick

Project/source	Material type	d_{10} [mm]	d_{50} [mm]	d_{60} [mm]	d_{70} [mm]
(Van Heerebeek, 2013) B-WSP-11 mg-1	Very coarse extremely silty sand medium gravel content	-	0.170	0.255	0.390
B-WSP-12 mg-1	Extremely coarse sand	0.255	0.410	0.490	0.590
B-WSP-13 mg-1	Very coarse sand low gravel content	0.240	0.380	0.410	0.510
Average		**0.165**	**0.320**	**0.385**	**0.500**

Table A.3: Grain size overview Buggenum

Project/source	Material type	d_{10} [mm]	d_{50} [mm]	d_{60} [mm]	d_{70} [mm]
(Van Heerebeek, 2013) B-WSP-14 mg-1	Very coarse faint silty sand high gravel content	**0.210**	**0.480**	**0.700**	**0.900**

Table A.4: Grain size overview Thorn

Project/source	Material type	d_{10} [mm]	d_{50} [mm]	d_{60} [mm]	d_{70} [mm]
POV-piping (Slot, 2016) HB-33 mg-4 mm70	medium coarse sand, low gravel content	0.130	0.245	0.300	0.350
HB-34 mg-6 mm71	very coarse silty sand, high gravel content	-	0.340	0.400	0.500
HB-35 mg-8 mm72	very coarse sand, medium gravel content	0.190	0.390	0.420	0.490
HB-36 mg-8 mm73	very coarse low silty sand, medium gravel content	0.063	0.370	0.400	0.480
*HB-37 mg-4 mm75	very coarse low silty sand, high gravel content	0.140	0.400	0.560	1.2
*HB-37 mg-5 mm76	very coarse low silty sand, high gravel content	0.220	0.600	0.850	1.3
HB-39 mg-6 mm77	very coarse low silty sand, medium gravel content	0.130	0.310	0.380	0.420
HB-39 mg-7 mm78	very coarse sand, high gravel content	0.200	0.410	0.480	0.580
*MB-04 mg-6,7,8 mm79	very coarse sand, high gravel content	0.200	0.490	0.780	2.0
MB-04 mg-31,32,33 mm88	very coarse sand,	0.260	0.360	0.370	0.390
(Van Heerebeek, 2013) B-WSP-18 mg-1	Very coarse faint silty sand low gravel content	0.063	0.320	0.400	0.485
Average		**0.148**	**0.343**	**0.395**	**0.460**

*Are not taken into account in calculating the average values due to outlier values

A.3. Permeability/hydraulic conductivity estimation

If measurements of the hydraulic conductivity or intrinsic permeability of subsoil layers are scarce or non-existent for a site of interest, the hydraulic conductivity can be estimated using empirical formulas. Various empirical formulas for estimating hydraulic conductivity have been developed over time. The empirical formulas are used to determine whether the hydraulic conductivity found in the pumping tests

of POV-piping is applicable to the research locations (Slot & Lipzig, 2016; Slot, 2016). For the research location Hout-Blerick, the hydraulic conductivity of the sand layer cannot be derived from previous studies. Therefore it is derived from the empirical formulas listed below.

Kozeny-Carman
Chapuis (2012) demonstrates that all of these formulas are applicable to a variety of soil types. The formula requires an input value for fluid density, fluid dynamic viscosity, porosity, and an average grain size value. The d_{50} is used as the average grain size value. When porosity is unknown, it can be estimated using Equation A.2 Mazzoleni et al. (2014).

$$K = \frac{\rho g}{\mu} \frac{\epsilon^3}{(1-\epsilon)^2} \frac{d_p^2}{180} \tag{A.1}$$

$$\epsilon = 0.255 \left(1 + 0.83^{\frac{d_{60}}{d_{10}}} \right) \tag{A.2}$$

Den Rooijen 1992 (Deltares, 2012)
According to 'WBI Limburg, Technische Uitgangspunten Notitie' (Waterschap Limburg, 2020) the permeability must be determined with the empirical formula of Den Rooijen. The Den Rooijen formula contains a constant c_0 to represent the packing of the soil. The packing coefficients are:

- loose packing: $c_0 = 1.5 \cdot 10^4$ m^{-1}s^{-1}
- medium packing: $c_0 = 1.2 \cdot 10^4$ m^{-1}s^{-1}
- tight packing: $c_0 = 1.0 \cdot 10^4$ m^{-1}s^{-1}

$$K = \left(c_0 - 1.83 \cdot 10^3 \cdot \ln \left(\frac{d_{60}}{d_{10}} \right) \right) d_{10}^2 \tag{A.3}$$

Seelheim
Fill in d_{50} in millimetres.

$$K = 0.00357 \cdot d_{50}^2 \tag{A.4}$$

Hazen
Fill in d_{10} in millimetres.

$$K = 0.0116 \cdot d_{10}^2 \tag{A.5}$$

Results
The estimated hydraulic conductivity of the sand layer at the research location is demonstrated in Table A.5. The final grain sizes of Tables A.1, A.2, A.3 and A.4 form the input parameters for the empirical formulas. The last column of Table A.5 contains the hydraulic conductivity according to the pumping tests in POV-piping (Slot & Lipzig, 2016; Slot, 2016).

The hydraulic conductivity that is used for the sand layer in further analyses of this thesis are marked in bold in Table A.5. From comparison, it can be seen that the hydraulic conductivity values found during the POV-piping project (Koopmans & Janssen, 2018) for Well and Thorn are correct. However, the hydraulic conductivity of the empirical formulas for Buggenum, is quite different from found during POV-piping. As a result, the sand layer's hydraulic conductivity is chosen to be equal to the result of Equation A.3 for medium soil packing.

A.4. Schematization per research location

In Tables A.6, A.7, A.8 and A.9, the subsoil layer schematization and characteristics are summarized by research location. The subsoil layering is constructed using samples and data from the appendix's first section. A double line divides the subsoil layers into two in each table. This line represents the numerical model's maximum depth for that research location. That is, the layers above the double line are implemented in the models.

Table A.5: Hydraulic conductivity [m/d] estimation sand layer

	Kozeny-Carman [m/d]	Den Rooijen			Seelheim [m/d]	Hazen [m/d]	POV-piping [m/d]
		Loose	Medium	Tight			
Well	36	49	38	30	57	42	**48**
Hout-Blerick	20	31	25	**20**	32	28	
Buggenum	45	50	**37**	30	72	44	75
Thorn	23	25	20	15	36	23	**30**

Table A.6: Subsoil layer schematization Well

Description/ material	Formation	Lower side layer [m + NAP]	Layer thickness [m]	K [m/d]	d_{70} [mm]
Crest height		15.25			
Surface level		13 / 12.8			
Clay	Holoceen; Boxtel	11.5	1.5 / 1.3	0.6	-
Coarse sand	Beegden	8.5	3	48	0.660
Gravel	Beegden	-2.5	11	125	12
Coarse sand	Kiezeloöliet	-5.5	3	-	-
Geohydrological base	Breda	-191.5	186	-	-

Table A.7: Subsoil layer schematization Hout-Blerick

Description/ material	Formation	Lower side layer [m + NAP]	Layer thickness [m]	K [m/d]	d_{70} [mm]
Crest height		19			
Surface level		14 / 14.5			
Clay	Holoceen; Boxtel	12	2	0.46	-
Mod. coarse sand	Beegden	6.5	5.5	20	0.500
Coarse sand	Beegden	-2	8.5	75	2
Geohydrological base	Kiezoloöliet*	-53	51	-	-

Table A.8: Subsoil layer schematization Buggenum

Description/ material	Formation	Lower side layer [m + NAP]	Layer thickness [m]	K [m/d]	d_{70} [mm]
Crest height		22.10			
Surface level		18 / 17			
Clay	Holocene	16	2 / 1.0	0.29	-
Sand	Boxtel	15.2	0.8	37	0.900
Gravel	Beegden	7	8.2	184	-
Gravel	Beegden	-2.5	9.5	110	-
Coarse sand river deposit	Sterksel *	-20.5	18	12.5	-
Clay and sand	Stramproy	-76.5	56	-	-
Geohydrological base	Waalre *	-82.5	6	-	-

Table A.9: Subsoil layer schematization Thorn

Description/ material	Formation	Lower side layer [m + NAP]	Layer thickness [m]	K [m/d]	d_{70} [mm]
Crest height		25.4			
Surface level		22.94 / 23.7			
Clay	Holoceen; Boxtel	22.2	0.72 / 1.5	0.49	-
Coarse sand	Beegden	20.4	1.8	30	0.460
Gravel package	Beegden	6.1	14.3	85	27
Coarse sand river deposit	Sterksel	5.1	1.0	-	-
Fine sand deposit	Strampoy	-64.4	69.5	-	-
Geohydrological base	Kiezeloöliet	-109.4	45.0	-	-

B

Sensitivity analysis model parameters

Calibration involves comparing hydraulic head field measurement data with the hydraulic head simulated by the cross-sectional models and fine-tuning model parameters to ensure that the model output hydraulic head accurately represents the field measurement data. As a result, understanding the impact of model parameters on the model's hydraulic head output is critical. A sensitivity analysis was performed to investigate the influence of the following parameters: hydraulic conductivity of different layers (K [m/d]), layer thicknesses (D [m]), length of the foreland and hinterland, anisotropy, and porosity.

B.1. Control model

All sensitivity analyses have been performed for the cross-sectional model of Well. The model geometry has been rebuilt to a normal dike geometry without any piping characteristics. It is critical to begin each sensitivity analysis with the same model geometry and model parameters to ensure consistency. This cross-sectional model is known as the Well control model. The control parameters of the control model are shown in Table B.1 below. The control model is also plotted in each sensitivity analysis plot to quantify the effect of a particular model parameter variation. The control model is always represented by a dashed black line and is referred to as Control in the legends.

The location and depth in the cross-sectional model where the hydraulic head development is determined is another constant condition for the sensitivity analysis. For each sensitivity analysis the hydraulic head development is assessed at a depth of 1 m beneath the bottom of the clay layer.

Parameter	Unit	Value
D_clay	[m]	1.5
D_sand	[m]	3
D_grav	[m]	11
K_clay	[m/d]	0.6
K_sand	[m/d]	48
K_grav	[m/d]	125
ϵ_clay	[-]	0.5
ϵ_sand	[-]	0.3
ϵ_grav	[-]	0.4
ϵ_pipe	[-]	1.0
L	[m]	24
L_f	[m]	30
L_h	[m]	30
W	[m]	2.68
h_b	[m]	0

Table B.1: Parameters control model
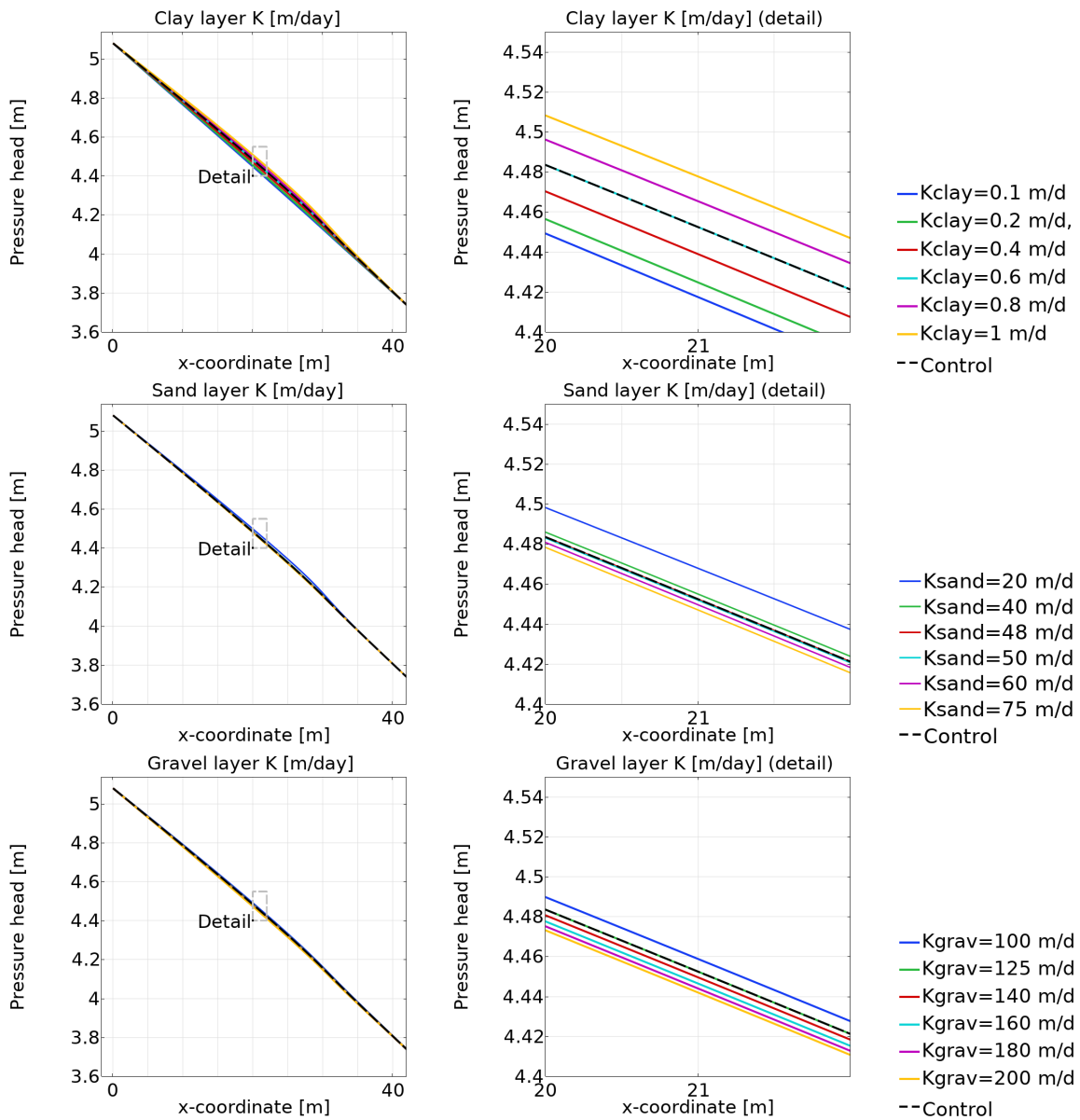
Figure B.1: Sensitivity analysis hydraulic conductivity K [m/day]

B.2. Hydraulic conductivity

The cross-sectional model of Well consists of three layers: clay, sand, and gravel. A range of hydraulic conductivity values have been tested for each layer. The parameter value ranges are chosen to be realistic for the soil type, as proposed by Koopmans & Janssen (2018). Keep in mind that the vertical and horizontal axes have been chosen to best show the effect of parameter variation. A general hydraulic head development is shown for each soil type or layer, as well as a detail to show the magnitude of the effects. Because the graph is mirrored for the second half of the dike and hinterland (x > 42m), the general head development is given for the model's foreland until half of the dike (x = 42m).

The sensitivity analysis in Figure B.1 shows that variation in the hydraulic conductivity of the clay layer has the greatest effect, because the hydraulic head quantity varies by 8 cm. The hydraulic conductivity of the sand and gravel layer has an effect of 1-2 cm.
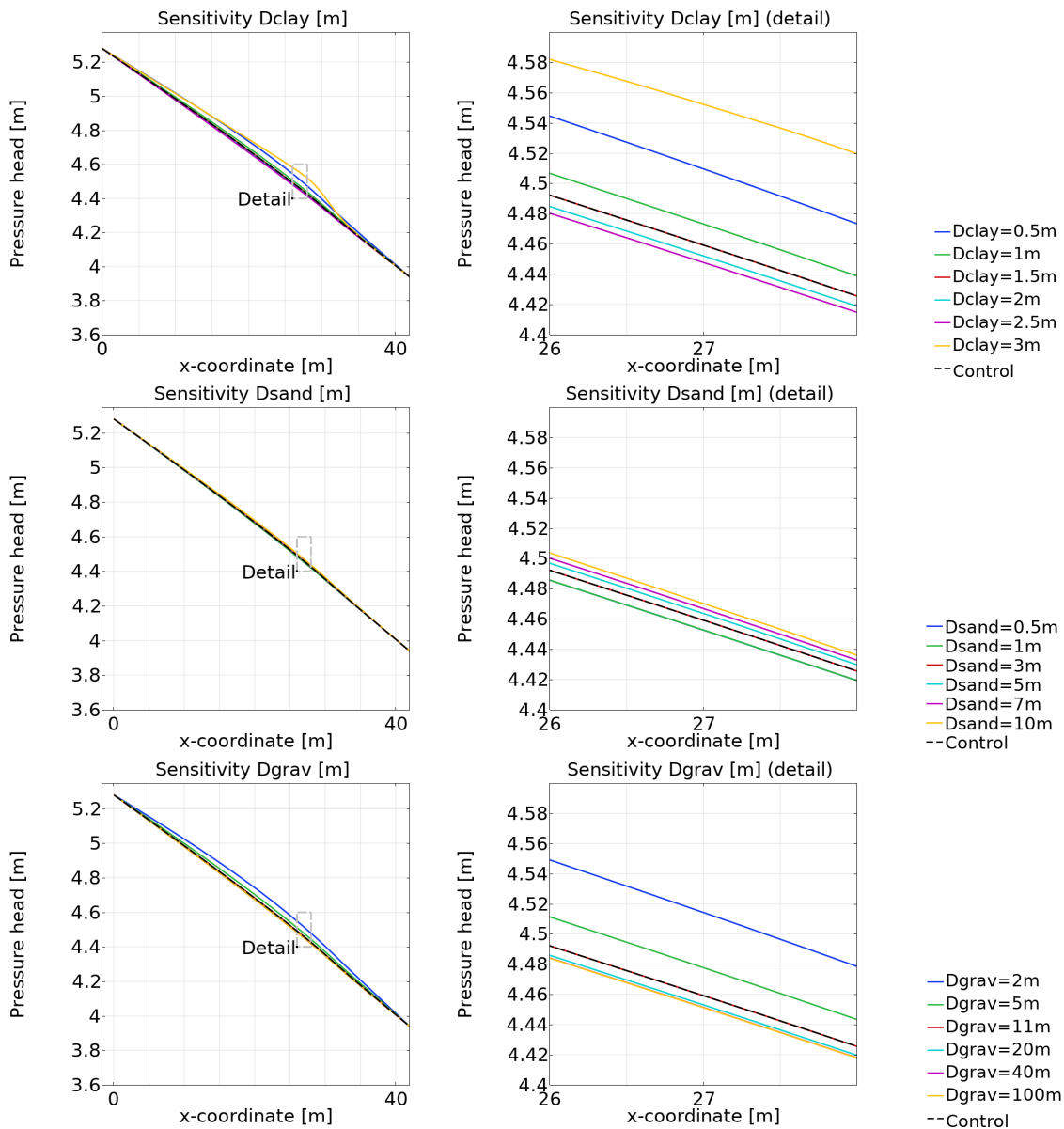
Figure B.2: Sensitivity analysis layer thickness D [m]

B.3. Layer thicknesses

The second model parameter for which a sensitivity analysis is performed is layer thickness. In the Well control model, different layer thickness values are tested for each soil layer to see how they affect the hydraulic head development in the aquifer.

The influence of each layer thickness variation can be seen in Figure B.2. The figure shows that variation in the thickness of the clay layer has the greatest effect on the hydraulic head development, which is in the order of 9 cm. Because more pressure builds up beneath the cover layer, a thicker clay layer causes a higher hydraulic head in the aquifer. Variation in sand layer thickness has little effect on the hydraulic head; the maximum deviation from the control line is in the order of about 1 cm.

The maximum effect of gravel layer variation (distance from the control line) is in the order of 6 cm. The hydraulic head increases as the gravel layer thickness decreases, indicating that the parameters are inversely proportional to one another. It should be noted that for a 2 m thick gravel layer, the entire model loses 7 m in depth because the gravel layer is 11m thick in the control model. The amount of flux and groundwater flowing through the entire aquifer is distributed across the sand and gravel

layer. However, because the gravel layer has a higher permeability than the sand layer, more flux and groundwater flows through it. When the gravel layer shrinks, more groundwater/flux flows through the sand layer, increasing the hydraulic head in the sand layer, which is also where the hydraulic head for the sensitivity analysis is determined.

B.4. Anisotropy

Anisotropy is the difference between a soil's horizontal (κ_h [m^2]) and vertical (κ_v [m^2]) permeability. For model calibration, isotropic soil properties ($kh/kv = 1$) are used as a starting point. However, soil in the northern Maasvallei is anisotropic, with a permeability factor (κ_h/κ_v) ranging from 1 to 6 (Waterschap Limburg, 2018), and the typical anisotropy factor for coarse sand ranging from 1 to 3 (Slot & Lipzig, 2016). As a result, the influence of anisotropy on the development of the hydraulic head is examined in Figure B.3. In the sensitivity analysis, the maximum and minimum permeability factors for the sand and underlying gravel layer are considered for convenience. Because water flows mostly vertically through the clay cover layer, it is not taken into account in the anisotropy sensitivity analysis.
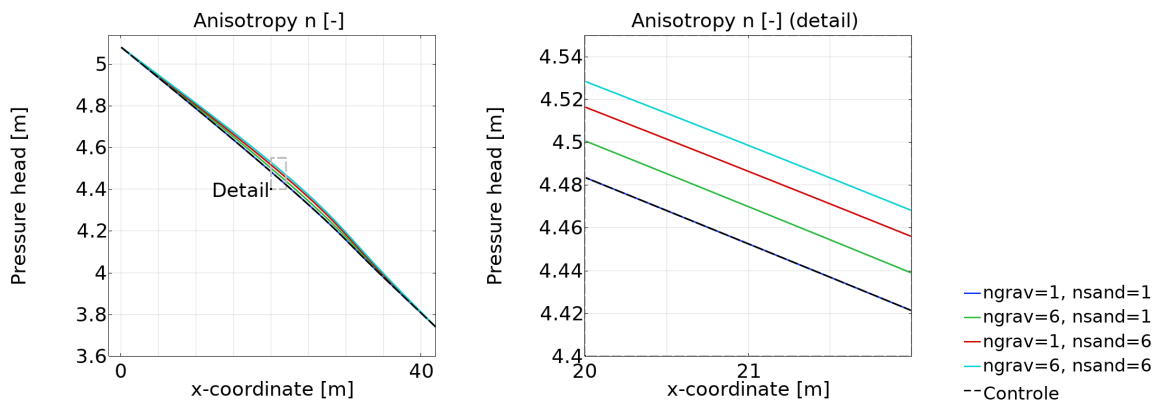
Figure B.3: Sensitivity analysis anisotropy

The analysis in Figure B.3 shows that a higher permeability factor results in a higher pressure head. This demonstrates that increasing the permeability factor has the same effect as decreasing the hydraulic conductivity (as shown in Figure B.1). Both variations increase the resistance acting on groundwater flow.

Because the pressure head is measured in the sand layer, the pressure head is higher when applying the maximum permeability factor on the sand layer (red line in Figure B.3) than on the gravel layer (green line in Figure B.3).

B.5. Foreland and hinterland length

The foreland and hinterland lengths are two parameters that determine not only the length of the model, but also how the fluxes that enter and exit the model operate. The length of the model influences how the boundary conditions affect the model. The model has more freedom to solve Darcy's law and simulate hydraulic head development when the boundaries are set further apart than when the boundaries are close to the dike. The boundary conditions dominate the model elements for a short foreland and hinterland. Furthermore, the area for fluxes to enter and exit the model is more restricted for a shorter model, which influences the number of fluxes in the model.

The influence of the foreland and hinterland length is analysed individually (uncorrelated) in Figures B.4 and B.5 and together (correlated) in Figure B.6. The position of the dike varies along the horizontal axis due to variations in foreland length. Therefore , the dike is indicated in each figure by a dotted surrounded area in the same colour as the corresponding pressure head development. The average pressure head gradient over the dike is later used to determine piping. The effect of varying foreland and hinterland lengths on the average pressure gradient over the dike in the aquifer is depicted in Figure B.7.

Figures B.4 to B.6 show similar effects when a longer foreland and hinterland are used. The longer the applied foreland length in the model, the more curvature the pressure head development gets in the foreland until the dike is reached (see Figure B.4). A short foreland length results in nearly linear pressure head development along the horizontal axis. In Figure B.5, a constant hinterland length is used, resulting in a constant shape along the plots past the indicated dike. Figure B.5 demonstrates that a longer hinterland length results in a more logarithmic plot profile. The combined effect of having equal values for the foreland and hinterland (short and long) is shown in Figure B.6.
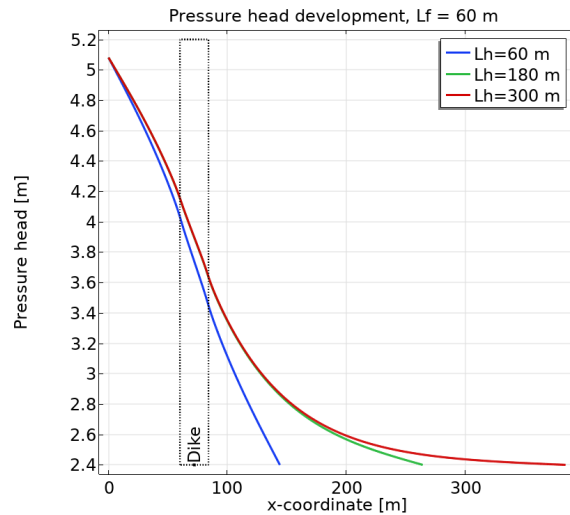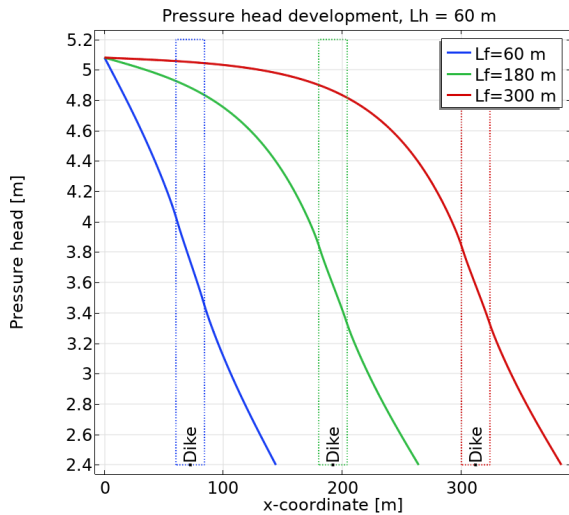
Figure B.4: Pressure head development over the model length for varying L_f **Figure B.5:** Pressure head development over the model length for varying L_h
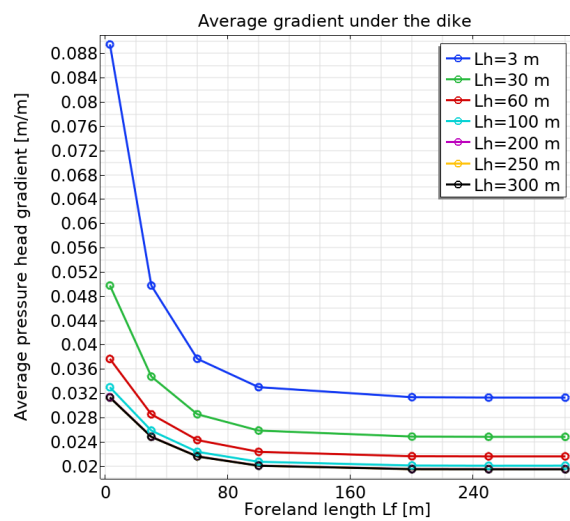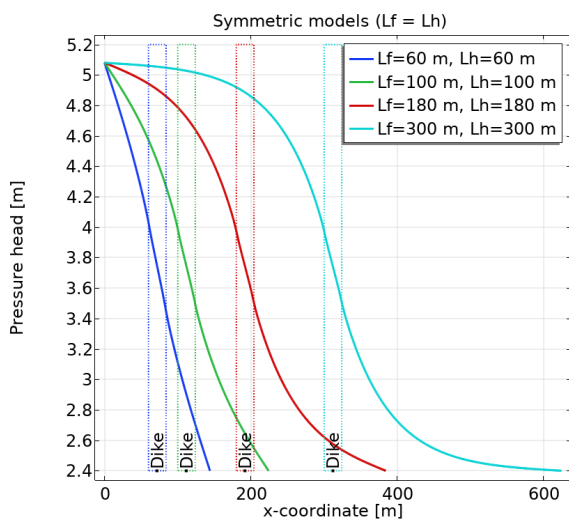
Figure B.6: Pressure head development over the model length for equal L_f and L_h **Figure B.7:** Effect of model length on average pressure head gradient under dike

The influence of the foreland and hinterland lengths on the average pressure head gradient over the dike must be studied in order to determine piping. According to Figures B.4 to B.6, the average pressure head gradient over the dike area appears to be almost constant for the different foreland and hinterland compositions. However, when the average pressure head gradient is closely studied, variations in the average pressure head gradient are discovered. Figure B.7 depicts the mean pressure head over the dike for various foreland and hinterland length compositions.

The total model length (the sum of the foreland length, dike width, and hinterland length) determines the average pressure head gradient over the dike, according to this figure. For example, a foreland

length of 60 m and a hinterland length of 100 m produce the same average pressure head gradient as a foreland length of 100 m and a hinterland length of 60 m. It can also be concluded that the average pressure head gradient decreases with increasing total model length.

B.6. Discussion

The geometry of the control model influences the magnitude of the effect that the parameters discussed above have on the hydraulic or pressure head development. The foreland and hinterland lengths, as shown in Appendix B.5, determine the development of the pressure head over the model length. A foreland and hinterland length of 30 m is used in the control model. The pressure head development over this relatively short model is almost linear, as shown in Figure B.6. This is because the boundary conditions are relatively close and dominate the pressure head development over the dike.

The sensitivity analysis should be repeated with different values for the foreland and hinterland lengths. Another option is to apply open boundary conditions to the model's vertical boundaries, allowing the FEM model to calculate the head along the boundaries or the amount of inflow and outflow through the boundaries. However, due to time constraints, extensive research on this topic is not possible.

Furthermore, sensitivity analysis is carried out for individual parameters, while correlation between model parameters is completely ignored. In reality, model parameters are correlated, and their effects on hydraulic head development over the model are influenced by one another. For example, variations in clay layer thickness and hydraulic conductivity have individual effects on pore pressure head development, but when observed together, they may not have the same effect quantity. Because of the way and amount of correlation between the two parameters, it is difficult to sum the magnitude of the effects of layer thickness and hydraulic conductivity on pore pressure head. The degree of correlation varies again depending on the parameters.

$$C$$
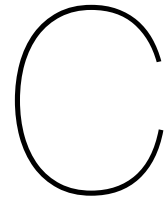
Calibration data

The goal of calibrating the cross-sectional models is to be able to fine-tune the model parameters so that the models are as close to reality as possible. This appendix contains the data used for model calibrations. Keep in mind that the Thorn field measurement data is also displayed, but the model calibration for Thorn is not performed. Thorn's standpipe and pore pressure gauges indicate that piping is not a viable failure mechanism.

Calibration of the models was carried out using data from stand pipe and pore pressure gauges at the research locations, as well as Maas water level data derived from monitoring stations along the Maas near the research locations. The standpipe data and water level data are available from 01-07-2021 to 01-08-2022, which includes the Limburg flood event from approximately 13-07-2021 to 23-07-2021.

C.1. Standpipe data

The Waterschap of Limburg has provided hydraulic head data of standpipes and pore pressure gauges present at the different research locations. The Figures C.9 to C.12 show the development of the hydraulic head in July 2021 for multiple standpipes (PB-#) and pore pressure gauges (WSP-#) at each research location. The Tables C.1 to C.4 give the characteristics and information for each standpipe and pressure gauge displayed in Figures C.9 to C.12.

Table C.1: Standpipe information Well (Waterschap Limburg, 2021)

Dike sec.	Location	Name	SFLVL [NAP]	x [RD]	y [RD]	Head SP [NAP]	sensor depth [NAP]	date	gw lvl [NAP]
60.070+60	outer toe	wsp-04	13.00	202431.11	397062.50	-	10.45	15-01-13	11.70
60.070+60	outer toe	pb-04	12.65	202431.11	397062.50	12.64	12.29	15-01-13	dry
60.070+60	crest	pb-05	15.25	202438.75	397058.77	15.22	13,92	15-01-13	dry
60.070+60	crest	wsp-05	15.25	202438.75	397058.77	-	10.63	15-01-13	11.85
60.070+60	ditch	wsp-06	12.81	202446.52	397051.62	-	10.02	15-01-13	12.13
60.070+60	hinterland	wsp-07	12.62	202459.80	397045.72	-	10.31	15-01-13	11.43

Table C.2: Standpipe information Hout-Blerick (Waterschap Limburg, 2021)

Dike sec.	Location	Name	SFLVL [NAP]	x [RD]	y [RD]	Head SP [NAP]	sensor depth [NAP]	date	gw lvl [NAP]
70.075+62	outer toe	wsp-11	14.01	207098.73	373900.37	-	12.01	15-01-13	13.34
70.075+62	outer toe	pb-10	14,01	207098.73	373900.37	14,00	13,65	15-01-13	dry
70.075+62	crest	pb-11	19,03	207086.92	373911.95	19,00	16,96	15-01-13	dry
70.075+62	crest	pb-12	19.03	207086.92	373911.95	19.01	9.07	15-01-13	13.36
70.075+62	inner toe	wsp-12	14.60	207078.54	373922.05	-	11,69	15-01-13	12.61
70.075+62	hinterland	wsp-13	14.50	207065.00	373930.00	-	11,99	15-01-13	12.85

Table C.3: Standpipe information Buggenum (Waterschap Limburg, 2021)

Dike sec.	Location	Name	SFLVL [NAP]	x [RD]	y [RD]	Head SP [NAP]	sensor depth [NAP]	date	gw lvl [NAP]
75.030+40	berm outer slope	wsp-14	16.31	196286.99	360031.44	-	14,01	15-01-13	*x
75.030+40	berm outer slope	pb-13	14.74	196290.61	360029.70	14.73	14.23	15-01-13	dry
75.030+40	crest	pb-14	20.61	196271.61	360041.97	20.58	12.98	15-01-13	15.06
75.030+40	crest	wsp-15	20.61	196271.61	360041.97	-	16.48	15-01-13	15.06
75.030+40	inner toe	wsp-16	18.15	196263.48	360047.37	-	14.40	15-01-13	15.07

*x: no controle measure possible due to rubble

Table C.4: Standpipe information Thorn (Waterschap Limburg, 2021)

Dike sec.	Location	Name	SFLVL [NAP]	x [RD]	y [RD]	Head SP [NAP]	sensor depth [NAP]	date	gw lvl [NAP]
79.037+12	hinterland	wsp-18	23.70	186948.48	351975.12	-	21,10	15-01-13	*x
79.037+12	inner toe	wsp-19	23.11	186954.00	351953.00	-	20,49	15-01-13	*x
79.037+12	crest	pb-15	24.89	186956.64	351948.33	24.96	23.73	15-01-13	dry
79.037+12	crest	wsp-20	24.90	186956.64	351948.33	-	20,55	15-01-13	*x
79.037+12	outer toe	wsp-21	22.94	186961.16	351940.43	-	20.54	15-01-13	*x

*x: no controle measure possible due to rubble

Figures C.1 to C.4 show the placement of the standpipe and pore pressure gauges on the dike at the research locations. The location of the standpipes and gauges is derived from the coordinates mentioned in the tables above and is placed on a map in Google Earth.

Figure C.1: Standpipe locations Well (Google, 2022)

Figure C.2: Standpipe locations Hout-Blerick (Google, 2022)
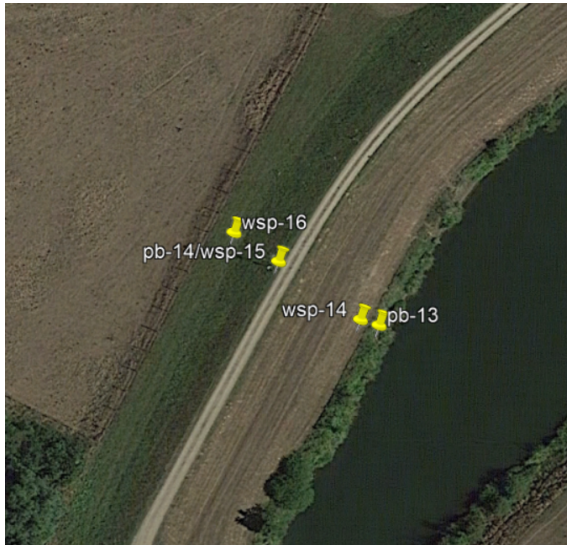
Figure C.3: Standpipe locations Buggenum (Google, 2022)
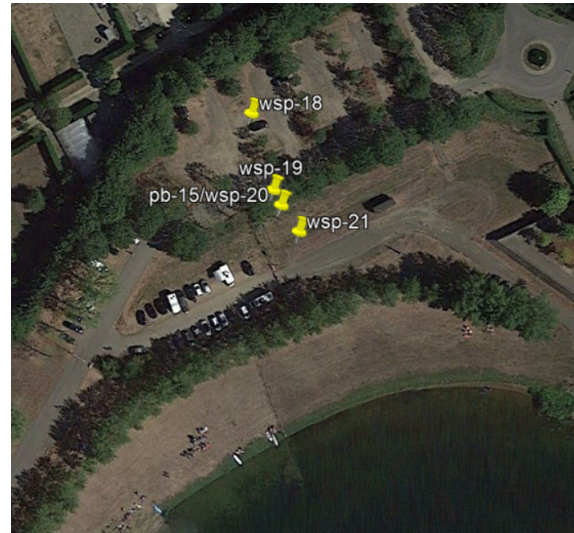
Figure C.4: Standpipe locations Thorn (Google, 2022)

Figures C.5 to C.7 demonstrate the locations and sensor depth of the standpipe and pore pressure gauges in the cross-sectional models of Well, Hout-Blerick and Buggenum. The dashed line on the domain boundaries of the cross-sectional models represents the boundary condition corresponding to the standpipe or pore pressure gauge on the boundary. The cross-sectional model of Thorn is not included in the calibration, and therefore no cross-sectional model is built for the calibration.
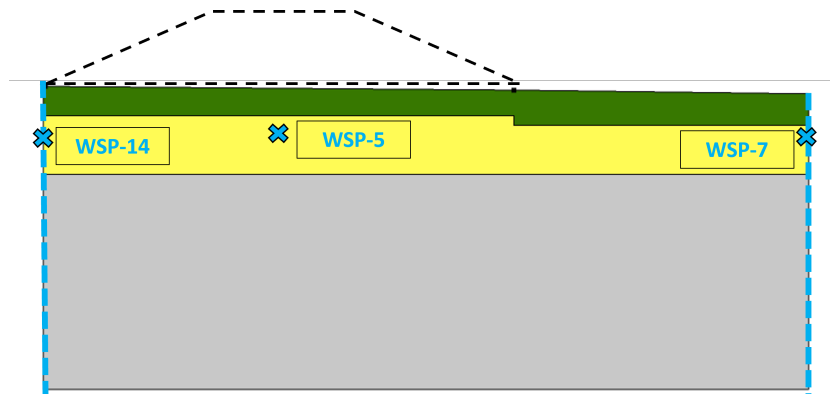
Figure C.5: Location and depth standpipes and pore pressure gauges in the model Well
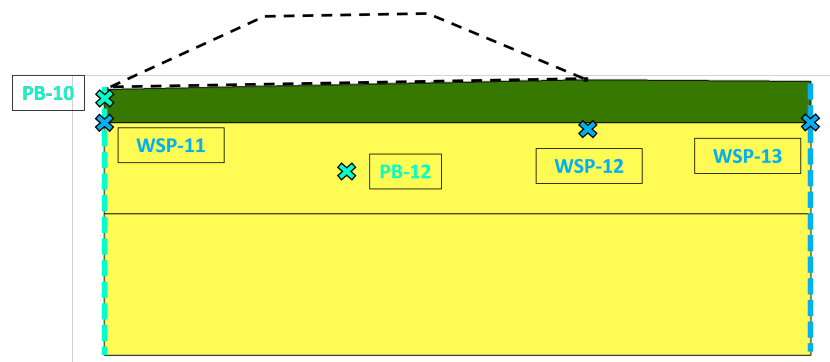
Figure C.6: Location and depth standpipes and pore pressure gauges in the model Hout-Blerick
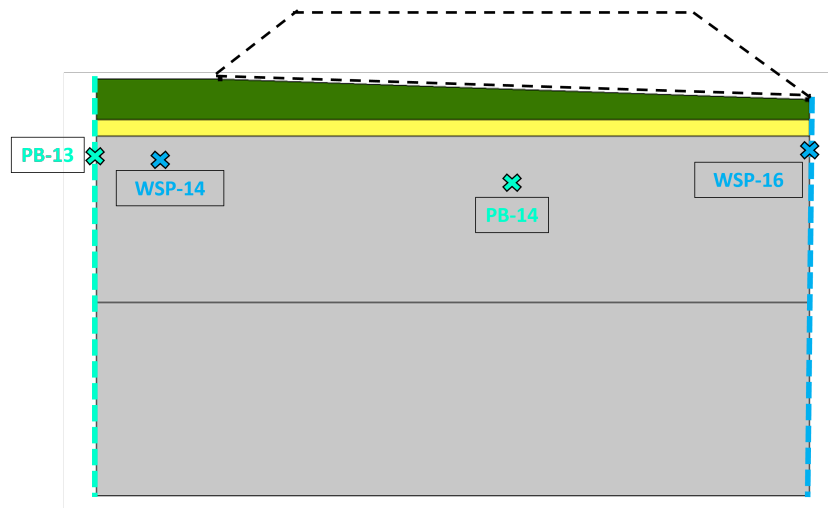
Figure C.7: Location and depth standpipes and pore pressure gauges in the model Buggenum

C.2. Maas water level data

Several monitoring stations are located along the Maas to monitor the river's water level. Because these monitoring stations are managed by Rijkswaterstaat, the collected data is freely available. A monitoring station as close to the research location as possible is used to extract water level data. When the research location is located between two stations, data from both stations is extracted and analyzed (see Table C.5). The July 2021 water level data is provided in a CSV-file containing a massive time series with a 10 minute data interval.

Table C.5: Water level monitoring along the Maas (Rijkswaterstaat, 2022)

Monitoring station	rkm	Max water level (July 2021) [cm+NAP]	Related research location (rkm)
Stevensweert	61.6	2557	Thorn (64-66)
Heel boven	67.34	2278	Thorn (64-66)
Buggenum	85	2030	Buggenum (85)
Befeld beneden	102.7	1845	Hout-Blerick (104-105)
Venlo	107	1801	Hout-Blerick (104-105)
Well Dorp	132	1548	Well (134)

Figure C.8 depicts the Maas water level development in July 2021 for the various monitoring stations mentioned in Table C.5. The high water wave in the figure differs in height, shape, and translation as seen in Figure C.8. The vertical translation in the figure is caused by the y-axis unit being in cm+NAP and the difference in surface level height between the monitoring stations and the river. The south of Limburg has a higher surface level than the north, resulting in a sloping river bed. The monitoring locations and corresponding high water waves are listed from south to north of Limburg. The horizontal translation of the high water wave is due to the fact that the wave propagates along the Maas and thus arrives at monitoring stations in the southerly region earlier than stations in the northerly region.

The depth and width of the Maas and floodplains, as well as the influences of dams and weirs, cause the difference in shape and height of the high water wave in Figure C.8. The high water wave is reduced in areas where the Maas is wider or can flood the available floodplains.
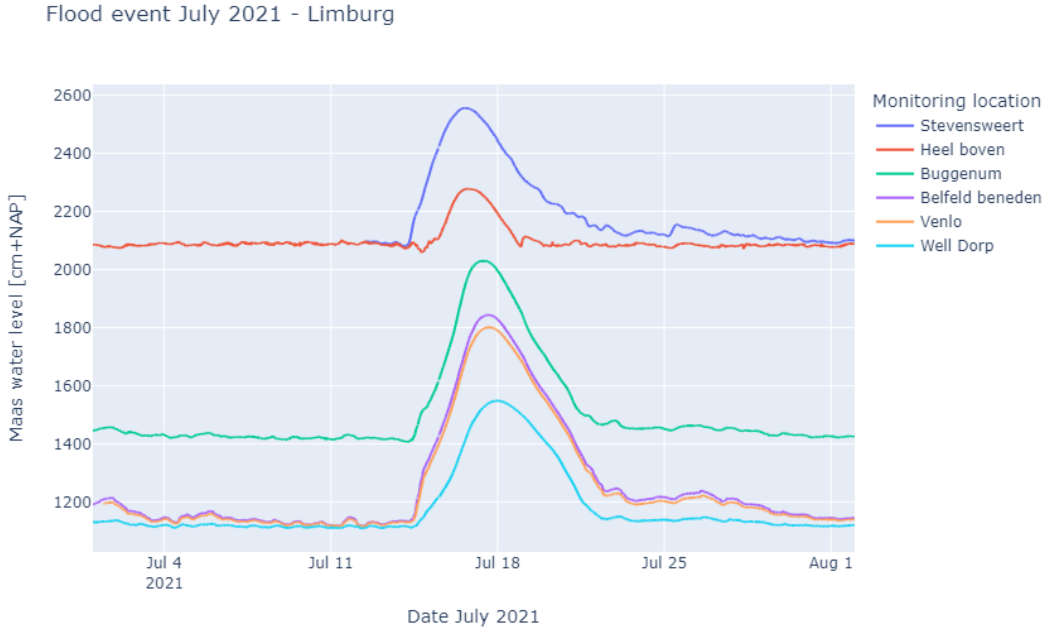
Figure C.8: Maas water levels July 2021 at the research locations (Rijkswaterstaat, 2022)
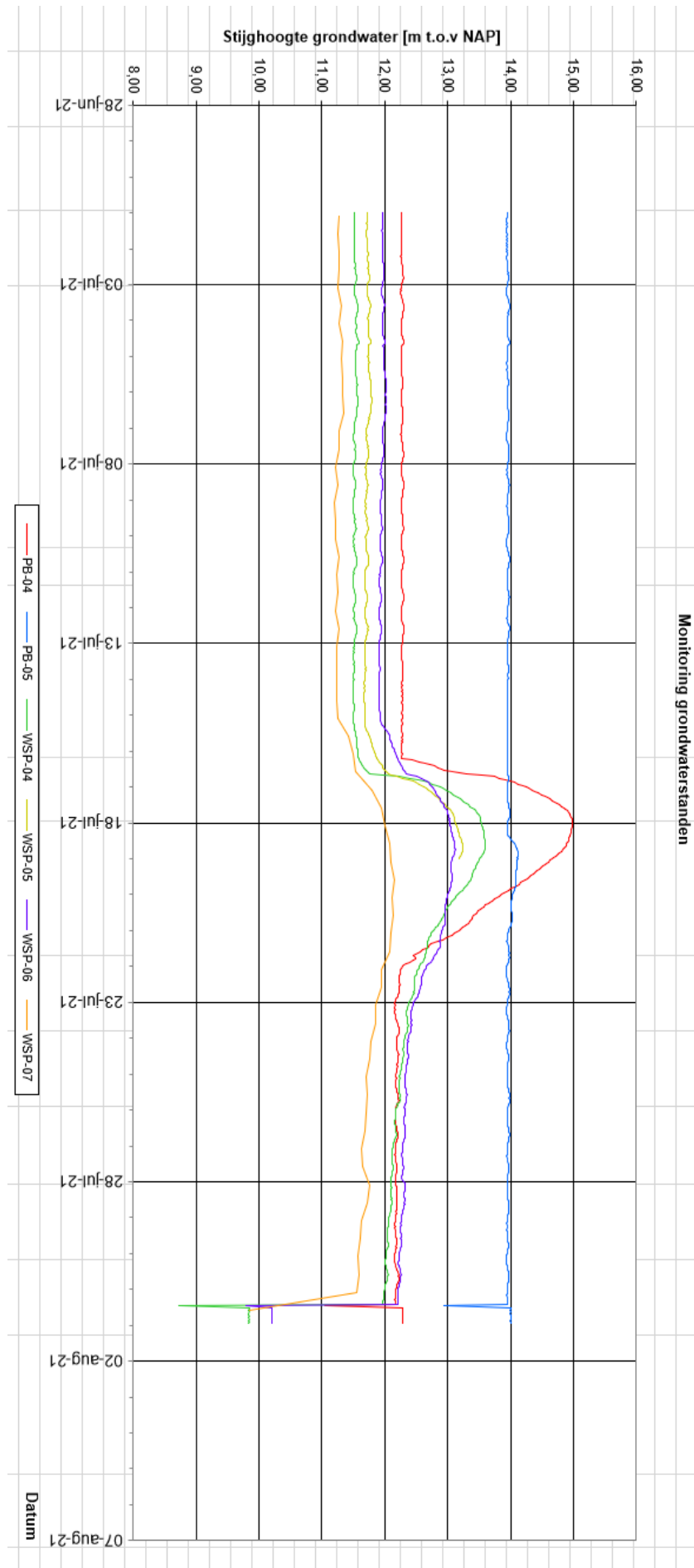
Figure C.9: Standpipe data Well (Waterschap Limburg, 2021)
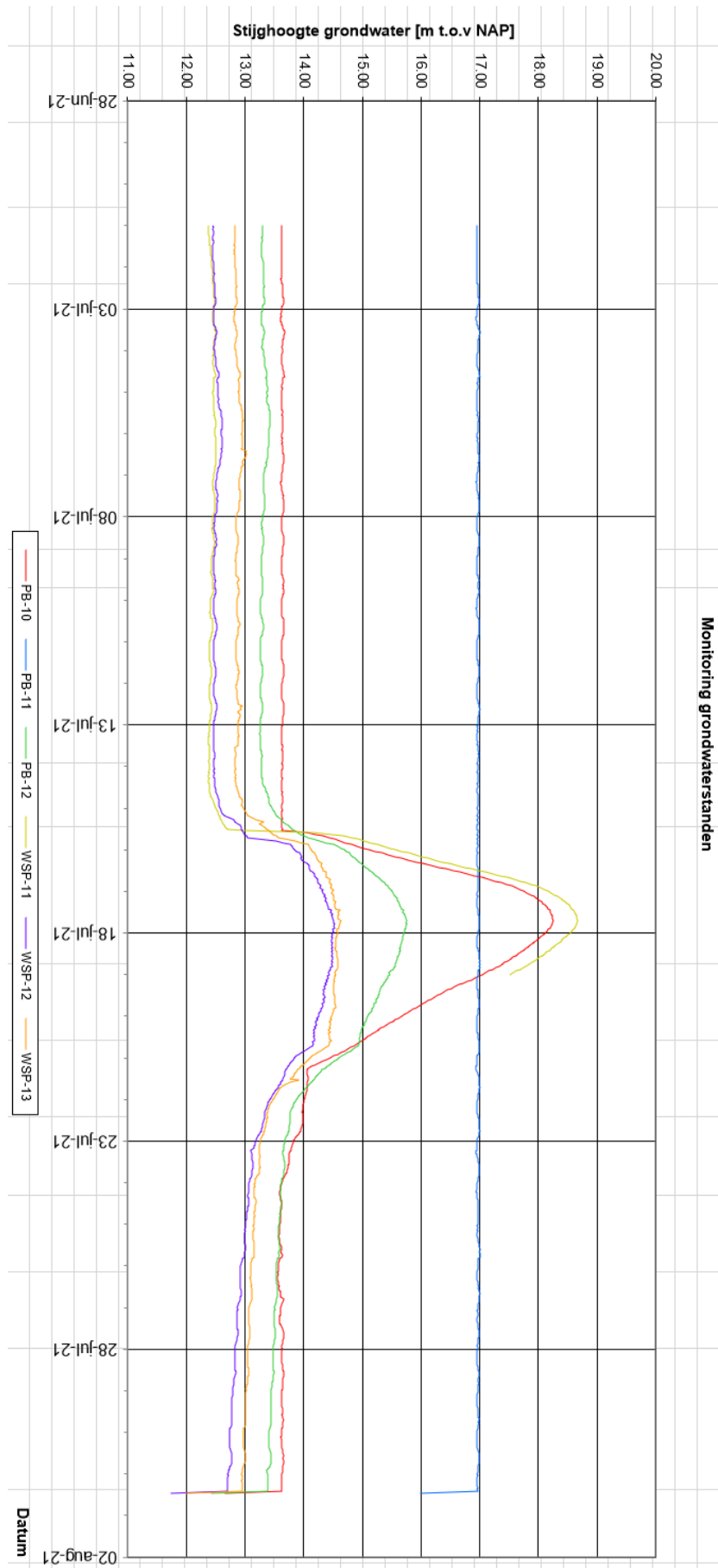
Figure C.10: Standpipe data Hout-Blerick (Waterschap Limburg, 2021)
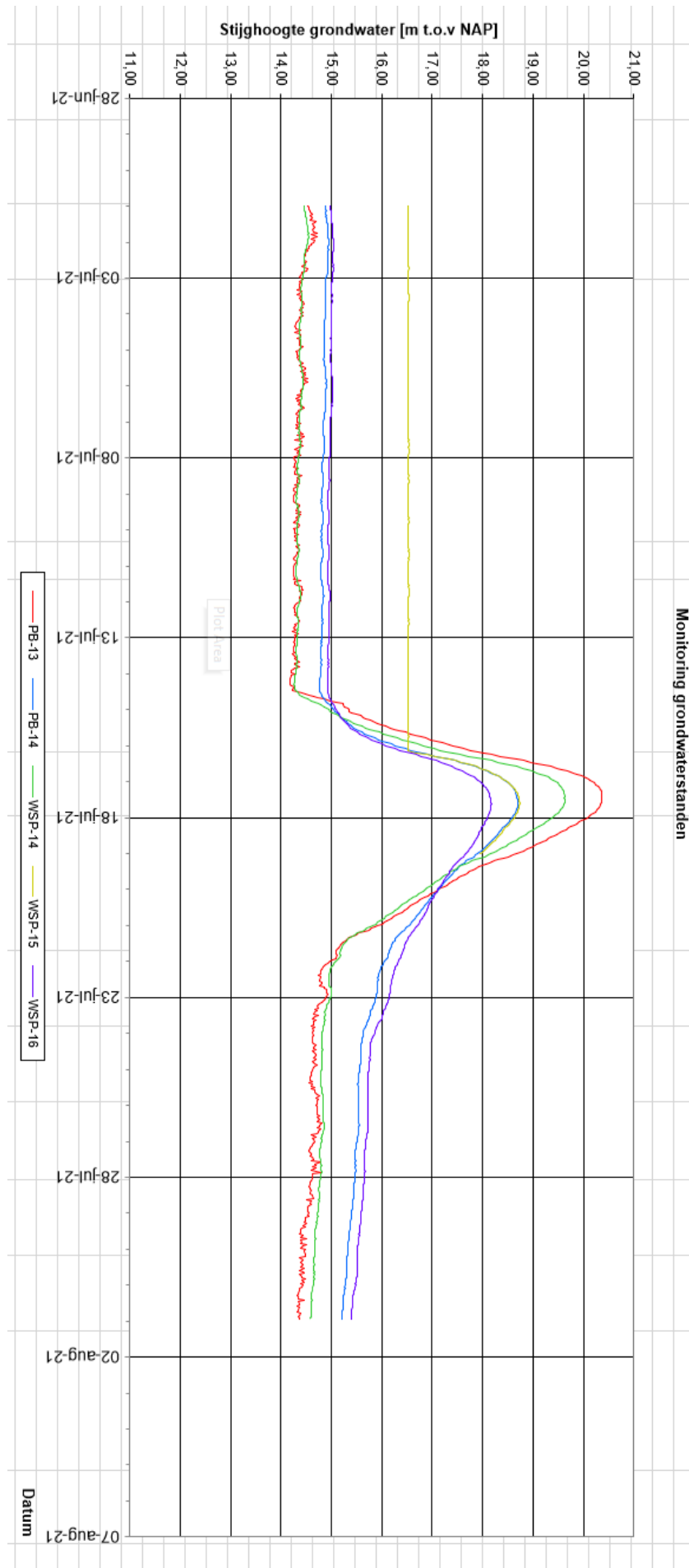
Figure C.11: Standpipe data Buggenum (Waterschap Limburg, 2021)
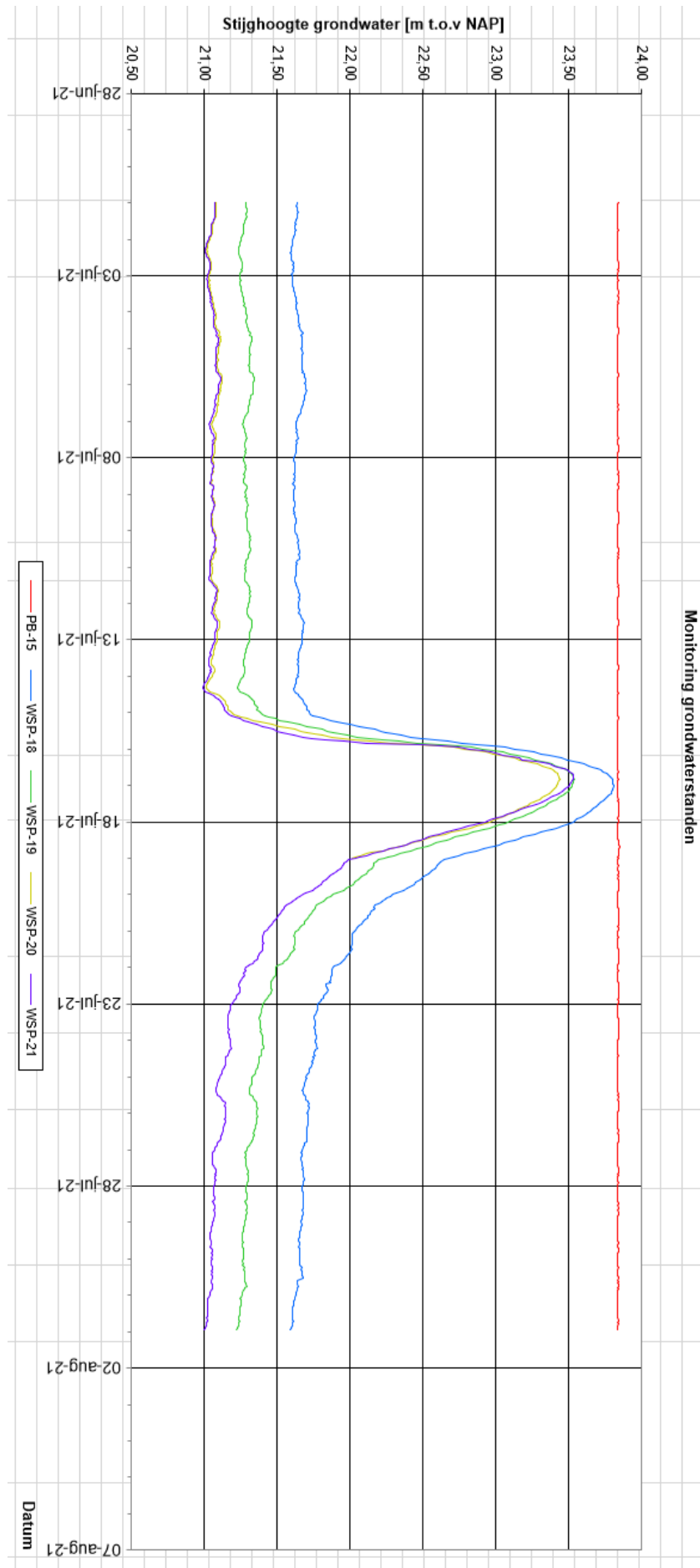
Figure C.12: Standpipe data Thorn (Waterschap Limburg, 2021)

D
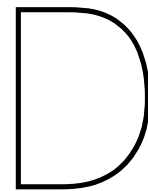
Deterministic model parameters

D.1. General parameters and calculations

This section displays the general parameters and formulas that are used as input for all cross-sectional models. The formulas are divided into Sellmeijer calculations (shown in Table D.2) and model geometry setup calculations (see Table D.1). The parameters are listed below the corresponding formula. The missing parameters in Tables D.1 and D.2 are location-specific and are included in Tables D.3 to D.6, which contain the specific model parameters of specific research location.

Table D.1: Geometry parameters and calculations

Parameter	Unit	Value/calculation
a	[m]	$n_g \cdot d_{70}$
ng	[-]	10
a_{mesh}	[m]	$d_{70,max} \cdot 30$
$d_{70,max}$	[mm]	10
C	[-]	a/a_{mesh}
k_f	[m^2]	$2(D_h^2)/\beta_f$
β_f	[-]	96
D_h	[m]	$2 \cdot a$
$D_{aquifer}$	[m]	$D_1 + D_2 + ...$
$K_{aquifer}$	[m/d]	$(D_1 K_1 + D_2 K_2)/D_{aquifer}$
$k_{aquifer}$	[m^2]	$K_{aquifer} v/g$
v	[m^2/s]	$1.33 \cdot 10^{-6}$
ρ_w	[kg/m^3]	1000
μ	[kg/ms]	$v \cdot \rho_w$
λ	[m]	$\sqrt{\dfrac{K_{aquifer} \cdot D_{aquifer} \cdot D_{clay}}{K_{clay}}}$

Table D.2: Sellmeijer calculations in COMSOL

Parameter	Unit	Value/calculation
dhdxcrit	[-]	$(\pi/3)(\gamma_{sp}/\gamma_w)(d_{70}\eta \tan(\theta)/a)$
γ_s	[kN/m^3]	26.5
γ_w	[kN/m^3]	10
γ_{sp}	[kN/m^3]	$\gamma_s - \gamma_w$
η	[-]	0.25
θ	[deg]	37
H$_{c,o}$	[m]	F$_R$*F$_S$*F$_G$*L
1.8H$_{c,o}$	[m]	$1.8 \cdot H_{c,o}$
F$_R$	[-]	$\eta(\gamma_{sp}/\gamma_w)\tan(\theta)$
F$_S$	[-]	$d_{70}/\sqrt[3]{k_{aquifer}L}$
F$_G$	[-]	$0.91(D_{aquifer}/L)^B$
B	[-]	$0.28/((D_{aquifer}/L)^{2.8} - 1) + 0.04$
H$_{c,rev}$	[m]	F$_R$F$_{S,rev}$F$_G$L
F$_{S,rev}$	[-]	$(d_{70m}/\sqrt[3]{k_{aquifer}L})(d_{70}/d_{70m})^{0.4}$
d_{70m}	[m]	$2.08 \cdot 10^{-4}$

D.2. Model parameters deterministic analysis

The model parameters for each research location are shown in Tables D.3 to D.6, and are used to perform the analytic Sellmeijer calculations and the deterministic piping assessment of Chapter 4. The parameters in the tables are mostly the same, but some cross-sectional models include additional subsoil layers. In COMSOL, these parameters are used as input parameters.

Table D.3: Model parameters Well

Parameter	Unit	Value
D_{clay}	[m]	1.5
D_{sand}	[m]	3
D_{grav}	[m]	11
K_{clay}	[m/d]	0.6
K_{sand}	[m/d]	48
K_{grav}	[m/d]	125
ϵ_{clay}	[-]	0.5
ϵ_{sand}	[-]	0.42
ϵ_{grav}	[-]	0.375
ϵ_{pipe}	[-]	1
L	[m]	24
L_f	[m]	$\lambda = 61.62$
L_h	[m]	$3\lambda = 184.87$
l	[m]	0.44*L
b	[m]	0.10
crest	[m+NAP]	15.25
SFLVL$_{fore}$	[m+NAP]	13.0
SFLVL$_{hinter}$	[m+NAP]	12.8
UC$_{hinter}$	[m+NAP]	11.0
W	[m]	H$_{c,o}$
h_b	[m]	0
d_{70}	[m]	$6.6 \cdot 10^{-4}$

Table D.4: Model parameters Hout-Blerick

Parameter	Unit	Value
D_{clay}	[m]	2
$D_{sand,1}$	[m]	5.5
$D_{sand,2}$	[m]	8.5
K_{clay}	[m/d]	0.46
$K_{sand,1}$	[m/d]	20
$K_{sand,2}$	[m/d]	75
ϵ_{clay}	[-]	0.5
ϵ_{sand}	[-]	0.42
ϵ_{pipe}	[-]	1
L	[m]	29
L_f	[m]	$\lambda = 57$
L_h	[m]	$3\lambda = 171.03$
l	[m]	0.44*L
b	[m]	0.10
crest	[m+NAP]	19
SFLVL$_{fore}$	[m+NAP]	14
SFLVL$_{hinter}$	[m+NAP]	14.50
UC	[m+NAP]	SFLVL$_{fore}$ - D$_{clay}$
W	[m]	H$_{c,o}$
h_b	[m]	0
d_{70}	[m]	$5 \cdot 10^{-4}$

Table D.5: Model parameters Buggenum

Parameter	Unit	Value
D_{clay}	[m]	1.0
D_{sand}	[m]	0.8
$D_{grav,1}$	[m]	8.2
$D_{grav,2}$	[m]	9.5
K_{clay}	[m/d]	0.29
K_{sand}	[m/d]	37
$K_{grav,1}$	[m/d]	184
$K_{grav,2}$	[m/d]	110
ϵ_{clay}	[-]	0.5
ϵ_{sand}	[-]	0.42
ϵ_{grav}	[-]	0.375
ϵ_{pipe}	[-]	1
L	[m]	29
L_f	[m]	3
L_h	[m]	$3\lambda = 283.15$
l	[m]	0.44*L
b	[m]	0.10
crest	[m+NAP]	22.10
SFLVL$_{fore}$	[m+NAP]	18
SFLVL$_{hinter}$	[m+NAP]	17
UC	[m+NAP]	16
W	[m]	H$_{c,o}$
h_b	[m]	0
d_{70}	[m]	$0.9 \cdot 10^{-4}$

Table D.6: Model parameters Thorn

Parameter	Unit	Value
D_{clay}	[m]	1.5
D_{sand}	[m]	1.8
D_{grav}	[m]	14.3
K_{clay}	[m/d]	0.49
K_{sand}	[m/d]	30
K_{grav}	[m/d]	85
ϵ_{clay}	[-]	0.5
ϵ_{sand}	[-]	0.42
ϵ_{grav}	[-]	0.375
ϵ_{pipe}	[-]	1
L	[m]	14
L_f	[m]	$\lambda = 62.34$
L_h	[m]	$3\lambda = 187.02$
l	[m]	0.44*L
b	[m]	0.10
crest	[m+NAP]	25.4
SFLVL$_{fore}$	[m+NAP]	22.94
SFLVL$_{hinter}$	[m+NAP]	23.7
UC	[m+NAP]	SFLVL$_{hinter}$ - D$_{clay}$
W	[m]	H$_{c,o}$
h_b	[m]	0
d_{70}	[m]	$4.6 \cdot 10^{-4}$

Flow regime investigation in Buggenum

The deterministic numerical piping assessment of the Buggenum research location in Section 4.2, shows that the flow regime in the pipe can become turbulent for a pipe length equal to 44% of the dike width (0.44L). The flow regime is determined by Reynolds number (R_e) and is considered laminar for $R_e < 2300$, transitional for $2300 \leq R_e \leq 3500$ and turbulent for $R_e > 3500$:

$$R_e = \frac{uD_h\rho}{mu} \tag{E.1}$$

The Reynolds number is a function of the flow velocity (u [m/s]), hydraulic diameter (D_h [m]), fluid density (ρ [kg/m^3]) and the dynamic viscosity (μ [kg/m·s]). Because all research locations have the same hydraulic diameter, density, and dynamic viscosity, these parameters cannot explain why Buggenum is the only one with a potentially turbulent flow regime in the pipe.

To investigate the cause of the high Reynolds numbers in the cross-sectional model of Buggenum, three additional analyses with varying model geometries are performed.

Original Buggenum model geometry
The original Buggenum model geometry is shown in Figure E.1 and is shown for comparison with the new analyses. The short foreland length distinguishes this geometry from the geometries of other research locations. Due to the presence of a channel along the dike, a short foreland length was chosen.

As a result, the domain boundary is relatively close to the dike, with little resistance provided by the foreland. As a result, the turbulent flow regime could be explained by the fact that the flow velocity of water entering the model through this boundary is not dampened by the resistance of the foreland.

Table E.1 demonstrates that the flow regime is laminar for a pipe length equal to 10% of the dike width. For pipes with a pipe height greater than 3 grains and a pipe length equal to 44% of the dike width, is indicated by the Reynolds numbers in Table E.2 that the flow regime inside the pipe becomes turbulent.
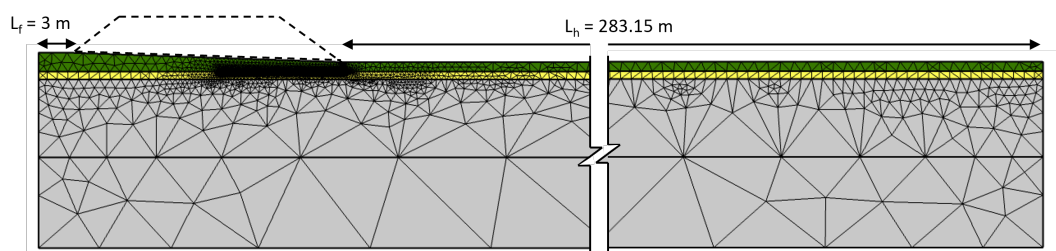
Figure E.1: Original Buggenum model geometry, pipe length = 0.44L

Table E.1: Flow regime analysis original Buggenum model (Figure E.1): 0.1L; W = 4.1 m

n_g [-]	dh/dx_{2F} [m/m]	dh/dx_{FEM} [m/m]	R_e [-]
3	0.10850	0.064132	1658.0
10	0.032551	0.0022043	1953.0
20	0.016276	2.7307E-4	1935.5
30	0.010850	8.0855E-5	1934.2
40	0.0081378	3.4111E-5	1934.2
50	0.0065102	1.7675E-5	1957.5

Table E.2: Flow regime analysis original Buggenum model (Figure E.1): 0.44L; W = 4.1 m

n_g [-]	dh/dx_{2F} [m/m]	dh/dx_{FEM} [m/m]	R_e [-]
3	0.10850	0.096520	2308.9
10	0.032551	0.0045096	3995.4
20	0.016276	5.6553E-4	4008.4
30	0.010850	1.6642E-4	3981.0
40	0.0081378	7.0280E-5	3985.1
50	0.0065102	3.6194E-5	4008.4

Buggenum model geometry with extra foreland resistance

In the first Buggenum model geometry adaptation, an extra vertical layer is included in the foreland, increasing the foreland resistance (see Figure E.2). The vertical layer represents the material at the channel's bottom that prevents water from entering the subsoil. This layer has a very low hydraulic conductivity (K = 0.0001 m/d), which is three orders of magnitude lower than the clay cover layer's hydraulic conductivity (K = 0.29 m/d). The vertical layer should slow water entering the model through this vertical boundary.

The results of this adapted model geometry show that for a pipe height greater than 3 grains, the flow regime inside the pipe remains turbulent with a pipe length equal to 44% of the dike width (see Table E.4). The Reynolds numbers in Table E.4 are slightly lower than inTable E.2, but not significantly. As a result, it can be concluded that a vertical low permeable layer has insufficient influence on flow velocity.
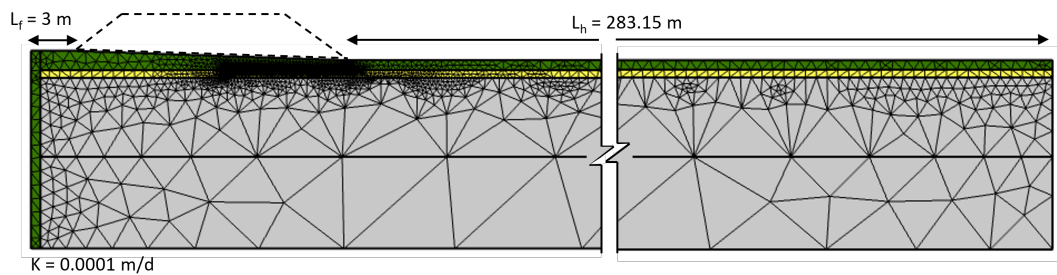
Figure E.2: Buggenum geometry with extra foreland resistance in form of clay layer, pipe length = 0.44L

Table E.3: Flow regime analysis clay Buggenum model (Figure E.2): 0.1L; W = 4.1 m

n_g [-]	dh/dx_{2F} [m/m]	dh/dx_{FEM} [m/m]	R_e [-]
3	0.10850	0.069201	1655.4
10	0.032551	0.0022007	1949.8
20	0.016276	2.7262E-4	1932.3
30	0.010850	8.0722E-5	1931.0
40	0.0081378	3.4054E-5	1931.0
50	0.0065102	1.7646E-5	1954.2

Table E.4: Flow regime analysis clay Buggenum model (Figure E.2): 0.44L; W = 4.1 m

n_g [-]	dh/dx_{2F} [m/m]	dh/dx_{FEM} [m/m]	R_e [-]
3	0.10850	0.096323	2304.2
10	0.032551	0.0044986	3985.6
20	0.016276	5.6414E-4	3998.6
30	0.010850	1.6601E-4	3971.2
40	0.0081378	7.0107E-5	3975.3
50	0.0065102	3.6105E-5	3998.6

Buggenum model geometry with extra long foreland

The foreland length of the Buggenum model geometry is implemented in this analysis similarly to other research locations (see Figure E.3). The foreland length is equal to the leakage length, being 94.38 m. This assumption ignores the presence of the channel in the foreland. This analysis must demonstrate how a long foreland length affects the Reynolds number and thus the flow regime.

The Reynolds numbers of Table E.6 show that the flow regime inside the pipe for the geometry with an extra long foreland remains laminar for both pipe lengths (0.1L and 0.44L). When these findings

are compared to the results of the original Buggenum model geometry, it is clear that a longer foreland reduces the Reynolds number.
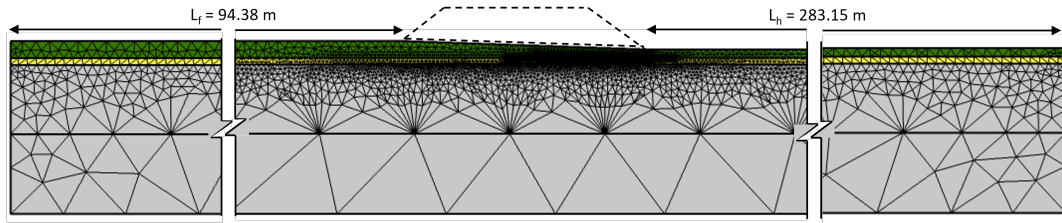
Figure E.3: Buggenum geometry with extra long foreland, pipe length = 0.44L

Table E.5: Flow regime analysis extra long Buggenum model (Figure E.3): 0.1L; W = 4.1 m

n_g [-]	dh/dx_{2F} [m/m]	dh/dx_{FEM} [m/m]	R_e [-]
3	0.10850	0.027684	662.24
10	0.032551	8.6826E-4	769.26
20	0.016276	1.0682E-4	757.10
30	0.010850	3.1197E-5	746.27
40	0.0081378	1.2874E-5	729.97
50	0.0065102	6.4568E-5	715.07

Table E.6: Flow regime analysis extra long Buggenum model (Figure E.3): 0.44L; W = 4.1 m

n_g [-]	dh/dx_{2F} [m/m]	dh/dx_{FEM} [m/m]	R_e [-]
3	0.10850	0.032310	772.90
10	0.032551	0.0013406	1187.7
20	0.016276	1.6677E-4	1182.0
30	0.010850	4.8778E-5	1166.8
40	0.0081378	2.0487E-5	1161.6
50	0.0065102	1.0549E-5	1168.2

Hout-Blerick model geometry with Buggenum's foreland and hinterland lengths

The Hout-Blerick model geometry is modified to include the foreland and hinterland lengths of the original Buggenum model geometry in order to demonstrate whether the potential turbulent flow regime is caused by the ratio of foreland and hinterland lengths. Originally, the foreland length of Hout-Blerick was 61.62 and the hinterland length was 184.87. This model configuration led to the results in Tables E.7 and E.8.

Table E.7: Flow regime analysis original Hout-Blerick geometry: 0.1L; W = 5 m

n_g [-]	dh/dx_{2F} [m/m]	dh/dx_{FEM} [m/m]	R_e [-]
3	0.10850	0.064132	263.05
10	0.032551	0.0024956	379.12
20	0.016276	3.1438E-4	382.08
30	0.010850	9.2737E-5	380.38
40	0.0081378	3.8620E-5	375.49
50	0.0065102	1.9303E-5	366.55

Table E.8: Flow regime analysis original Hout-Blerick geometry: 0.44L; W = 5 m

n_g [-]	dh/dx_{2F} [m/m]	dh/dx_{FEM} [m/m]	R_e [-]
3	0.10850	0.058292	239.10
10	0.032551	0.0038507	584.99
20	0.016276	4.9899E-4	606.44
30	0.010850	1.4844E-4	608.88
40	0.0081378	6.2453E-5	607.21
50	0.0065102	3.1774E-5	603.37

The Hout-Blerick geometry with Buggenum's foreland and hinterland lengths shows that the Reynolds number increases for the new geometry parameters (compare Tables E.8 and E.10). The new findings, however, do not show a turbulent flow regime in the pipe. The flow regime inside the pipe of the new Hout-Blerick geometry remains laminar.

As a result, can be concluded that the short foreland length and the foreland length to hinterland length ratio of the original Buggenum model geometry, are not the only parameters that cause the flow inside the pipe of the original Buggenum model geometry to be turbulent.
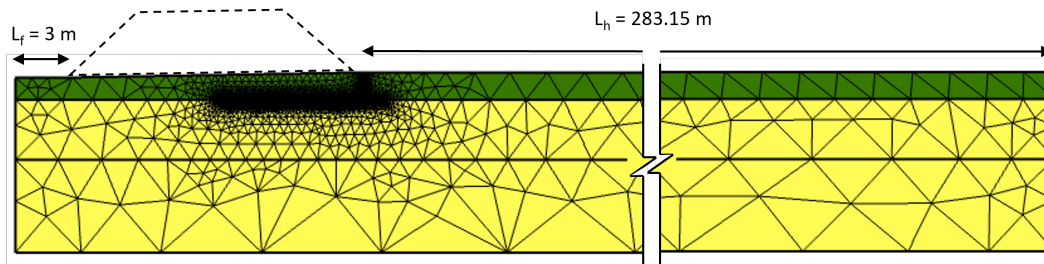
Figure E.4: Hout-Blerick geometry with foreland and hinterland length of Buggenum

Table E.9: Flow regime analysis original Hout-Blerick geometry with new foreland and hinterland length (Figure E.4): 0.1L; W = 5 m

| n_g | dh/dx_{2F} | dh/dx_{FEM} | R_e |
[-]	[m/m]	[m/m]	[-]
3	0.10850	0.087375	358.39
10	0.032551	0.0030404	461.89
20	0.016276	3.8287E-4	465.31
30	0.010850	1.1394E-5	467.35
40	0.0081378	4.8318E-5	469.78
50	0.0065102	2.4918E-5	473.18

Table E.10: Flow regime analysis original Hout-Blerick geometry with new foreland and hinterland length (Figure E.4): 0.44L; W = 5 m

| n_g | dh/dx_{2F} | dh/dx_{FEM} | R_e |
[-]	[m/m]	[m/m]	[-]
3	0.10850	0.10962	34.048
10	0.032551	0.0061251	930.51
20	0.016276	7.8532E-4	954.43
30	0.010850	2.3376E-4	958.84
40	0.0081378	9.8864E-5	961.22
50	0.0065102	5.0742E-5	963.58

Conclusion

The different analyses have shown that the turbulent flow regime inside the pipe of the original Buggenum model is not caused solely by the short foreland length. A short foreland does result in higher Reynolds numbers, but the Hout-Blerick model analysis revealed that other model parameters must also influence the Reynolds number. Because the outside hydraulic head boundary condition and aquifer depth in the Hout-Blerick analysis are similar, the two model geometries of the two research locations are comparable.

Furthermore, implementing a poorly permeable soil layer at the channel's bottom or sides results in a turbulent flow regime inside pipes with a length equal to 44% of the dike width.